CENTRO DE CIENCIAS BÁSICAS

DEPARTAMENTO DE CIENCIAS DE LA COMPUTACIÓN

TESIS

Inteligencia Artificial Aplicada al Análisis Histológico del Hipocampo

PRESENTA

Alfonso Vizcaíno Poblano

PARA OBTENER EL GRADO DE
DOCTOR EN CIENCIAS APLICADAS Y TECNOLOGÍA

TUTORES

Dr. Hermilo Sánchez Cruz

Dr. Juan Humberto Sossa Azuela

ASESORES

Dr. Julio César Ponce Gallegos

Aguascalientes, Ags. Septiembre de 2023

M. en C. Jorge Martín Alférez Chávez
DECANO (A) DEL CENTRO DE CIENCIAS BÁSICAS

_____
P R E S E N T E

Por medio del presente como ***TUTOR*** designado del estudiante **ALFONSO VIZCAÍNO POBLANO** con ID *12942* quien realizó *la tesis* titulado: **INTELIGENCIA ARTIFICIAL APLICADA AL ANÁLISIS HISTOLÓGICO DEL HIPOCAMPO**, un trabajo propio, innovador, relevante e inédito y con fundamento en el Artículo 175, Apartado II del Reglamento General de Docencia doy mi consentimiento de que la versión final del documento ha sido revisada y las correcciones se han incorporado apropiadamente, por lo que me permito emitir el **VOTO APROBATORIO**, para que *el* pueda proceder a imprimirla así como continuar con el procedimiento administrativo para la obtención del grado.

Pongo lo anterior a su digna consideración y sin otro particular por el momento, me permito enviarle un cordial saludo.

A T E N T A M E N T E
"Se Lumen Proferre"
Aguascalientes, Ags., a 14 de septiembre de *2023*.

DR. HERMILO SÁNCHEZ CRUZ
Cotutor de tesis

c.c.p.- Interesado
c.c.p.- Secretaría Técnica del Programa de Posgrado

M. en C. Jorge Martín Alférez Chávez
DECANO (A) DEL CENTRO DE CIENCIAS BÁSICAS

_____
P R E S E N T E

Por medio del presente como ***TUTOR*** designado del estudiante **ALFONSO VIZCAÍNO POBLANO** con ID *12942* quien realizó *la tesis* titulado: **INTELIGENCIA ARTIFICIAL APLICADA AL ANÁLISIS HISTOLÓGICO DEL HIPOCAMPO**, un trabajo propio, innovador, relevante e inédito y con fundamento en el Artículo 175, Apartado II del Reglamento General de Docencia doy mi consentimiento de que la versión final del documento ha sido revisada y las correcciones se han incorporado apropiadamente, por lo que me permito emitir el **VOTO APROBATORIO**, para que *el* pueda proceder a imprimirla así como continuar con el procedimiento administrativo para la obtención del grado.

Pongo lo anterior a su digna consideración y sin otro particular por el momento, me permito enviarle un cordial saludo.

A T E N T A M E N T E
"Se Lumen Proferre"
Aguascalientes, Ags., a 14 de septiembre de *2023*.

DR. JUAN HUMBERTO SOSSA AZUELA
Cotutor de tesis

c.c.p.- Interesado
c.c.p.- Secretaría Técnica del Programa de Posgrado

M. en C. Jorge Martín Alférez Chávez
DECANO (A) DEL CENTRO DE CIENCIAS BÁSICAS

_____
P R E S E N T E

Por medio del presente como ***TUTOR*** designado del estudiante **ALFONSO VIZCAÍNO POBLANO** con ID *12942* quien realizó *la tesis* titulado: **INTELIGENCIA ARTIFICIAL APLICADA AL ANÁLISIS HISTOLÓGICO DEL HIPOCAMPO**, un trabajo propio, innovador, relevante e inédito y con fundamento en el Artículo 175, Apartado II del Reglamento General de Docencia doy mi consentimiento de que la versión final del documento ha sido revisada y las correcciones se han incorporado apropiadamente, por lo que me permito emitir el **VOTO APROBATORIO**, para que *el* pueda proceder a imprimirla así como continuar con el procedimiento administrativo para la obtención del grado.

Pongo lo anterior a su digna consideración y sin otro particular por el momento, me permito enviarle un cordial saludo.

A T E N T A M E N T E
"Se Lumen Proferre"
Aguascalientes, Ags., a 14 de septiembre de *2023*.

DR. JULIO CÉSAR PONCE GALLEGOS
Asesor de tesis

c.c.p.- Interesado
c.c.p.- Secretaría Técnica del Programa de Posgrado

DICTAMEN DE LIBERACIÓN ACADÉMICA PARA INICIAR LOS TRÁMITES DEL EXAMEN DE GRADO

Fecha de dictaminación dd/mm/aaaa: 25/09/2023

NOMBRE: Alfonso Vizcaíno Poblano **ID** 12942

PROGRAMA: Doctorado en Ciencias Aplicadas y Tecnología **LGAC (del posgrado):** Inteligencia Artificial Y Modelación Estadística

TIPO DE TRABAJO: (X) Tesis ( ) Trabajo Práctico

TITULO: Inteligencia Artificial Aplicada al Análisis Histológico del Hipocampo

IMPACTO SOCIAL (señalar el impacto logrado): La tesis contribuye en la automatización del análisis de cortes histológicos de cerebros, a través de técnicas de inteligencia artificial y realidad virtual; contribuyendo así al avance en el estudio de imágenes médicas.

INDICAR SI NO N.A. (NO APLICA) SEGÚN CORRESPONDA:	
	Elementos para la revisión académica del trabajo de tesis o trabajo práctico:
SI	El trabajo es congruente con las LGAC del programa de posgrado
SI	La problemática fue abordada desde un enfoque multidisciplinario
SI	Existe coherencia, continuidad y orden lógico del tema central con cada apartado
SI	Los resultados del trabajo dan respuesta a las preguntas de investigación o a la problemática que aborda
SI	Los resultados presentados en el trabajo son de gran relevancia científica, tecnologíca o profesional según el área
SI	El trabajo demuestra más de una aportación original al conocimiento de su área
SI	Las aportaciones responden a los problemas prioritarios del país
SI	Generó transferecia del conocimiento o tecnológica
SI	Cumple con la ética para la investigación (reporte de la herramienta antiplagio)
	El egresado cumple con lo siguiente:
SI	Cumple con lo señalado por el Reglamento General de Docencia
SI	Cumple con los requisitos señalados en el plan de estudios (créditos curriculares, optativos, actividades complementarias,estancia, predoctoral, etc)
SI	Cuenta con los votos aprobatorios del comité tutoral, en caso de los posgrados profesionales si tiene solo tutorpodrá liberar solo el tutor
N.A.	Cuenta con la carta de satisfacción del Usuario
SI	Coincide con el título y objetivo registrado
SI	Tiene congruencia con cuerpos académicos
SI	Tiene el CVU del Conacyt actualizado
SI	Tiene el artículo aceptado o publicado y cumple con los requisitos institucionales (en caso que proceda)
	En caso de Tesis por artículos científicos publicados
SI	Aceptación o Publicación de los articulos según el nivel del programa
SI	El estudiante es el primer autor
SI	El autor de correspondencia es el Tutor del Núcleo Académico Básico
SI	En los artículos se ven reflejados los objetivos de la tesis, ya que son producto de este trabajo de investigación.
SI	Los artículos integran los capítulos de la tesis y se presentan en el idioma en que fueron publicados
SI	La aceptación o publicación de los artículos en revistas indexadas de alto impacto

Con base a estos criterios, se autoriza se continúen con los trámites de titulación y programación del examen de grado:

Sí x

No

FIRMAS

Elaboró:

* NOMBRE Y FIRMA DEL CONSEJERO SEGÚN LA LGAC DE ADSCRIPCION: Dr. Jaime Muñoz Arteaga

NOMBRE Y FIRMA DEL SECRETARIO TÉCNICO: Dr. Angel Eduardo Muñoz Zavala

*** En caso de conflicto de intereses, firmará un revisor miembro del NAB de la LGAC correspondiente distinto al tutor o miembro del comité tutoral, asignado por el Decano**

Revisó:

NOMBRE Y FIRMA DEL SECRETARIO DE INVESTIGACIÓN Y POSGRADO: Dr. Juan Jauregui Rincón

Autorizó:

NOMBRE Y FIRMA DEL DECANO: Mtro. Jorge Martín Alférez Chávez

Nota: procede el trámite para el Depto. de Apoyo al Posgrado

En cumplimiento con el Art. 105C del Reglamento General de Docencia que a la letra señala entre las funciones del Consejo Académico: .... Cuidar la eficiencia terminal del programa de posgrado y el Art. 105F las funciones del Secretario Técnico, llevar el seguimiento de los alumnos.

Hindawi
Computational and Mathematical Methods in Medicine
Volume 2021, Article ID 6663977, 11 pages
https://doi.org/10.1155/2021/6663977

Research Article

Pixel-Wise Classification in Hippocampus Histological Images

Alfonso Vizcaíno,[1] **Hermilo Sánchez-Cruz**,[1] **Humberto Sossa**,[2] **and J. Luis Quintanar**[3]

[1]*Departamento de Ciencias de la Computación, Universidad Autónoma de Aguascalientes, Aguascalientes 20131, Mexico*
[2]*Centro de Investigación en Computación, Instituto Politécnico Nacional, Ciudad de México, Mexico*
[3]*Departamento de Fisiología y Farmacología, Universidad Autónoma de Aguascalientes, Aguascalientes 20131, Mexico*

Correspondence should be addressed to Hermilo Sánchez-Cruz; hermilo.sanchez@edu.uaa.mx

Received 10 November 2020; Accepted 11 May 2021; Published 21 May 2021

Academic Editor: Dong Song

This paper presents a method for pixel-wise classification applied for the first time on hippocampus histological images. The goal is achieved by representing pixels in a 14-D vector, composed of grey-level information and moment invariants. Then, several popular machine learning models are used to categorize them, and multiple metrics are computed to evaluate the performance of the different models. The multilayer perceptron, random forest, support vector machine, and radial basis function networks were compared, achieving the multilayer perceptron model the highest result on accuracy metric, AUC, and F_1 score with highly satisfactory results for substituting a manual classification task, due to an expert opinion in the hippocampus histological images.

1. Introduction

The study of the hippocampus region has been of particular interest because of its relationship with memory and learning processes [1, 2], its volume as an indicator for Alzheimer's disease [3], personality disorder [4], neurological disorders derived from strokes [5–9], and drug addiction effects [10], to mention a few.

Most common hippocampal quantification techniques are based in MRI images [11, 12] for volumetric calculation and histological images [13, 14] for neural cell counting.

However, determining hippocampal volume in histological images is a challenging labour, on the one hand because image conditions are not always good and hippocampus section is of an irregular shape that is only a few pixels thick, which makes this labour an intensive and time-consuming task that demands the help of an expert to correctly identify the area of interest and so be able to determine hippocampus volume.

On one hand, pixel-wise classification has been used broadly for task such as mitosis detection in histological breast images for cancer detection [15–17], gland segmentation of prostate histology images [18], and nuclei segmentation [19], among others, where the solution range goes from digital image processing approaches used in combination with ML techniques to convolutional neural networks.

On the other hand, studies on hippocampus region have been performed exhaustively using magnetic resonance images from humans and rats, to perform segmentation tasks by applying several methods such as atlas based [20–23], a combination with support vector machines (SVMs) [24], and patch-based approaches [25], among others [26–29].

Even though each published work reports improvements over previous approaches on their own image source type and task types, as far as we know with our deep search in the literature, to perform a pixel-wise classification on hippocampus structure from rat brain histological images cuts, using the coronal anatomical plane, has not been done before. Mesejo et al. [30] perform a segmentation endeavour by using deformable models and random forest (RF) from Allen Brain Atlas [31] image repository using the sagittal anatomical plane. Senyukova et al. [32] do atlas-based segmentation on several brain sections with RF and Markov Random Fields on Nissl-stained histological sections of

Expert Systems With Applications 208 (2022) 118090

Contents lists available at ScienceDirect

Expert Systems With Applications

journal homepage: www.elsevier.com/locate/eswa

Neuron cell count with deep learning in highly dense hippocampus images

Alfonso Vizcaíno [a], Hermilo Sánchez-Cruz [a,*], Humberto Sossa [b], J. Luis Quintanar [c]

[a] Department of Computer Science, Universidad Autónoma de Aguascalientes, Aguascalientes, México
[b] Department of Computer Science, Instituto Politécnico Nacional-Centro de Investigación en Computación, Av. Juan de Dios Batiz S/N, Gustavo A. Madero, 07738 México, Distrito Federal, Mexico
[c] Department of Physiology and Pharmacology, Universidad Autónoma de Aguascalientes, Avenida Universidad 940, C.U, 20100 Aguascalientes, México

ARTICLE INFO

Keywords:
Histological images
Deep learning
Neuron cell count
Hematoxylin Eosin

ABSTRACT

Neural cell counting is one of the ways in which damage caused by neurodegenerative diseases can be assessed, but it is not an easy task when it comes to neuronal counting in the most densely populated areas of the hippocampus. In this regard, this work presents a leveraged deep learning (DL) model, an innovative way to treat histological images and their correspondent ground truth information, where highly dense cell population with fuzzy cell boundaries and low image quality exist. The proposed model achieves state-of-the-art results in the neuron cell count problem for the highly dense area of DG and CA hippocampus regions, by making use of better pixel characterization which in turn also delivers a more efficient model size and reduces training time. Furthermore, we show that the proposed image treatment can be applied to other DL models and help them to obtain a 12% performance increase. Also, we demonstrate that with the proposed methodology, an innovative and reliable way to count neural cells with poor image condition in histological analysis has been carried out.

1. Introduction

Neurodegenerative disorders are at the core of several studies characterized by neuronal loss (Mattson, 2000; Procaccini et al., 2016; Roy Sarkar & Banerjee, 2019; Zecca, Youdim, Riederer, Connor, & Crichton, 2004). Thus, accurate quantification of neurons is critically important not only in the understanding of physiological and psychological performance of some neuropathological processes, such as Alzheimer's disease (Yang, Mufson, & Herrup, 2003; Zarow, Lyness, Mortimer, & Chui, 2003) and Parkinson's disease (Giguère, Burke Nanni, & Trudeau, 2018) but in the investigation of neuroprotective drugs and the evaluation of the efficiency of treatment strategies in pre-clinical studies (Li et al., 2015; Zhu, Fotinos, et al., 2015).

Ischemic strokes, in which blood flow to the brain is blocked, are among those sources of damages that lead to these type of disorders (Radovsky, Katz, Ebmeyer, & Safar, 1997; Sugawara et al., 2000). To evaluate the harm caused by ischemic strokes it is imperative to generate reproducible brain damage, which is done with the establishment of multiple experimental models (García & Quintanar, 2020; Uluç, Miranpuri, Kujoth, Aktüre, & Başkaya, 2011) that assist the investigation of cerebral alteration and neural cell death and where immunohistochemical analysis plays an undeniable role in cell counting to measure damage of stroke and efficiency of treatments (Ke et al., 2020; Komur et al., 2014; Schuhmann, Gunreben, Kleinschnitz, & Kraft, 2016; Yata et al., 2007).

Zhu, Liu, Zou, and Torbey (2015) identified several counting strategies in the field of neuroscience research, such as unbiased stereological methods, flow cytometry, manual counting and automatic or semi-automatic counting methods.

On one hand, unbiased stereology methods tend to have higher technical requirements and the dependability of its results could be attenuated because of tissue deformation after the histological processing, staining of the sections and changes in thickness if the right approach is not considered (Dorph-Petersen, Nyengaard, & Gundersen, 2001; Zhu, Liu, et al., 2015) and thus, these methods are used less frequently than manual counting. On the other hand, counting cells within a defined region of interest (ROI) can introduce a strong bias to study results because neuronal cell death does not occur homogeneously since neurons are not equally sensitive to ischemic stress. Therefore, neuronal cell count should not be restricted to a single counting window but extended to multiple ROIs (Wang et al., 2015).

The above, coupled with the overwhelming labor of performing the

* Corresponding author.
E-mail addresses: alfonso.vizcano@gmail.com (A. Vizcaíno), hermilo.sanchez@edu.uaa.mx (H. Sánchez-Cruz), hsossa@cic.ipn.mx (H. Sossa), jlquintn@correo.uaa.mx (J.L. Quintanar).

https://doi.org/10.1016/j.eswa.2022.118090
Received 2 November 2021; Received in revised form 4 July 2022; Accepted 4 July 2022
Available online 8 July 2022

---------- Forwarded message ---------
De: **Software Impacts** <em@editorialmanager.com>
Date: dom, 25 sept 2022 a las 18:14
Subject: Send Back to Author: Request to Edit Submission
To: Hermilo Sánchez-Cruz <herssan@gmail.com>

Article Title: Cell-UNet as a DL model to quantify cells in highly dense cell population images
Corresponding Author: Dr. Hermilo Sánchez-Cruz

Dear Dr. Sánchez-Cruz,

Your submission entitled "Cell-UNet as a DL model to quantify cells in highly dense cell population images" has been received by Software Impacts. However, before we can proceed with the review process we ask you to address the following:

1- Please follow the SIMPAC template and prepare your manuscript as a single column document up to 3-4 pages. https://www.elsevier.com/journals/software-impacts/2665-9638/guide-for-authors

2- The Code Metadata table is required to be added to your manuscript as instructed in the guidelines. Please keep the format of the CodeMetadata table untouched with the specific order of the rows as in the template. If an entry does not apply to you, please put N/A and do not remove that row.

3- SIMPAC requires your open-source software/code repository in GitHub. This repo will be then forked to the SIMPAC GitHub account for archiving purposes, and readers can easily have access to the original repository in case there are updates in future. Please create a GitHub repo of your code and provide the link in row C2 of the CodeMetadata Table. Please also add an open-source license to your repository in GitHub. The instructions can be found at: https://docs.github.com/en/github/creating-cloning-and-archiving-repositories/licensing-a-repository

4- In addition, please make sure to publish your code in CodeOcean as a public capsule. Here is some info on how to do so: https://help.codeocean.com/en/articles/3063022-publishing-on-code-ocean-an-overview

Following the instructions in the link above, CodeOcean will verify your code and issue a reproducible capsule link which is public (note that this process may take up to a few days). We need that link (in row C3 of the CodeMetadata table) to complete your submission. The public CodeOcean link has the following format: https://codeocean.com/capsule/xxxxxx/tree/v1

Please log onto Elsevier Editorial System as an Author:

https://www.editorialmanager.com/simpac/.
1. Go to the menu item "Submissions/Revisions Sent Back to Author".
2. Click "Edit Submission/Revision".
3. Click on the relevant submission step on the left-hand menu.
4. Provide or modify the item/information as requested.
5. Go to "Attach Files" and "Build PDF for my Approval".
6. View and Approve your new PDF file including the changed item(s), or if needed, Edit again.

Thank you for submitting your work to the journal, and if you have any questions, please do not hesitate to contact me.
Yours sincerely,

Software Impacts

Have questions or need assistance?
For further assistance, please visit our customer service site: http://help.elsevier.com/app/answers/list/p/9435/. Here you can search for solutions on a range of topics, find answers to frequently asked questions, and learn more about Editorial Manager via interactive tutorials. You can also talk 24/5 to our customer support team by phone and 24/7 by live chat and email.

ACKNOWLEDGEMENTS

This thesis would not have been possible without the generous assistance of the whole people that walked this journey with me.

To begin, I would like to express my highest gratitude to Dr. Hermilo Sánchez Cruz, my respected advisor, for all the instructions, guidance, and support he provided to me throughout my doctoral studies. My most profound appreciation goes to Dr. José Luis Quintanar Stephano, his vast wisdom and wealth of experience has inspired me in this fantastic project and the next ones to come. The completion of this Ph.D. would not have been possible without the accurate technical assistance of my advisor Dr. Juan Humberto Sossa Azuela.

In addition, I want to express my appreciation to Autonomous University of Aguascalientes for providing me with the resources to pursue post-graduate study. Friends, colleagues, and lab mates of the pharmacology department are all well appreciated. Also, I would like to thank CONAHCYT for the studentship provided.

I would like to thank God, my parents, my so lovely and beautiful wife, and my joyful and beautiful children. It would have been impossible to finish my studies without their unwavering support over the past few years.

DEDICATION

This work is dedicated to my children. Life is beautiful, pursue your dreams, never give up, always be humble and enjoy the ride called life.

To my lovely wife. My beautiful and ever evolving dream that comes true every day and whose eyes enlighten my path.

Thank you!

INDEX

FIGURE INDEX.

RESUMEN.

Esta tesis se centra en la propuesta de diferentes algoritmos y técnicas de la inteligencia artificial empleados para el análisis de imágenes histológicas que son usadas en el estudio de la isquemia cerebral y específicamente su impacto en el hipocampo. Así mismo, lleva a cabo la consolidación de dichas propuestas a través de la implementación de aplicaciones que faciliten la evaluación de los efectos de la isquemia y de los medicamentos que contrarrestan sus efectos. También presenta como a través de un conjunto de imágenes histológicas del cerebro se puede obtener una representación 3D de éste y propone una alternativa interactiva en su estudio.

Específicamente, en el Capítulo III se expone un método innovador para el procesamiento de dichas imágenes que en conjunción con diferentes algoritmos de aprendizaje máquina obtienen un modelo que logra la identificación del hipocampo. El Capítulo IV muestra como dicho modelo es aprovechado en una aplicación que eficientiza la medición del hipocampo. Por su parte, en el Capítulo V se exhibe un nuevo modelo de red neuronal convolucional, el cual al mejorarse su arquitectura le permite identificar con mayor precisión las neuronas presentes en las regiones densamente pobladas del hipocampo. Gracias a la implementación del nuevo modelo de red neuronal, en el Capítulo VI, este modelo es usado para construir una aplicación que puede automatizar el conteo de neuronas de una manera más confiable, eficiente y eficaz. Por último, en el Capítulo VII se muestra el proceso para obtener la representación 3D de un cerebro y como tanto la representación del cerebro como las imágenes utilizadas para construirlo son vinculadas en una aplicación de realidad virtual que podría dinamizar el estudio de las estructuras cerebrales.

ABSTRACT.

This thesis focuses on the proposal of different artificial intelligence algorithms and techniques used for the analysis of histological images that are used in the study of cerebral ischemia and specifically its impact on the hippocampus. Likewise, it carries out the consolidation of these proposals through the implementation of applications that facilitate the evaluation of the effects of ischemia and the drugs that counteract its effects. It also presents how a 3D representation of the brain can be obtained through a set of histological images of the brain and proposes an interactive alternative in its study.

Specifically, in Chapter III an innovative method for the processing of these images is shown, which in conjunction with different machine learning algorithms obtains a model that achieves the identification of the hippocampus. Chapter IV exhibits how this model is used in an application that makes the measurement of the hippocampus more efficient. On the other hand, in Chapter V a new model of convolutional neural network is presented, which by improving its architecture allows it to identify with greater precision the neurons present in the densely populated regions of the hippocampus. Thanks to the implementation of the new neural network model, in Chapter VI, this model is used to build an application that can automate the counting of neurons in a more reliable, efficient, and effective way. Finally, Chapter VII shows the process to obtain a 3D representation of a brain and how both the representation of the brain and the images used to build it are linked in a virtual reality application that could boost the study of brain structures.

CHAPTER I - INTRODUCTION.

The analysis of histological images that are used in the study of cerebral ischemia and its impact on the hippocampus is a challenging task because on one side, they contain intricate anatomical sections that demand the help of a subject matter experts to correctly identify the area of interest, making this a labor intensive, time consuming and, since image conditions are not always good, an error prone task too.

There are several sub areas in artificial intelligence, such as machine learning and computer vison, where the computer is “taught” to “see” objects that permit the computer to detect, locate, delimit, or classify object, and in some cases, it can even generate new objects. That means, computer vision can be capable of “seeing” the patterns that subject matter experts have learned to identify during years of experience.

This is why, in conjunction with the pharmacology department of Autonomous University of Aguascalientes, it is presented throughout this work, a set of artificial intelligence algorithms and techniques that automates the analysis of histological images to compute key performance indicators such as hippocampus area measurement and neuron counting, which in turn, aide scientist to evaluate the effectiveness of drugs in ischemic strokes treatments. Not only that, here it is also shown a computer vision approach that proposes an alternative method to study the brain and its histological tissues using virtual reality technology.

Because of the nature of the different problems being solved, the distinct image sets with their respective characteristics and challenges, and the number of images made available, it was decided to solve such problems through different strategies. For instance, the images used to measure hippocampal area are digitized from an optical microscope with a smaller magnifying glass, than the ones used for cell counting where a much bigger magnifying glass needs to be used. Furthermore, these images come from histological cuts obtained from rats using a different stain, that the images used to do the virtual reality study proposal. With all of this, the methodology utilized to effectively manage each set of images needs to be different. The following chapters describe in detail the methodology used for each one of these problems, but the main strategy is briefly discussed here.

Chapter III reveals a pixel characterization technique that in conjunction with a machine learning algorithm, can obtain a hippocampus pixel classifier and with this effectively obtain the hippocampus from a histological image. Also, in this section it is presented how the different machine learning models are trained and how the best classifier is determined by evaluating each of the machine learning algorithms used here against a set of different metrics.

The best machine learning model found in the previous chapter, along with the pixel characterization technique, are used in Chapter IV where it is explained the consideration taken for building an application that performs hippocampus area measurement, and here it is also shown how the users can use the application.

Chapter V makes use of a different algorithm available in artificial intelligence known as convolutional neural network that specializes in extracting and learning patterns from images to correctly classify and locate objects in them. Here, an enhanced architecture of a convolutional neural network is used to teach the deep learning model to learn to identify cells on highly dense and noisy images. In this section it is also shown how the proposed deep learning model is trained, how it is evaluated against other different models and the metrics that are used to evaluate them.

Then, chapter VI is concerned on presenting the consideration taken to build an application that automates cell counting using the convolutional neural network proposed previously. This chapter also explains the steps that the user needs to execute to obtain cell count automatically.

Finally, chapter VII exposes the details on how a 3D image reconstruction of a mouse brain is achieved by using a process that involves traditional computer vision techniques to obtain the representing points of the contour of the brain, how this information is treated to build a 3D model and, how this 3D model is used in a virtual reality application that interacts with the user to analyze the reconstructed information.

1.1 Research objective.

To facilitate histological analysis process with the use of modern and accurate techniques.

1.2 Specific objectives.

1. To define a prediction model that automatically identifies hippocampus with an accuracy greater than 90% in histological images.
2. To create a system that is capable of measuring the occupied area by the hippocampus with an accuracy greater than 90%.
3. To define a prediction model that is capable of identifying neuron cells with an accuracy greater than 90% so that the identified cells can be automatically counted.
4. To create a system that is capable of performing 3D reconstruction of hippocampus brain structure from a series of histological images.
5. To present the reconstructed 3D model in a VR headset.

CHAPTER II - DERIVED WORK FROM THE THESIS.

Vizcaíno, A., Sánchez-Cruz, H., Sossa, H., & Quintanar, J. L. (2021). Pixel-wise classification in hippocampus histological images. Computational and Mathematical Methods in Medicine, 2021, 1-11.

Vizcaíno, A., Sánchez-Cruz, H. (2021). HMoHI [Mobile Application Software]. México, INDAUTOR: 03-2021-012711394300-01.

Vizcaíno, A., Sánchez-Cruz, H., Sossa, H., & Quintanar, J. L. (2022). Neuron cell count with deep learning in highly dense hippocampus images. Expert Systems with Applications, 208, 118090.

CHAPTER III - ML MODEL TO IDENTIFY HIPPOCAMPUS.

3.1 Introduction.

This section describes the research performed to determine what techniques and machine learning models best accomplish the objective of hippocampus identification. It explains how images were acquired, how images were processed and how machine models were trained and evaluated. Finally, it shows the conclusion about this research.

3.2 Article.

Hindawi
Computational and Mathematical Methods in Medicine
Volume 2021, Article ID 6663977, 11 pages
https://doi.org/10.1155/2021/6663977

Research Article

Pixel-Wise Classification in Hippocampus Histological Images

Alfonso Vizcaíno,[1] **Hermilo Sánchez-Cruz**,[1] **Humberto Sossa**,[2] **and J. Luis Quintanar**[3]

[1]*Departamento de Ciencias de la Computación, Universidad Autónoma de Aguascalientes, Aguascalientes 20131, Mexico*
[2]*Centro de Investigación en Computación, Instituto Politécnico Nacional, Ciudad de México, Mexico*
[3]*Departamento de Fisiología y Farmacología, Universidad Autónoma de Aguascalientes, Aguascalientes 20131, Mexico*

Correspondence should be addressed to Hermilo Sánchez-Cruz; hermilo.sanchez@edu.uaa.mx

Received 10 November 2020; Accepted 11 May 2021; Published 21 May 2021

Academic Editor: Dong Song

This paper presents a method for pixel-wise classification applied for the first time on hippocampus histological images. The goal is achieved by representing pixels in a 14-D vector, composed of grey-level information and moment invariants. Then, several popular machine learning models are used to categorize them, and multiple metrics are computed to evaluate the performance of the different models. The multilayer perceptron, random forest, support vector machine, and radial basis function networks were compared, achieving the multilayer perceptron model the highest result on accuracy metric, AUC, and F_1 score with highly satisfactory results for substituting a manual classification task, due to an expert opinion in the hippocampus histological images.

1. Introduction

The study of the hippocampus region has been of particular interest because of its relationship with memory and learning processes [1, 2], its volume as an indicator for Alzheimer's disease [3], personality disorder [4], neurological disorders derived from strokes [5–9], and drug addiction effects [10], to mention a few.

Most common hippocampal quantification techniques are based in MRI images [11, 12] for volumetric calculation and histological images [13, 14] for neural cell counting.

However, determining hippocampal volume in histological images is a challenging labour, on the one hand because image conditions are not always good and hippocampus section is of an irregular shape that is only a few pixels thick, which makes this labour an intensive and time-consuming task that demands the help of an expert to correctly identify the area of interest and so be able to determine hippocampus volume.

On one hand, pixel-wise classification has been used broadly for task such as mitosis detection in histological breast images for cancer detection [15–17], gland segmentation of prostate histology images [18], and nuclei segmentation [19], among others, where the solution range goes from digital image processing approaches used in combination with ML techniques to convolutional neural networks.

On the other hand, studies on hippocampus region have been performed exhaustively using magnetic resonance images from humans and rats, to perform segmentation tasks by applying several methods such as atlas based [20–23], a combination with support vector machines (SVMs) [24], and patch-based approaches [25], among others [26–29].

Even though each published work reports improvements over previous approaches on their own image source type and task types, as far as we know with our deep search in the literature, to perform a pixel-wise classification on hippocampus structure from rat brain histological images cuts, using the coronal anatomical plane, has not been done before. Mesejo et al. [30] perform a segmentation endeavour by using deformable models and random forest (RF) from Allen Brain Atlas [31] image repository using the sagittal anatomical plane. Senyukova et al. [32] do atlas-based segmentation on several brain sections with RF and Markov Random Fields on Nissl-stained histological sections of

mouse brains. And Riklin-Raviv et al. [33] propose a slice-by-slice segmentation with three-dimensional Gaussian mixtures and level sets where the successful segmentation of one section provides a prior for the subsequent one, assuming that the segmentation of few sparsely sampled slices is done manually.

This work reports the implementation of a computer vision method to extract pixel features and use them along with several machine learning (ML) techniques such as multilayer perceptron network (MLP), SVM, radial basis function network (RBFN), and RF, to perform pixel-wise classification on rat brain histological images using the coronal anatomical plane to correctly identify the hippocampus structure and facilitate its measurement.

2. Materials and Methods

The images used in this work are supplied by the Pharmacology Department of the Autonomous University of Aguascalientes. These images are serial coronal sections of approximately 6 μ thick, from male rat brains of the Sprague Dawley strain around 8-12 weeks old with a weight of 250-330 g. The cuts are stained with a specific chemical dye, and in this case hematoxylin-eosin is employed, to create contrast on the seeked anatomical structure.

A total of 25 images were digitized from an optical microscope with a magnifying glass of 0.67x, using an LGE LM-X520 camera model that was configured with an ISO speed rating of 100, a focal length of 3.5 mm, and a variable exposure time ranging from 1/60 s to 1/30 s. Each image was captured at 4161 × 3120 pixels and was saved originally in JPEG format.

When performing a visual inspection on these images, several conditions can be identified:

(i) No relevance on a specific colour for detecting anatomical structures

(ii) Different lighting effects: some images are brighter than others

(iii) Fuzziness of the hippocampus boundaries

(iv) Variability of hippocampus' shape and orientation

(v) Cutoff of regions and presence of markings such as scraps, tears, and streaks in tissue

(vi) Rotated and uncentred brain position

Examples of some of these characteristics are shown in Figure 1.

Our methodology for hippocampus pixel classification consists of four consecutive steps, as depicted in Figure 2. The first step uses image processing to enhance hippocampus region. The second step characterizes each pixel as a 14-dimensional vector. Those vectors constitute the features used by the classification algorithms. After all images have been characterized, the third step begins. At this step, the training, validation, and test set are created. The last step involves feature classification to differentiate between a non-hippocampus pixel and hippocampus pixel. The details of each of these steps are now described.

2.1. Image Conditioning and Preprocessing. The provided images contain ample dark areas, since brain image is swiveled and given the large image dimensions, it is necessary to condition them in order to speed up its preprocessing step. Therefore, images are straightened and only brain image is kept along with its aspect ratio. It is determined that an image size average of 1024 × 832 pixels is big enough to preserve hippocampus pixels and small enough to perform a fast preprocessing step. An example of the conditioning phase is displayed in Figure 3. Finally, the coordinates that make up the main hippocampus bounding box are annotated.

Because of the ample differences between hippocampus images and the image conditions explained in previous section, a preprocessing phase is performed in order to enhance hippocampus region and extract meaningful information to construct the features that will be used later in the classification step. This phase is based in the procedure employed in Vega et al. [34] and Marin et al. [35]. However, given the difference between the images and their respective domain field, the procedure has to be tailored to generate suitable images. Next, the details of the preprocessing step are described.

2.1.1. Colour Independence. Histological cuts contain different colours because of the type, amount of dye, and the exposure time given to the tissue. Consequently, pixels differ in colour and intensity despite belonging to the same hippocampus region. For this reason, the input image is converted from an original RGB colour space to a Hue Saturation Value (HSV) colour space, extracting the Value Channel (VC) to better capture the full range of the different colours that belong to the hippocampus and to make it independent from the illumination of the sample images. Then, the image is cropped to the annotated bounding box to be furthered processed. I_V denotes the resultant image for future references. Because of the nature of VC, the hippocampus region is represented by dark colour pixels which correspond to values close to zero. In order to emboss them, image is negated having I_{NV} as result.

$$I_{\mathrm{NV}} = 255 - I_V. \tag{1}$$

Figures 4(a) and 4(d) show an example of this phase.

2.1.2. Background Homogenization. Since the background is not homogeneous, a mean filter followed by a convolution with a Gaussian kernel followed by a histogram correction operation is applied. This phase is performed in the same way that [34] does background homogenization but working with an I_{NV} image. The resulting image of this phase is denoted as I_H, and an example of the outcome is presented in Figures 4(b) and 4(e).

2.1.3. Hippocampus Enhancement. Hippocampus enhancement is performed by applying a top-hat transformation.

$$I_{\mathrm{HE}} = \gamma(I_H), \tag{2}$$

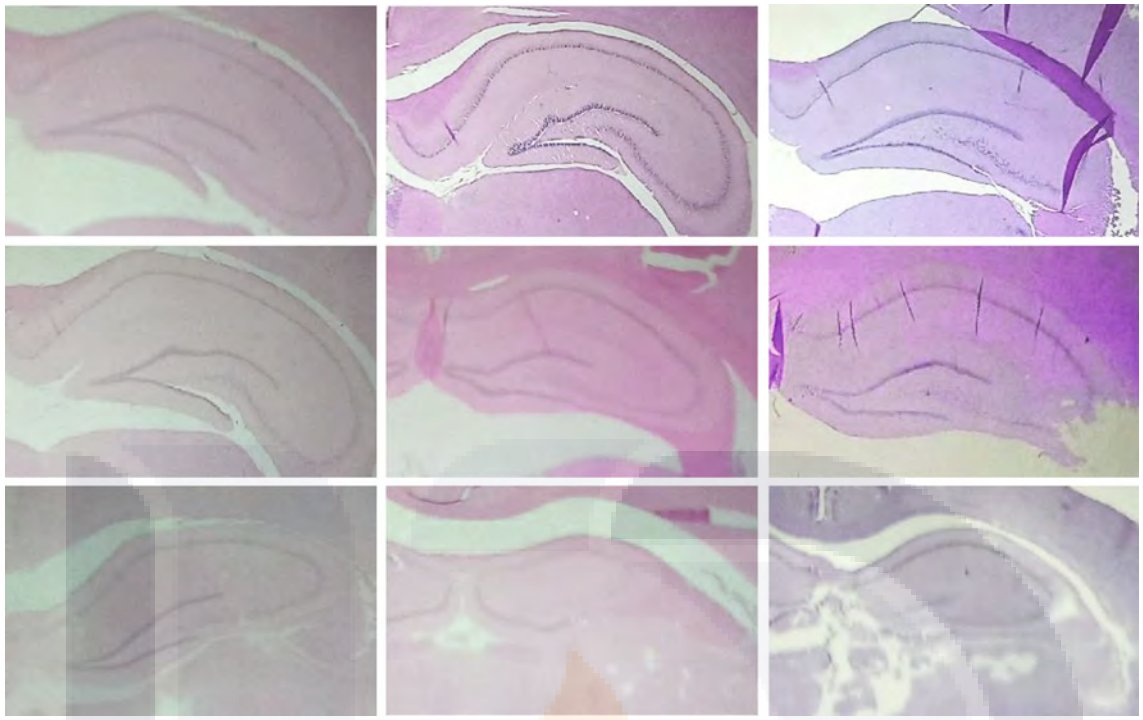

Figure 1: Coronal sections of the rat brain where the layers of the hippocampus stained with hematoxylin and eosin are observed. 3x magnification. Columns show difference in colour as well as in lighting. Rows show variability in hippocampus shape and markings presence.

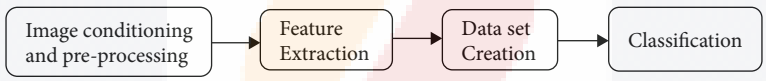

Figure 2: Diagram of the implemented methodology for hippocampus pixel-wise classification.

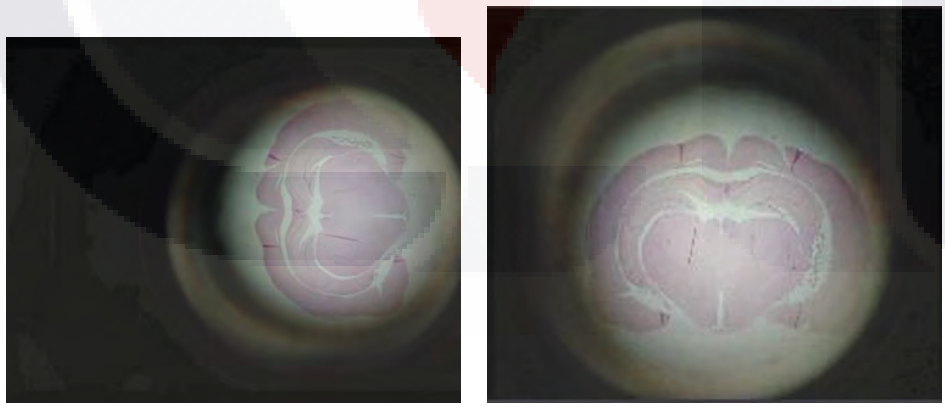

(a) (b)

Figure 3: (a) Original image. (b) Final image: rotated, centred, and resized.

where γ is a morphological opening using a disc of eight pixels in radius, thus removing most anatomical structures not belonging to hippocampal region and yielding better results than performing a boundary detection with algorithms like Canny, Prewitt, and Sobel. Figures 4(c) and 4(f) exhibit an example of the procedure applied in this phase.

2.2. Feature Extraction. The purpose of this step is to perform a pixel characterization in terms of some quantifiable measurements that can be used latter in the classification step. To accomplish this task, unlike Marin et al. and Vega et al. whom used seven and five functions, respectively, in this work, a total of fourteen functions are used. Our method uses

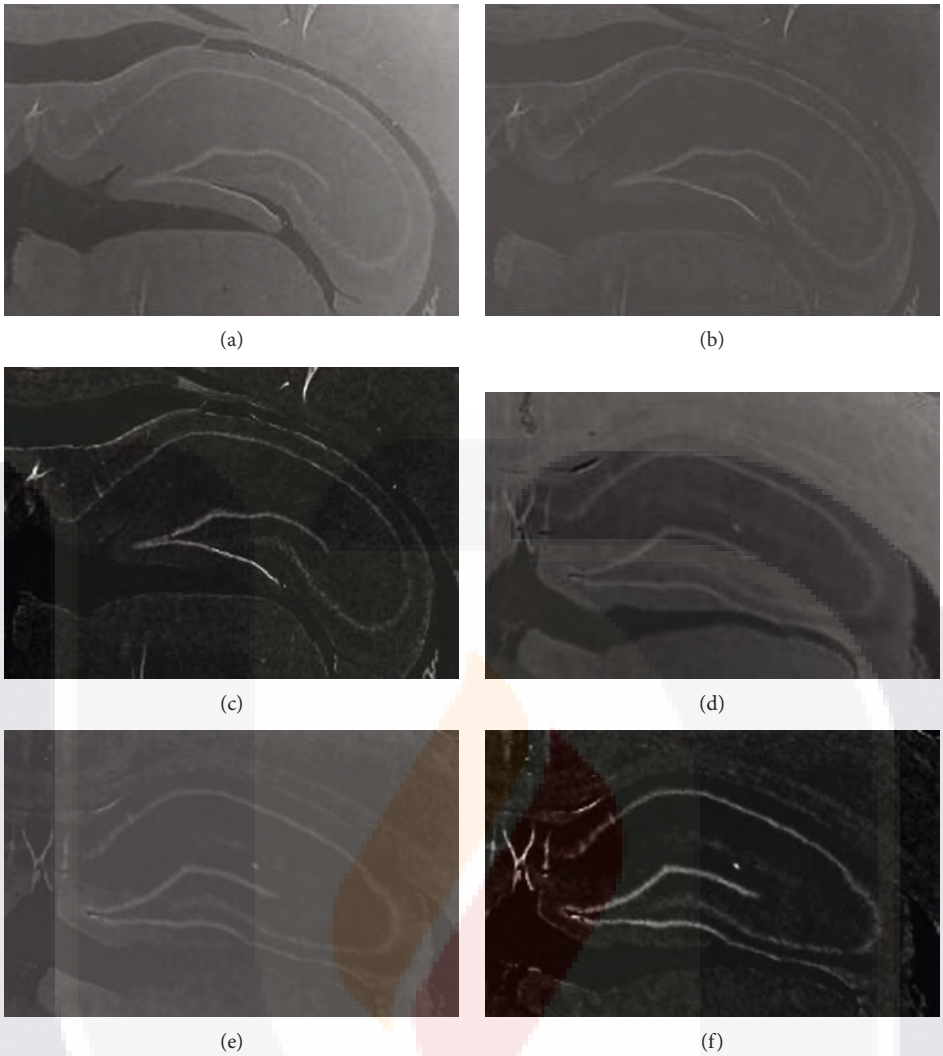

Figure 4: (a, d) Colour independence. (b, e) Background homogenization. (c, f) Hippocampus enhancement.

some variants that are described. The first five features are as follows: $f_1, f_2, \cdots, f_5$, which are based on the pixel's grey-level information available. In this work, we find that the features calculated from I_{HE} produce more meaningful representation of hippocampus pixels. The features are outlined as follows: considering a squared pixel region of size $w \times w$ taken from I_{HE} and centred at pixel (x, y), we have the following:

f_1 is the value of the pixel being characterized at position (x, y) subtracted from the smallest value of the squared region

$$f_1(x, y) = I_{\mathrm{HE}}(x, y) - \min_{(s,t) \in S^9_{x,y}} \{I_{\mathrm{HE}}(s, t)\}. \quad (3)$$

f_2 is the largest value of the squared region subtracted from the value of the pixel being characterized at position (x, y)

$$f_2(x, y) = \max_{(s,t) \in S^9_{x,y}} \{I_{\mathrm{HE}}(s, t)\} - I_{\mathrm{HE}}(x, y). \quad (4)$$

f_3 is the value of the pixel being characterized at position (x, y) subtracted from the average value of the squared region

$$f_3(x, y) = I_{\mathrm{HE}}(x, y) - \operatorname*{mean}_{(s,t) \in S^9_{x,y}} \{I_{\mathrm{HE}}(s, t)\}. \quad (5)$$

f_4 is the value of standard deviation of the squared pixel region characterized at position (x, y)

$$f_4(x, y) = \operatorname*{stdDev}_{(s,t) \in S^9_{x,y}} \{\mathrm{I}_{\mathrm{HE}}(s, t)\}. \quad (6)$$

f_5 is the value of the pixel being characterized at position (x, y)

$$f_5(x, y) = I_{\mathrm{HE}}(x, y). \quad (7)$$

Then, for the next two features, f_6 and f_7, we use the

first two Hu moment invariants [36] denoted by ϕ_1 and ϕ_2. These are computed from I_{Hu} image, which is obtained by multiplying a squared pixel region of 17×17 size from I_{HE} and an equal dimension matrix of Gaussian values, whose mean is 0 and variance is $(1.7)^2$; then, I_{Hu} is given by

$$I_{\text{Hu}}(i,j) = I_{\text{HE}}^{S_{x,y}^{17}}(i,j) \times G_{0,1.7^2}^{17}(i,j). \tag{8}$$

With these choices of parameters, the 9×9 central values in Gaussian matrix contain 97% of the area of the represented Gaussian distribution, making the remainder values being close to 0. The effect of this multiplication is that the values become sensitive for describing hippocampal and nonhippocampal central pixels. Given that ϕ_1 and ϕ_2 computation can take nonpositive and zero values, f_6 is defined as

$$f_6 = \begin{cases} \log(\phi_1), & \text{if} \phi_1 > 0, \\ -\log(|\phi_1|), & \text{if} \phi_1 < 0, \\ 0, & \text{otherwise}, \end{cases} \tag{9}$$

and f_7 is defined as

$$f_7 = \begin{cases} \log(\phi_2), & \text{if} \phi_2 > 0, \\ -\log(|\phi_2|), & \text{if} \phi_2 < 0, \\ 0, & \text{otherwise}. \end{cases} \tag{10}$$

Given that images contain other brain regions of similar shape and that image conditions are extremely variant, a set of extra seven features are used to acquire even more descriptive pixel information that can help better distinguishing between the seeked hippocampus section and the alike structure. Figure 5 illustrates the alike structure that is also obtained as result of the preprocessing step. Table 1 shows the comparison of the performance obtained when using seven features and the increased achievement by adding the extra seven.

For the remaining seven features, $f_8, f_9, \cdots, f_{14}$, the information is extracted from the I_{NV} image by following the same process described above, making a total of a 14-D feature vector.

Therefore, one pixel is represented by the 14-D feature space and is denoted by F

$$F = (f_1, f_2, \cdots, f_{14}). \tag{11}$$

2.3. Data Set Creation. The data set, denoted by F_T, is constituted from hippocampal features F_H and nonhippocampal features F_O. F_T is distributed in the following way. First, all features F from hippocampal pixels are collected from all images, acquiring 24,520 hippocampal features. Then, to be sure to obtain a well-balanced data set, the same amount of randomly picked features is collected from nonhippocampal pixels from all images. Thus, the entire data set F_T makes a total of 49,040 features F.

$$F_T = F_H + F_O. \tag{12}$$

Next, data set is complemented with ground truth values, C_1 for hippocampal pixel and C_0 for nonhippocampal pixels. For debugging purposes, data set is augmented with C_1 and C_0 pixel coordinates along with the source image name.

Finally, the data set is randomly split into training (D_{TN}), validation (D_{VL}), and test (D_{TS}) set, distributed in 70%, 20%, and 10%, respectively, making sure the same amount of hippocampal features as well as nonhipocampal ones are is contained in these data sets. A sample visual examination conducted on one of the images is shown in Figure 6.

2.4. Classification. To be able to determine if a pixel belongs to C_1 or C_0, in this work, different ML models are employed: MLP, RBFN, SVMs, and RF.

A MLP [37] is an artificial neural network that overcomes the limitations of least mean square algorithm in solving prediction problems. MLP consists of a set of three types of nodes: input nodes, known as input layer; one or more layers of computation nodes, known as hidden layer; and an output layer. The first layer receives an input signal and propagates it through network; then, each node of the hidden layer

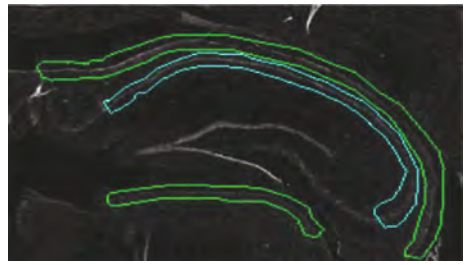

Figure 5: A hippocampus section is framed with cyan colour. Other brain regions that have a similar shape and similar pixel characteristics are framed with green colour.

Table 1: Model comparison using 7 vs. 14 features.

Model	Accuracy using 7 features	Accuracy using 14 features	Accuracy difference
MLP	0.917652	0.940481	+0.022829
RBFN	0.915206	0.931512	+0.016306
Random forest	0.915614	0.937627	+0.022013
SVM lineal	0.899715	0.918875	+0.019160
SVM poly feat	0.907868	0.931512	+0.023644
SVM poly kern	0.912556	0.935997	+0.023441
SVM RBF kern	0.917856	0.939462	+0.021606
Total average accuracy	0.912352	0.933638	+0.021285

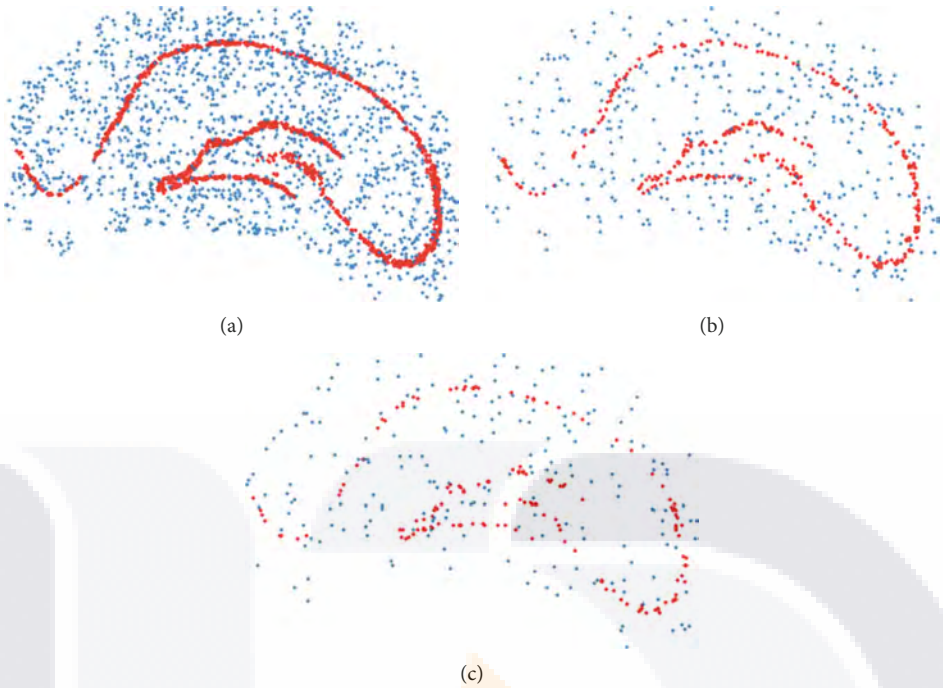

Figure 6: Red dots represent hippocampus pixels and blue dots represent nonhippocampus pixels. (a) Sample image from training set, (b) the same sample image taken from validation set, and (c) the same sample image taken from test set.

executes a nonlinear activation function, and the result is transmitted to the output layer where nodes located here perform a final activation function whose result is interpreted as the probability that the input signal corresponds to a known class.

On the other hand, RBFN was first proposed by Broomhead and Lowe [38] where the hidden layer is trained with an unsupervised algorithm, and the output layer is constructed with a supervised one. The key idea is to transform data points into high-dimensional space with the use of a Gaussian function, so that the transformed points become linearly separable.

SVMs [39] are a category of feed forward networks that can be used for pattern classification and nonlinear regression. SVMs construct a hyperplane as the decision surface in such a way that the margin of separation between positive and negative samples is maximized. There are three main types of SVMs: lineal, polynomials, and radial basis functions.

Random forests [40] are variants of clustering algorithms known as decision trees that perform particularly well on small data sets and like SVMs can perform both classification and regression tasks, but unlike decision trees, RF can limit the sensitivity to small variations in the training data by averaging predictions over many trees.

So that models can be more efficient, techniques such as feature engineering [41] can be used, but looking for maximizing their performance, all D_{TN} features, f_i of F, are used and standardized making them zero mean and unit variance in the following way.

$$f_i = \frac{f_i - \mu_i}{\sigma_i}, \tag{13}$$

where μ_i is the average and σ_i is the standard deviation of the i-th feature. For all these models, only f_i of F features are fed to the models, isolating data that is used for debugging purposes.

In MLP, a supervised learning algorithm known as backpropagation is used for training the layers and the synaptic weight between nodes [37]. With the right choice of weights and with the right number of the hidden nodes, MLP can be used to address classification problems [42]. Hence, the function approximation for classification is defined by a nested set of weighted summations.

RBFN solves the classification problem by proceeding in a hybrid manner. First, an input layer is composed with the same number nodes of the features being evaluated. Then, a hidden layer transforms the given set of nonlinearly separable patterns by applying an unsupervised learning algorithm. Finally, RBFN uses least squares estimation to train the output layer in a supervised manner to solve the classification problem. In RBFN, the function approximation for classification is defined by a single weighted sum [37].

RF is settled on decision trees. A decision tree is a machine learning technique, based on the divide and conquer paradigm where the basic idea is to partition the feature space into patches and to fit a model to a patch. RF creates different trees over the same training data set but provides random subset of features to each of the trees in its building process [43] and uses some aggregation technique, such as majority voting to perform the final classification.

SVMs are a type of binary classifiers that construct a hyperplane as the decision boundary and seek to maximize the distance of positive and negative examples given in a

training set [37]. SVMs use a two-step process on nonlinearly separable data to find the decision boundary. In the first step, a nonlinear transformation is applied to the data; in the second step, the points that constitute the decision boundary are then determined in the transformed space [44].

There are algorithms used in ML that have been proven to maximize predictive output such as ensemble learning [45]; however, this work is constrained to the mentioned ML models with the purpose of evaluating the pixel characterization method itself.

3. Experiments and Results

To measure the algorithmic performance of the proposed method, the before mentioned ML models are trained with D_{TN} set, and in order to find the best performing hyperparameters for each model, Random Search and Grid Search techniques are used. The former is used to reduce the search space and the latter to pinpoint the ideal values. Finally, D_{VL} set is used to assess that the found hyperparameters produce good results and that models are not overfitted.

The final architecture of the MLP model is implemented with TensorFlow and consists of an input layer with 14 nodes and then four fully connected layers made up with 31, 68, 13, and 7 nodes, respectively, with a ReLU activation type for each one of them. Finally, an output layer consisting of 1 node with a sigmoid activation type constitutes its architecture. The model was compiled using ADAM optimizer and binary cross entropy as loss function (LF) and trained over 37 epochs.

The RBFN is built in TensorFlow with the implementation provided by Vidnerová [46]. It was trained with K-Nearest Neighbourhood (K-NN) for the unsupervised algorithm and backpropagation for the supervised. The model has 3 layers as well. The first layer contains 14 input nodes, the second layer has 71 hidden nodes, and the third layer has one output node with a sigmoid activation type. The same σ value is used across Gaussian functions, and it is calculated as follows: $\sigma = d_{\max}/\sqrt{2k}$, where $d_{\max}$ represents the maximum distance between clusters and k is the number clusters, which in turn, match the number of nodes of the second layer. The model used a mean squared error as its LF and RMSprop algorithm for the optimizer and trained over 200 epochs.

The rest of the ML models are built with scikit-learn [47]. The best RF model is set with the following hyperparameters: a gini criterion for measuring the quality of splits; a value of $\sqrt{F_n}$ is set for the maximum features, where F_n represents the number of features; a value of 1 for the minimum samples per leaf and minimum samples for node split; and unset values for max depth, max leaf nodes, and max samples.

Finally, four different SVM models are used. The first one is configured as lineal support vector classification with these hyperparameters: a value of 182 for the regularization parameter (C), a squared hinge LF, and l2 penalty function (PF). The second model is a lineal support vector classification fed with polynomial characteristics, and its hyperparameters are set in the following manner: a value of 172 for C, a 2nd degree polynomial characteristic, and a squared hinge LF and a l2 PF. The third model is set with a 3rd degree polynomial kernel; a value of 2.1 for C; a squared l2 PF; and a γ value of $1/(C_n\sigma^2)$, where C_n is the number of characteristic and σ^2 is the variance; finally, a value of 40 is used for the independent variable (b). The last model uses a radial basis function as kernel type, a squared l2 PF, a value of $1/(C_n\sigma^2)$ for γ parameter, and a value of 182 for C.

After finding the best hyperparameter values for each of the models, the D_{TS} set is employed to objectively compare the performance of the ML models against each other using the following metrics.

On one hand, the receiver operating characteristic (ROC) curve is used to compare the performance of the classification models by plotting two parameters true positive rate (TPR) and false positive rate (FPR). These metrics are defined by

$$\begin{aligned} \mathrm{TPR} &= \frac{\mathrm{TP}}{\mathrm{TP}+\mathrm{FP}}, \\ \mathrm{FPR} &= \frac{\mathrm{FP}}{\mathrm{FP}+\mathrm{TN}}, \end{aligned} \tag{14}$$

where TP means true positives, FN: false negatives, FP: false positives, and TN: true negatives. For this graph, the closer the line is to the upper left corner, the better the classifier is. The ROC curve is displayed in Figure 7.

On the other hand, besides the ROC curve, metrics such as accuracy, precision, recall, and F_1 score are computed with the same purpose. These are defined by

$$\begin{aligned} \mathrm{Accuracy} &= \frac{\mathrm{TP}+\mathrm{TN}}{\mathrm{TP}+\mathrm{TN}+\mathrm{FP}+\mathrm{FN}}, \\ \mathrm{Precision} &= \mathrm{TPR}, \\ \mathrm{Recall} &= \frac{\mathrm{TP}}{\mathrm{TP}+\mathrm{FN}}, \\ F_1\mathrm{score} &= 2\times\left(\frac{\mathrm{precision}\cdot\mathrm{recall}}{\mathrm{precision}+\mathrm{recall}}\right). \end{aligned} \tag{15}$$

To evaluate if the added extra seven features resulted in a performance gain, the same data sets D_{TN}, D_{VL}, and D_{TS} are used for all the ML models but are trained, validated, and tested with only the first seven features, respectively. Table 1 shows that when models use 14 features, all models increase their performance.

Table 2 shows all the metrics described before and the values obtained by each model when using 14 features.

In this context, accuracy is a ratio of correctly predicted observation to the total observations; it works better when there is a symmetric data set and if FP and FN have similar cost. When the cost of FP and FN negatives is different, precision and recall metrics need to be considered. The former is the ratio of correctly predicted positive observations to the total predicted positive observations; ergo, it is a good measure to use when the costs of FP are high. The latter, also known as sensitivity, is the ratio of correctly predicted positive observations to all observations in actual class; hence, recall calculates how many of the actual positives the model captures through labelling it as TP. Finally, F_1 score is the weighted average of precision and recall, and it can be selected

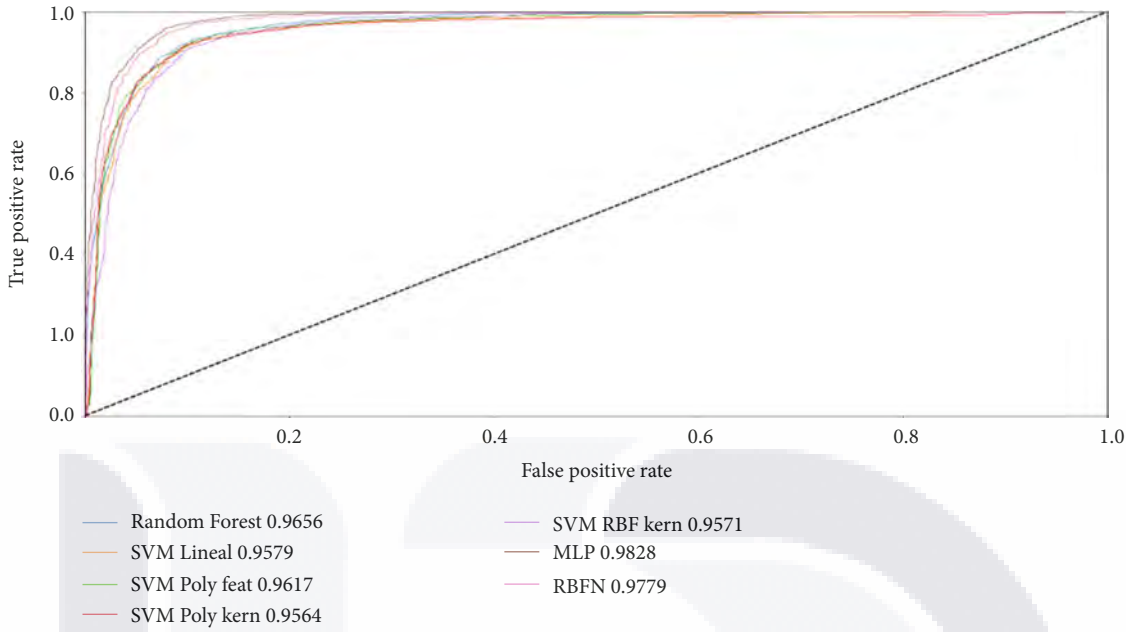

Figure 7: ROC curve. Dotted line from bottom left to upper right represents a strictly random classifier.

Table 2: Model performance.

Model	Accuracy	AUC	F_1 score	Precision	Recall
MLP	0.940481	0.982761	0.941506	0.925926	0.957620
RBFN	0.931512	0.977904	0.933413	0.908565	0.959658
Random forest	0.937627	0.965623	0.938579	0.924842	0.952730
SVM lineal	0.918875	0.957855	0.920368	0.904088	0.937245
SVM poly feat	0.931512	0.961692	0.932934	0.914319	0.952323
SVM poly kern	0.935997	0.956352	0.937325	0.918623	0.956805
SVM RBF kern	0.939462	0.957067	0.940683	0.922444	0.959658

as the main metric to use when a balance between precision and recall is required and there is an uneven class distribution.

Given that our data set is composed of symmetric quantities between C_1 and C_0 samples and assuming that FP and FN have the same cost, accuracy metric could have picked to evaluate models at one sight. Consequently, the model that presents a better performance is MLP; furthermore, this model also scored the highest on AUC, precision, and F_1 score metrics. However, knowing that all these metrics evaluate models from different perspectives and that the context, in a given problem, plays an important part on deciding which model fits a better solution, the interpretation of the other metrics is important when determining the better model. For this reason, if there was a high cost associated with a FN, i.e., a model predicting that a pixel is C_0 when in fact it is C_1, then recall metric should be the main evaluation metric and for such scenario, RBFN would be the best performing model.

4. Discussion

Although good results were obtained with a 7-D and a 5-D feature vectors in the experiments by Marine et al. and Vega et al., respectively, in our experiments, using a 7-D vector did not provide good enough accuracy. This could be, unlike the retinal images that were used in their work, due to the highly variability of the characteristics of the images and the presence of other brain structures that are similar to the seeked hippocampal shape. Nonetheless, when F was increased to 14-D, the experiments yielded an average accuracy increase of 2.1285%. This performance increase is associated to the more complete feature set that was generated with our proposed method and the better pixel characterization.

The best ML models are described next. For our data set, MLP model achieves the highest value in the accuracy metric and correctly predicts C_1 and C_0 pixels 94.0481% of the time. In contrast, when true positive rate needs to be considered cautiously, only 92.5926% C_1 pixels are correctly predicted and when FN has a greater importance in predicting C_1 pixels, MLP achieves a score of 95.7620%. In this regard, RBFN model achieves the best rate with a 95.9658% value. Finally, for properly predicting C_1 and when an equilibrium between FP and FN is sought, the F_1 score metric is picked. In this regard, the best balance is achieved again by MLP model, with a value of 94.1506%.

Despite that techniques such as deep learning can produce models that achieve higher performance on pixel-wise classification tasks [17, 48], and the architecture for these models tends to be of a much larger size, requiring a vast amount of information and special hardware, as GPUs, to account for the complexity and the computations needed in the training and inference phase execution, in a reasonable amount of time. In this regard, the model studied here already achieves and exceeds the accuracy needed by the subject matter expert to locate the hippocampus and can be probably increased by using ensemble methods [45] and feature engineering techniques [41]. The simplicity of the model means it can do, in a timely manner, fast inferences without the need of special hardware, and for its small size, it can even be implemented in portable devices, such as cell phones or tablets.

Even though this paper is for pixel-wise classification, one could argue that having labelled and located the position of hippocampal pixels, it can be considered as segmentation task. Also, knowing that the work from Mesejo et al. [30] is about hippocampus segmentation and that of Senyukova et al. [32] is for brain structure segmentation, with the hippocampus among them, and that both of them use histological images, we could present a second table to easily compare the results. However, Mesejo et al. use a different definition of accuracy of metric that only takes TP % values; Senyukova et al. present just the result of precision metric without giving further information. For these reasons, a fair comparison table cannot be elaborated but their results are written here for the reader's convenience. Mesejo et al. achieve an accuracy of 92.11% and Senyukova et al. accomplish a precision of 60.7194% for hippocampus structure.

5. Conclusions

We showed the robustness of the proposed method by evaluating it with different ML models. Furthermore, by adding samples of every image in the data set, we are increasing the exposure to varying styles of histological images. Likewise, by splitting our data set in 70% for training, 20% for validating, and 10% for testing, we can objectively verify that ML models are not overfitting. Hence, we can conclude that the method will be able to generalize when new images are to be presented.

Not only this, the proposed method described in this work showed that it is possible to do pixel-wise classification for histological images and achieve a remarkable good performance too. Furthermore, the described method can significantly reduce the lengthy effort employed by the subject matter expert on identifying and delimiting the hippocampal region and be considered an adequate operation for substituting a manual classification task.

However, there are some aspects that could be considered for future work. One likely way that performance could be improved is by using an ensemble method algorithm. The shown advantage obtained through the use of a 14-D feature vector could be made more efficient by using PCA or a feature engineering technique that reduces the dimensionality of the feature vector and still obtains a good performance. The current method could also be leveraged by fully automating the pixel-wise classification task by integrating an algorithm that locates the hippocampus bounding box. Another direction for future research could be on the generation of a hippocampus segmentation method to further facilitate the measurement of this area and help automating the quantification of hippocampal volume.

Data Availability

Source images, image pixel labels, data set, and code can be found at the following repository: https://github.com/alfonso-vizcaino/hipp_pixel_classification.

Conflicts of Interest

The authors declare that they have no conflicts of interest.

Acknowledgments

This work is funded in part by the Universidad Autónoma de Aguascalientes under grant PIINF20-6. A. Vizcaíno thanks CONACYT for the scholarship 2020-000013-01NACF-15018 granted to pursue his doctoral studies. Humberto Sossa thanks the Instituto Politécnico Nacional for the support to undertake this research. We also recognize Ma del Rosario Montoya García for her scientific discussions.

References

[1] K. A. Norman, "How hippocampus and cortex contribute to recognition memory: revisiting the complementary learning systems model," *Hippocampus*, vol. 20, no. 11, pp. 1217–1227, 2010.

[2] S. A. Golsorkhdan, M. E. Boroujeni, A. Aliaghaei et al., "Methamphetamine administration impairs behavior, memory and underlying signaling pathways in the hippocampus," *Behavioural Brain Research*, vol. 379, article 112300, 2020.

[3] J. Barnes, J. W. Bartlett, L. A. van de Pol et al., "A meta-analysis of hippocampal atrophy rates in Alzheimer's disease," *Neurobiology of Aging*, vol. 30, no. 11, pp. 1711–1723, 2009.

[4] S. Kaya, H. Yildirim, and M. Atmaca, "Reduced hippocampus and amygdala volumes in antisocial personality disorder," *Journal of Clinical Neuroscience*, vol. 75, pp. 199–203, 2020.

[5] V. Bouët, T. Freret, J. Toutain, D. Divoux, M. Boulouard, and P. Schumann-Bard, "Sensorimotor and cognitive deficits after transient middle cerebral artery occlusion in the mouse," *Experimental Neurology*, vol. 203, no. 2, pp. 555–567, 2007.

[6] R. Gerlai, H. Thibodeaux, J. T. Palmer, M. van Lookeren Campagne, and N. van Bruggen, "Transient focal cerebral ischemia induces sensorimotor deficits in mice," *Behavior Brain Research*, vol. 108, no. 1, pp. 63–71, 2000.

[7] S. Knechtt, S. Hesse, and P. Oster, "Rehabilitation after stroke," *Deutsches Aerzteblatt Online*, vol. 108, no. 6, pp. 600–606, 2011.

[8] R. P. Allred and T. A. Jones, "Maladaptative effects of learning with the less affected forelimb after focal cortical infarcts in rats," *Experimental Neurology.*, vol. 210, no. 1, pp. 172–181, 2008.

[9] J. Yuan, "Neuroprotective strategies targeting apoptotic and necrotic cell death for stroke," *Apoptosis*, vol. 14, no. 4, pp. 469–477, 2009.

[10] Y. Li, X. Wang, N. Li et al., "The NAc lesions disrupted the hippocampus-mPFC theta coherence during intravenous cocaine administration in rats," *Neuroscience Letters*, vol. 729, p. 134986, 2020.

[11] W. Hu, L. Liu, B. Zhao et al., "Use of an automated quantitative analysis of hippocampal volume, signal, and glucose metabolism to detect hippocampal sclerosis," *Frontiers in Neurology*, vol. 9, p. 820, 2018.

[12] A. C. Coan, B. Kubota, F. P. G. Bergo, B. M. Campos, and F. Cendes, "3T MRI quantification of hippocampal volume and signal in mesial temporal lobe epilepsy improves detection of hippocampal sclerosis," *American Journal of Neuroradiology*, vol. 35, no. 1, pp. 77–83, 2014.

[13] J. Wang, A. Jahn-Eimermacher, M. Brückner, C. Werner, K. Engelhard, and S. C. Thal, "Comparison of different quantification methods to determine hippocampal damage after cerebral ischemia," *Journal of Neuroscience Methods*, vol. 240, pp. 67–76, 2015.

[14] T. A. Steve, J. D. Jirsch, and D. W. Gross, "Quantification of subfield pathology in hippocampal sclerosis: a systematic review and meta-analysis," *Epilepsy Research*, vol. 108, no. 8, pp. 1279–1285, 2014.

[15] A. Tashk, M. S. Helfroush, H. Danyali, and M. Akbarzadeh, "An automatic mitosis detection method for breast cancer histopathology slide images based on objective and pixel-wise textural features classification," in *The 5th Conference on Information and Knowledge Technology*, pp. 406–410, Shiraz, 2013.

[16] D. C. Cireşan, A. Giusti, L. M. Gambardella, and J. Schmidhuber, "Mitosis detection in breast cancer histology images with deep neural networks," in *Medical Image Computing and Computer-Assisted Intervention–MICCAI 2013*, Springer, 2013.

[17] D. Cai, X. Sun, N. Zhou, X. Han, and J. Yao, "Efficient mitosis detection in breast cancer histology images by RCNN," in *2019 IEEE 16th International Symposium on Biomedical Imaging (ISBI 2019)*, pp. 919–922, Venice, Italy, 2019.

[18] S. Naik, S. Doyle, M. Feldman, J. Tomaszewski, and A. Madabhushi, *Gland segmentation and computerized Gleason grading of prostate histology by integrating low-high-level and domain specific information*, MIAAB, 2007.

[19] Z. Zeng, W. Xie, Y. Zhang, and Y. Lu, "RIC-Unet: an improved neural network based on Unet for nuclei segmentation in histology images," *IEEE Access*, vol. 7, pp. 21420–21428, 2019.

[20] O. T. Carmichael, H. A. Aizenstein, S. W. Davis et al., "Atlas-based hippocampus segmentation in Alzheimer's disease and mild cognitive impairment," *NeuroImage*, vol. 27, no. 4, pp. 979–990, 2005.

[21] F. Van der Lijn, T. den Heijer, M. M. B. Breteler, and W. J. Niessen, "Hippocampus segmentation in MR images using atlas registration, voxel classification, and graph cuts," *NeuroImage*, vol. 43, no. 4, pp. 708–720, 2008.

[22] A. R. Khan, N. Cherbuin, W. Wen, K. J. Anstey, P. Sachdev, and M. F. Beg, "Optimal weights for local multi-atlas fusion using supervised learning and dynamic information (Super Dyn): validation on hippocampus segmentation," *NeuroImage*, vol. 56, no. 1, pp. 126–139, 2011.

[23] T. A. Steve, C. L. Yasuda, R. Coras et al., "Development of a histologically validated segmentation protocol for the hippocampal body," *NeuroImage*, vol. 157, pp. 219–232, 2017.

[24] Y. Hao, T. Wang, X. Zhang et al., "Local label learning (LLL) for subcortical structure segmentation: application to hippocampus segmentation," *Human Brain Mapping*, vol. 35, no. 6, pp. 2674–2697, 2014.

[25] P. Coupé, J. V. Manjón, V. Fonov, J. Pruessner, M. Robles, and D. L. Collins, "Nonlocal patch-based label fusion for hippocampus segmentation," *Lecture Notes in Computer Science*, vol. 6363, pp. 129–136, 2010.

[26] K. Richards, C. Watson, R. F. Buckley et al., "Segmentation of the mouse hippocampal formation in magnetic resonance images," *NeuroImage*, vol. 58, no. 3, pp. 732–740, 2011.

[27] M. Chupin, E. Gérardin, R. Cuingnet et al., "Fully automatic hippocampus segmentation and classification in Alzheimer's disease and mild cognitive impairment applied on data from ADNI," *Hippocampus*, vol. 19, no. 6, pp. 579–587, 2009.

[28] V. Dill, A. R. Franco, and M. S. Pinho, "Automated methods for hippocampus segmentation: the evolution and a review of the state of the art," *Neuroinformatics*, vol. 13, no. 2, pp. 133–150, 2015.

[29] N. Khalili, N. Lessmann, E. Turk et al., "Automatic brain tissue segmentation in fetal MRI using convolutional neural networks," *Magnetic Resonance Imaging*, vol. 64, pp. 77–89, 2019.

[30] P. Mesejo, R. Ugolotti, S. Cagnoni, F. Di Cunto, and M. Giacobini, "Automatic segmentation of hippocampus in histological images of mouse brains using deformable models and random forest," in *2012 25th IEEE International Symposium on Computer-Based Medical Systems (CBMS)*, pp. 1–4, Rome, 2012.

[31] Allen Institute for Brain Science, "Allen reference atlases," http://mouse.brain-map.org, 2004-2006.

[32] O. V. Senyukova, A. S. Lukin, and D. P. Vetrov, "Automated atlas-based segmentation of Nissl-stained mouse brain sections using supervised learning," *Programming and Computing Software*, vol. 37, no. 5, pp. 245–251, 2011.

[33] T. Riklin-Raviv, N. Sochen, N. Kiryati et al., "Propagating distributions for segmentation of brain atlas," in *2007 4th IEEE International Symposium on Biomedical Imaging: From Nano to Macro*, pp. 1304–1307, Arlington, VA, USA, 2007.

[34] R. Vega, G. Sanchez-Ante, L. E. Falcon-Morales, H. Sossa, and E. Guevara, "Retinal vessel extraction using lattice neural networks," *Computers in Biology and Medicine*, vol. 58, pp. 20–30, 2015.

[35] D. Marín, A. Aquino, M. Gegundez-Arias, and J. Bravo, "A new supervised method for blood vessel segmentation in retinal images by using gray-level and moment invariants-based features," *IEEE Transactions on Medical Imaging*, vol. 30, no. 1, pp. 146–158, 2011.

[36] M. K. Hu, "Visual pattern recognition by moment invariants," *IRE Transactions on Information Theory*, vol. 8, pp. 179–187, 1962.

[37] S. Haykin, *Neural Networks and Learning Machines, Third Edition*, Prentice Hall, 2008.

[38] D. Broomhead and D. Lowe, "Multivariable functional interpolation and adaptive networks," *Complex Systems*, vol. 2, pp. 321–355, 1988.

[39] C. C. Aggarwal, *Neural Networks and Deep Learning. A Textbook*, Springer, 2018.

[40] L. Breiman, "Random forests," *Journal Machine Learning archive*, vol. 45, no. 1, pp. 5–32, 2001.

[41] A. Onan, S. Korukoğlu, and H. Bulut, "A hybrid ensemble pruning approach based on consensus clustering and multi-

objective evolutionary algorithm for sentiment classification," *Information Processing & Management*, vol. 53, no. 4, pp. 814–833, 2017.

[42] M. Kubat, *An Introduction to Machine Learning, Second Edition*, Springer, 2017.

[43] L. Igual and S. Seguí, *Introduction to Data Science a Python Approach to Concepts Techniques and Applications, Second Edition*, Springer, 2017.

[44] W. Ertel, *Introduction to Artificial Intelligence, Second Edition*, Springer, 2017.

[45] A. Onan, "On the performance of ensemble learning for automated diagnosis of breast cancer," *Artificial Intelligence Perspectives and Applications*, vol. 347, pp. 119–129, 2015.

[46] P. Vidnerová, *RBF-Keras: An RBF Layer for Keras Library*, 2019, https://github.com/PetraVidnerova/rbf_keras.

[47] F. Pedregosa, G. Varoquaux, A. Gramfort et al., "Scikit-learn: Machine Learning in Python," *Journal of Machine Learning Research*, vol. 12, pp. 2825–2830, 2011.

[48] W. Ouyang, A. Aristov, M. Lelek, X. Hao, and C. Zimmer, "Deep learning massively accelerates super-resolution localization microscopy," *Nature Biotechnology*, vol. 36, no. 5, pp. 460–468, 2018.

3.3 Summary

The information presented in this chapter demonstrates a trustworthy process that can work with histological images of hippocampus. Therefore, it was made possible the achievement of the first research objective, finding a machine learning model capable of identifying the hippocampus with an accuracy greater than 90% in histological images.

CHAPTER IV - IMPLEMENTING A SYSTEM FOR HIPPOCAMPUS MEASURMENT.

4.1 Introduction.

In this chapter it is described a system that is designed and built to facilitate hippocampus measurement based on the best machine learning model found previously, therefore effectively satisfying the second research objective. In addition, this section presents some images of the key functionalities built-in in the application.

4.2 System implementation.

For building a system that is capable of processing images to help laboratory technicians as well as students identifying and measuring hippocampus, several factors were considered but the most important aspects to decide how the system was built are: programing language and technology used for the machine learning model, time available for system development, cost and available technological infrastructure, and the familiarity of users with technology and computer systems in general.

Given that the machine learning model was built with TensorFlow using python programming language, the most straight forward way to use this model would be in the direction of porting the code to a server, were a client-server pattern system could fit the needs. However, because of cost constraints involved with the implementation of such infrastructure and the time available to develop the client and backend code applications, this option was discarded.

The venue for using a mobile application was then explored knowing that TensorFlow provides utility packages to convert models for usage in mobile applications. It was also identified that building a mobile application would not incur in addition cost compared to maintaining client-server infrastructure and that users are familiarized with mobile applications. Furthermore, because of the familiarity with of these technologies, it was determined that developing this application would be feasible from a time constrain perspective.

With these features in mind, it was decided to build a mobile application which has the advantage of taking photographs of histological images in place and using them to directly feed the system were students and laboratory technicians can use them right away without the need of transmitting them from one system to other.

The system Hippocampus Measurement on Histological Images, HMoHI, was built using Android technology and to incorporate the machine learning model into the Android system TensorFlow Lite was used with the help of NativeJDK to integrate the C code generated by the TensorFlow packages.

To have the ability of identifying and measuring hippocampus, several features were added to make it more functional. HMoHI lets the user establish image dimension to properly calibrate itself and, out of this information, it establishes a pixel scale that is used for area extrapolation. It allows the user to work with only a section of the image, it permits to modify the predicting confidence threshold that exclude/include hippocampus areas and it can also send the measurement results through email. The measurement results were compared with ImageJ, a popular software that is used to manually measure hippocampus images, obtaining remarkably good results.

The system HMoHI can be used by mobile phones with Android version 9 or higher. It was registered with INDAUTOR under registration number 03-2021-012711394300-01 as can be seen in Figure IV-1. At the time of writing, the system is only available to white-listed users in the Google Play Store. Because of intellectual property protection, no application design diagrams are included here.

CERTIFICADO

Registro Público del Derecho de Autor

Para los efectos de los artículos 13, 162, 163 fracción I, 164 fracción I, 168, 169, 209 fracción III y demás relativos de la Ley Federal del Derecho de Autor, se hace constar que la **OBRA** cuyas especificaciones aparecen a continuación, ha quedado inscrita en el Registro Público del Derecho de Autor, con los siguientes datos:

AUTORES:	SANCHEZ CRUZ HERMILO VIZCAINO POBLANO ALFONSO
TITULO:	HMOHI
RAMA:	PROGRAMAS DE COMPUTACION
TITULARES:	SANCHEZ CRUZ HERMILO VIZCAINO POBLANO ALFONSO

Con fundamento en lo establecido por el artículo 168 de la Ley Federal del Derecho de Autor, las inscripciones en el registro establecen la presunción de ser ciertos los hechos y actos que en ellas consten, salvo prueba en contrario. Toda inscripción deja a salvo los derechos de terceros. Si surge controversia, los efectos de la inscripción quedarán suspendidos en tanto se pronuncie resolución firme por autoridad competente.

Con fundamento en los artículos 2, 208, 209 fracción III y 211 de la Ley Federal del Derecho de Autor; artículos 64, 103 fracción IV y 104 del Reglamento de la Ley Federal del Derecho de Autor; artículos 1, 3 fracción I, 4, 8 fracción I y 9 del Reglamento Interior del Instituto Nacional del Derecho de Autor, se expide el presente certificado.

Número de Registro: **03-2021-012711394300-01**

Ciudad de México, a 23 de febrero de 2021

EL DIRECTOR DEL REGISTRO PÚBLICO DEL DERECHO DE AUTOR

JESUS PARETS GOMEZ

SECRETARÍA DE CULTURA
INSTITUTO NACIONAL DEL DERECHO DE AUTOR
DIRECCIÓN DE REGISTRO PÚBLICO DEL DERECHO DE AUTOR

CULTURA | INDAUTOR

Figure IV-1. INDAUTOR certificate

4.3 System usage.

In this section it is briefly explained the steps for accessing the main functionality provided in HMoHI.

1. Clicking on the camera button and selecting a hippocampal histology image will make program start uploading and pre-processing the image. This step may take a few moments. These steps are ilustrated in Figure IV-2

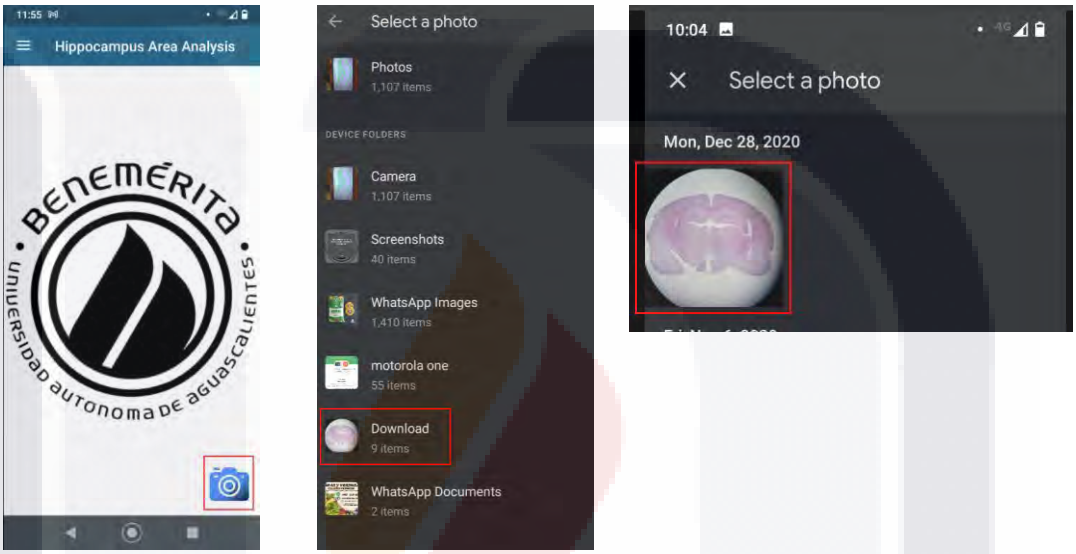

Figure IV-2. Image selection process. Source own creation

2. When finished, the program will show an image as in the Figure IV-3

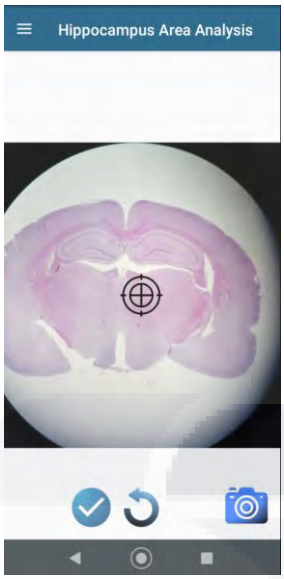

Figure IV-3. Preprocessed image. Source own creation.

3. To start system calibration, the sytem needs to be fed with the measurements of a know portion of the tissue. Figure IV-4 shows a sequence of images that show how to instruct the system with the known portion of tissue.

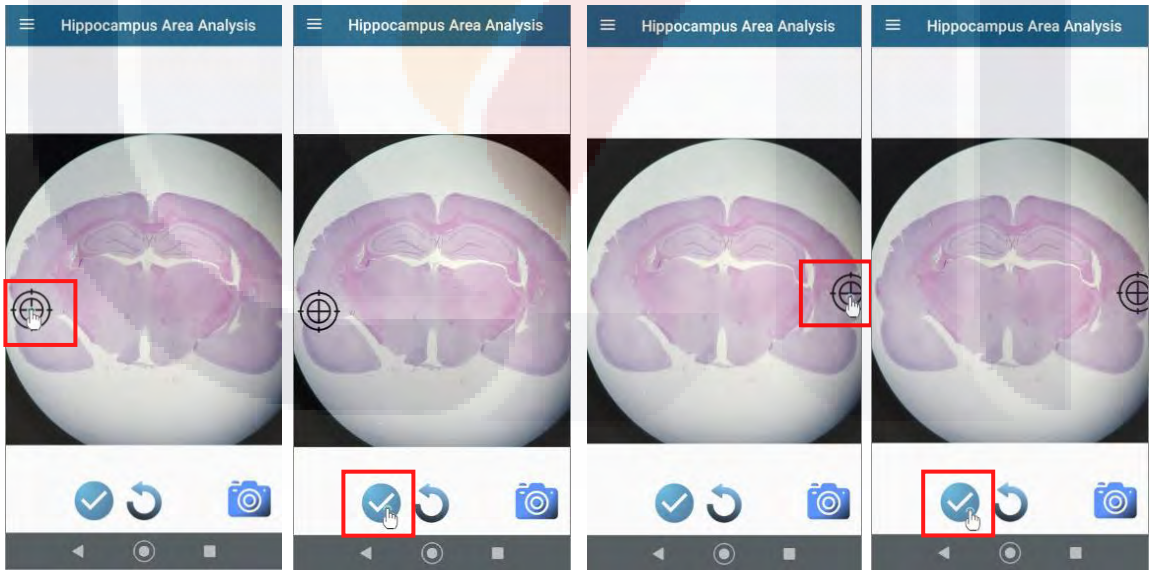

Figure IV-4. Calibration step 1. Selecting a known distance from a portion of a tissue. Source own creation.

4. Click again on the accept button to confirm the trace and capture size of the selected portion in millimeters. When done, clicking on "Accept" button will finish system calibration. This is reflected in Figure IV-5.

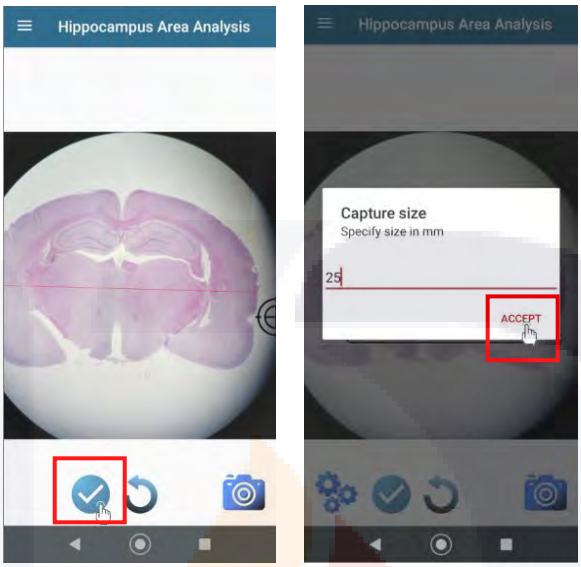

Figure IV-5. Calibration step 2.Capturing the known measurement portion of a tissue. Source own creation.

5. The program will display the region of interest window. Make a zoom gesture on the image to enlarge it enough so it fits a hippocampal section as shown in Figure IV-6

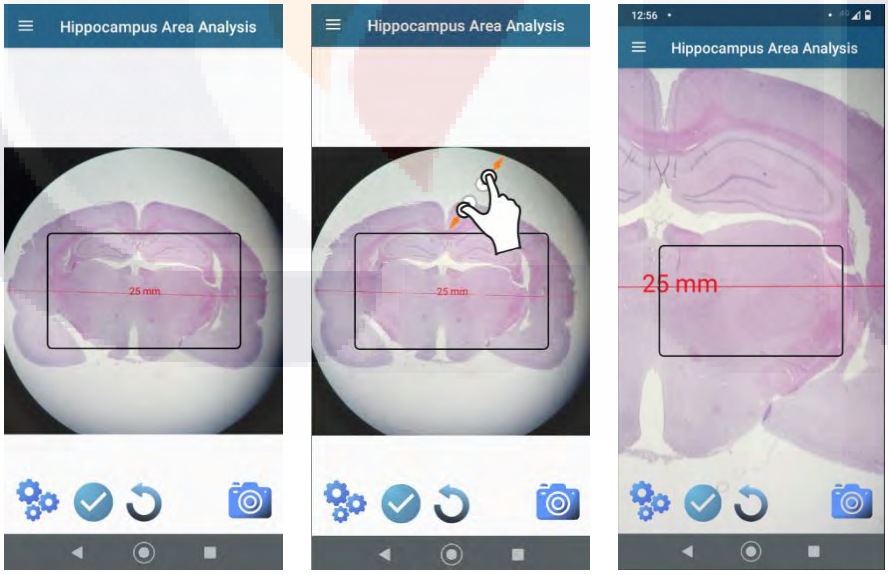

Figure IV-6. Locating region of interest.Source own creation.

6. In Figure IV-7 The user drags the region of interest window over the hippocampus as shown in the figures below. When finished, click on the process button.

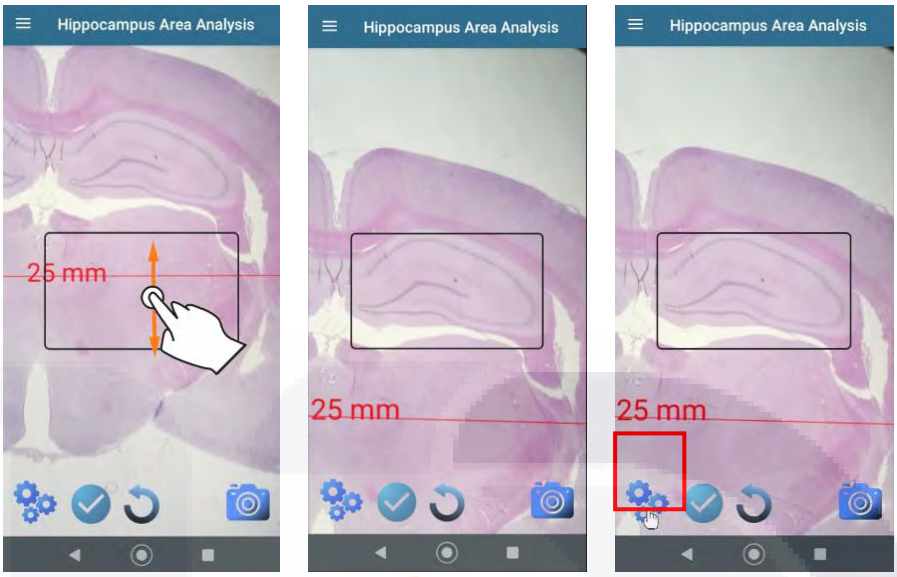

Figure IV-7. Selecting region of interest. Source own creation.

7. The program will show the region to analyze. Touch the screen to display the controls and click the button to start the image analysis like displayed in Figure IV-8

Figure IV-8. Starting hippocampus identification. Source own creation.

8. After a few moments it will show the segmented hippocampus in green color. Touch the screen again to display the controls for error correction, segmentation adjustment, probability map, and analysis mailing. Figure IV-9 shows the information on the measured area denoted with the orange color.

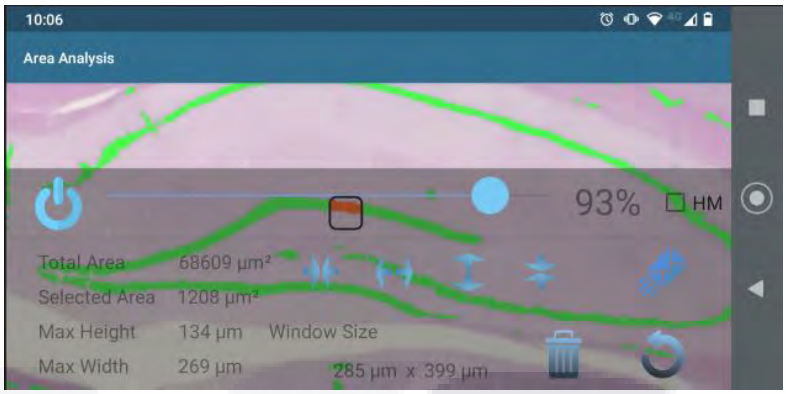

Figure IV-9. Area measurement information and controls. Source own creation.

4.4 Summary.

With the implementation of HMoHI, it is accomplished the second research objective of creating a system that can accurately measure the hippocampus area. In practice, it is also observed that the usage of the application is not as seamless as intended due to some small mobile screen sizes.

CHAPTER V - DL MODEL TO IDENTIFY NEURONS.

5.1 Introduction.

This section describes the research performed to create a prediction model, in this case implemented with deep learning, skilled in identifying neuron cells with an accuracy of more than 90%. The deep learning model is also evaluated on different datasets to verify its generalizations capabilities under different cell types.

5.2 Article.

Expert Systems With Applications 208 (2022) 118090

Contents lists available at ScienceDirect

Expert Systems With Applications

journal homepage: www.elsevier.com/locate/eswa

Neuron cell count with deep learning in highly dense hippocampus images

Alfonso Vizcaíno [a], Hermilo Sánchez-Cruz [a,*], Humberto Sossa [b], J. Luis Quintanar [c]

[a] Department of Computer Science, Universidad Autónoma de Aguascalientes, Aguascalientes, México
[b] Department of Computer Science, Instituto Politécnico Nacional-Centro de Investigación en Computación, Av. Juan de Dios Batiz S/N, Gustavo A. Madero, 07738 México, Distrito Federal, Mexico
[c] Department of Physiology and Pharmacology, Universidad Autónoma de Aguascalientes, Avenida Universidad 940, C.U, 20100 Aguascalientes, México

ARTICLE INFO

Keywords:
Histological images
Deep learning
Neuron cell count
Hematoxylin Eosin

ABSTRACT

Neural cell counting is one of the ways in which damage caused by neurodegenerative diseases can be assessed, but it is not an easy task when it comes to neuronal counting in the most densely populated areas of the hippocampus. In this regard, this work presents a leveraged deep learning (DL) model, an innovative way to treat histological images and their correspondent ground truth information, where highly dense cell population with fuzzy cell boundaries and low image quality exist. The proposed model achieves state-of-the-art results in the neuron cell count problem for the highly dense area of DG and CA hippocampus regions, by making use of better pixel characterization which in turn also delivers a more efficient model size and reduces training time. Furthermore, we show that the proposed image treatment can be applied to other DL models and help them to obtain a 12% performance increase. Also, we demonstrate that with the proposed methodology, an innovative and reliable way to count neural cells with poor image condition in histological analysis has been carried out.

1. Introduction

Neurodegenerative disorders are at the core of several studies characterized by neuronal loss (Mattson, 2000; Procaccini et al., 2016; Roy Sarkar & Banerjee, 2019; Zecca, Youdim, Riederer, Connor, & Crichton, 2004). Thus, accurate quantification of neurons is critically important not only in the understanding of physiological and psychological performance of some neuropathological processes, such as Alzheimer's disease (Yang, Mufson, & Herrup, 2003; Zarow, Lyness, Mortimer, & Chui, 2003) and Parkinson's disease (Giguère, Burke Nanni, & Trudeau, 2018) but in the investigation of neuroprotective drugs and the evaluation of the efficiency of treatment strategies in pre-clinical studies (Li et al., 2015; Zhu, Fotinos, et al., 2015).

Ischemic strokes, in which blood flow to the brain is blocked, are among those sources of damages that lead to these type of disorders (Radovsky, Katz, Ebmeyer, & Safar, 1997; Sugawara et al., 2000). To evaluate the harm caused by ischemic strokes it is imperative to generate reproducible brain damage, which is done with the establishment of multiple experimental models (García & Quintanar, 2020; Uluç, Miranpuri, Kujoth, Aktüre, & Başkaya, 2011) that assist the investigation of cerebral alteration and neural cell death and where immunohistochemical analysis plays an undeniable role in cell counting to measure damage of stroke and efficiency of treatments (Ke et al., 2020; Komur et al., 2014; Schuhmann, Gunreben, Kleinschnitz, & Kraft, 2016; Yata et al., 2007).

Zhu, Liu, Zou, and Torbey (2015) identified several counting strategies in the field of neuroscience research, such as unbiased stereological methods, flow cytometry, manual counting and automatic or semi-automatic counting methods.

On one hand, unbiased stereology methods tend to have higher technical requirements and the dependability of its results could be attenuated because of tissue deformation after the histological processing, staining of the sections and changes in thickness if the right approach is not considered (Dorph-Petersen, Nyengaard, & Gundersen, 2001; Zhu, Liu, et al., 2015) and thus, these methods are used less frequently than manual counting. On the other hand, counting cells within a defined region of interest (ROI) can introduce a strong bias to study results because neuronal cell death does not occur homogeneously since neurons are not equally sensitive to ischemic stress. Therefore, neuronal cell count should not be restricted to a single counting window but extended to multiple ROIs (Wang et al., 2015).

The above, coupled with the overwhelming labor of performing the

* Corresponding author.
E-mail addresses: alfonso.vizcano@gmail.com (A. Vizcaíno), hermilo.sanchez@edu.uaa.mx (H. Sánchez-Cruz), hsossa@cic.ipn.mx (H. Sossa), jlquinta@correo.uaa.mx (J.L. Quintanar).

https://doi.org/10.1016/j.eswa.2022.118090
Received 2 November 2021; Received in revised form 4 July 2022; Accepted 4 July 2022
Available online 8 July 2022

manual counting task and the need for subject matter experts that can correctly distinguish the right cells are causing automated methods to become popular. Inglis et al. (2008) created an automated neuron recognition algorithm capable of obtaining the x, y position of neurons within Nissl-stained images of the cerebral cortex of monkey brains by applying a combination of image segmentation and machine learning techniques, correctly identifying 86 ± 5% neurons with 15 ± 8% error (mean ± standard deviation). Meanwhile, Woeffler-Maucler, Beghin, Ressnikoff, Bezin, and Marinesco (2014) presented an automated immunohistochemical method to quantify neuronal density in confocal images of brain sections employing fluorescent antibodies performing a double-labeling technique that highlighted neural and non-neural nucleus and using image processing techniques such as band pass filters, auto thresholding and morphological operations. The automatic method developed by Attili, Silva, Nguyen, and Ascoli (2019) quantified the distribution of cells making use Nissl-stained images of Allen Brain Atlas by creating image segmentation pipelines that involved image processing techniques reaching an average absolute difference at the sub-region level of less than 15%, however, the highly dense regions of the principal layers of hippocampus, Cornu Ammonis (CA) and Dentate Gyrus (DG), where excluded. Štajduhar, Džaja, Judaš, and Lončarič (2019) were able to correctly distinguish 95.41% of neurons in NeuN-stained images of adult human prefrontal cortex images with an anisotropic diffusion technique.

Recently, with the advent of more computing power, new technologies are emerging such as Deep Learning (DL) which is making its way in multiple medical fields (Ravì et al., 2017) such as cancer detection (Cireşan, Giusti, Gambardella, & Schmidhuber, 2013; Hamed, Marey, Amin, & Tolba, 2020; Shen et al., 2019; Xu et al., 2016), glaucoma diagnosis (Chai, Liu, & Xu, 2018; Serte & Serener, 2019; Song, Lai, & Su, 2021), heart disease and failure prediction (Ali et al., 2020; Kwon et al., 2019; Potes, Parvaneh, Rahman, & Conroy, 2016), among others (Chen, Dou, Yu, Qin, & Heng, 2018; Li et al., 2019; Serte & Demirel, 2021) and where cell counting is not the exception.

Jiang, Liu, Yan, Gu, and Jiang. (2021) performs blood cell count with an attention-guided deep learning method derived from YOLO architecture (Redmon, Divvala, Girshick, & Farhadi, 2016) and Chowdhury, Roberson, Hukkoo, Bodapati, and Cappelleri (2020) use an optimized version of it, being capable of identifying and counting thrombocytes, red and white blood cells. Likewise, counting retinal ganglion cell axons is done by Ritch et al. (2020) in optic nerve tissue images by making an adaptation of a well-known Convolutional Neural Network (CNN) noted as U-Net (Ronneberger, Fischer, & Brox, 2015). Soltanian-Zadeh, Sahingur, Blau, Gong, and Farsiu (2019) attains the identification and segmentation of active neurons by utilizing a variety of two-photon calcium images with STNeuroNet, an extension of DenseVNet (Gibson et al., 2018) and reaching scores of 0.86, 0.88, 0.87 for recall, precision and F_1 metrics, respectively. Iqbal, Sheikh, and Karayannis (2019) created a DL architecture based in Faster RCNN (Ren, He, Girshick, & Sun, 2017) to detect neurons and tested it against human brain images with highly dense cell population of fluorescently-tagged CaMKIIa, achieving a mean average-precision score of 0.75 and a mean precision of 0.87, also, Iqbal et al. achieved mean average-precision of 0.9 in a neural dataset of GAD1 and VGAT *in situ* hybridized brain sections where these markers cover about 20% of all cortical neurons. And other works (Hagos, Narayanan, Akarca, Marafioti, & Yuan, 2019; Xie, Noble, & Zisserman, 2018) perform cell counting on synthetic dataset and images from patients with cancer, respectively.

It is known that staining neurons with NeuN or fluorescent antibodies can facilitate discrimination of neurons, glia cells or nucleus much better than Hematoxylin-eosin (H-E). NeuN and fluorescent antibodies create better marked cells by giving them greater intensity and more defined contours, however, the time-consuming aspect in the preparation of the tissue, as opposed to the easiness of the staining procedure, familiarity of use and least expensiveness of H-E and Nissl antigen, makes both widely used in clinical and research labs around the world (Duregon et al., 2014; Inglis et al., 2008; Iqbal et al., 2019; Nuovo et al., 2021; Ochi et al., 2014; Yang, Song, Li, & Liang, 2014; Yavuz et al., 2001; Zhu, Liu, et al., 2015). But any of these techniques create a vast variability of color in cell staining, and the presence of damaged in tissue surfaces, the existence of overlapping or partial cells and image quality such as lighting and focus conditions derived of its acquisition, they are all a major source of noise in manual and automatic counting.

With all of this, there is still a need for addressing the highly cell clumped areas of CA (1 and 3) and DG region of hippocampus in H-E-stained images that also tackles the issuances produced by immunohistochemical procedure to count cells more accurately in an automatic way.

Therefore, in this work we propose a new approach to perform neural cell counting for highly dense and low quality images using a DL architecture trained with hippocampus histological images reaching state of the art performance.

The remainder of this paper is organized as follows: Section 2 describes the materials used in this study. Section 3 presents our methodology. Section 4 describes experiments and results and discusses the results obtained by the models and finally, Section 5 presents conclusions.

2. Materials

2.1. Animals

Male Sprague-Dawley rats weighing 270 to 330 g were used to collect images for this study. The rats were provided by the animal farm of Physiology and Pharmacology Department of the Autonomous University of Aguascalientes. They were maintained at 22 °C with a 12-hour light–dark cycle with free access to food and water.

2.2. Animal preparation

The rats were divided into four groups: 1) Normal control group, 2) ischemic group treated with sterile saline solution (IR + SS), 3) ischemic group treated with leuprolide acetate (IR + LA) and 4) Sham group, which were rats that underwent of surgery but no ischemic stroke. All surgeries were performed under general anesthesia of ketamine and xylazine hydrochloride. The rats were used and treated in accordance with the Institutional Welfare Standards (Autonomous University of Aguascalientes) and every effort was made to avoid suffering and to avoid unnecessary testing. To know more details of how the cerebral ischemia and reperfusion procedure was carried out, the reader can consult García and Quintanar (2020) work.

To IR + LA group, leuprolide acetate was given at a dose of 10 μg/kg in the following way: on the day of surgery and the two consecutive days, a dose was injected intramuscularly and then every third day until 27th day. For the IR + SS group a dose of 100 μl of sterile saline was injected with the same frequency as IR + AL. On 30th day the animals were euthanized. The brains were extracted to perform histological techniques.

2.3. Tissue preparation

Rats were anesthetized using ketamine and xylazine hydrochloride and then, transcardially were perfused with 0.1 M phosphate buffer, followed by freshly prepared 4% paraformaldehyde in 0.1 M phosphate buffer. Brains were subsequently removed, immersed in the same fixative for 5 h at 4° C and processed for paraffin embedding. Serial coronal sections of approximately 6μ thick were obtained from each brain considering Bregma − 3.3 mm. The slides were dewaxed, rehydrated and H-E staining was performed.

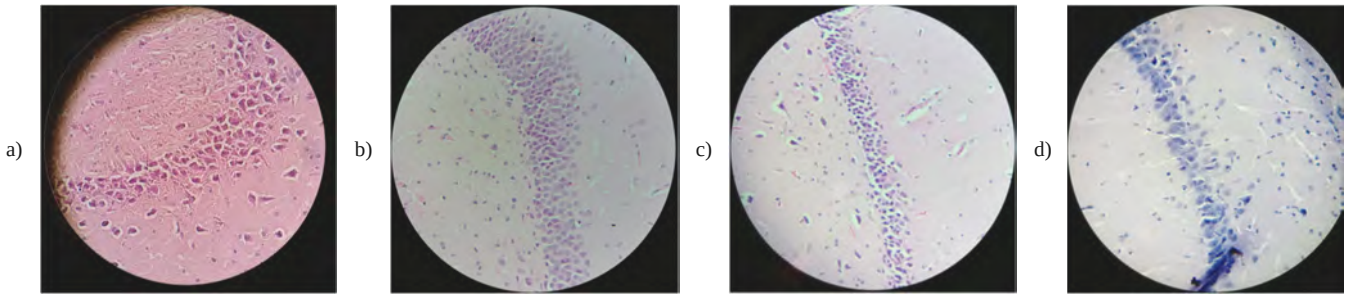

Fig. 1. Sample coronal sections of different rat brains digitized at 40x magnification and stained with hematoxylin and eosin. a) Image from a Control group rat depicting a CA3 hippocampus section. b) Image from an IR + LA group rat depicting a DG hippocampus section. c) Image from an IR + SS group rat depicting a DG hippocampus section. d) Image from a Sham group rat depicting a CA1 hippocampus section.

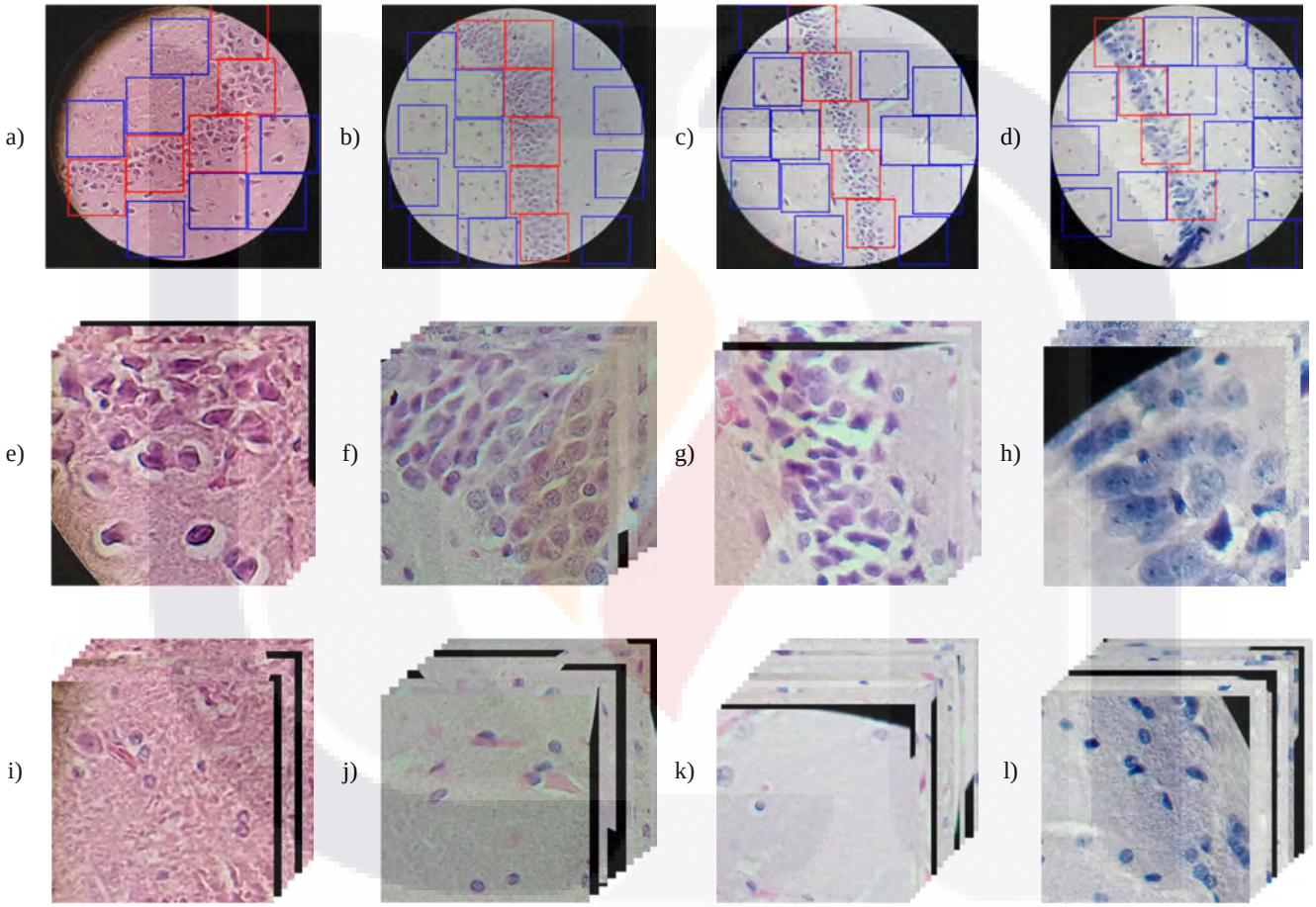

Fig. 2. a-d) The same images as in Fig. 1. Red squares show the position of the extracted images belonging to a highly dense hippocampus region and blue squares show the position of the nearby region of interest. e-h) Images of 512 × 512 showing cells from highly dense region portraying wide differences in morphology and color. i-l) Images of 512 × 512 showing ample difference in tissue textures and cells from the nearby region of interest. (For interpretation of the references to color in this figure legend, the reader is referred to the web version of this article.)

2.4. Image acquisition

Tissue containing CA1, CA3, and DG region of hippocampus section was digitized from an optical microscope with a magnifying glass of 40x, using an LGE LM-X520 camera model that was configured with an ISO speed rating of 100, a focal length of 3.5 mm and a variable exposure time ranging from 1/60 s to 1/30 s. Each image was captured at a resolution of 4161 × 3120 pixels, with an average size of 3 megabytes, a resolution of 72 ppi and, was saved originally in JPEG format with a compression value of 96.

In total 43 images were obtained and are distributed in the following way: 22 images come from Control group rats, 11 images come from IR + LA group, 6 images come from IR + SS group and 4 come from Sham group. It is worth noting that since tissue is stained with H-E, cell characteristics and morphology is not directly affected by the process and the treatment applied to rats, but the amount of cells that are present in images might be associated with them. The amount of acquired images is given by the availability of histological samples at image acquisition time. A representative sample of these groups is shown in Fig. 1.

To better manage and train DL models, 516 images of size 512 × 512 pixels were extracted out of the 43 original images. We saw that this

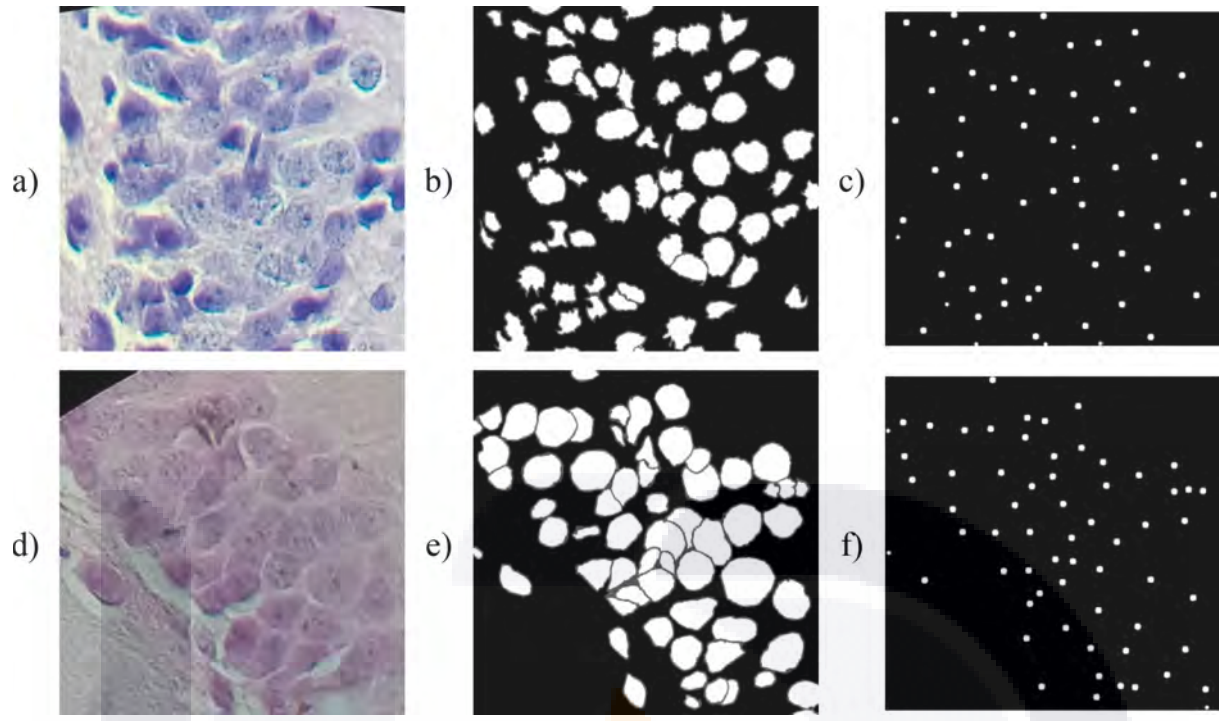

Fig. 3. Ground Truth Enhancement Process for two images with a highly cell population and blurry boundaries. Original images a) and d). Manually annotated ground truth images b) and e). GTE images c) and f).

image size is large enough to contain most of the region of interest DG, CA1 and CA3, where the very crowded cell area is located and without having to cut more cells. On the other hand, if a smaller image size were used, a considerably greater effort to acquire the full number of cells per image would be necessary.

The extraction was conducted in the following way. First, 165 images of the highly dense DG, CA1 and CA3 regions were obtained. These images have 44 $\pm$ 20 cells (mean $\pm$ standard deviation) per image. Then, because of cells taking up most of the space of the image, to make sure we provide the DL models with enough information of tissue background and help it properly identify cells, another 351 images were randomly obtained from the nearby area of the region of interest. These images have 8 $\pm$ 6 cells (mean $\pm$ standard deviation) per image. Fig. 2 shows images extracted from the region of interest, its surroundings and tissue texture.

Given that H-E stains neurons, astrocytes, oligodendrocytes, microglia alike and because of the nature of cells observed at the acquired magnification level, mistakes can be committed when trying to make distinctions between them. For this reason, in this study all cells were manually segmented with no differentiation between them to create the ground truth. A technician familiarized with neurons in H-E hippocampus images, manually delineated each cell using a digitizing Wacom CTL472 tablet to precisely annotate each cell using special editing software Krita on a 25″ monitor with a 160x digital magnification. The technician was asked to carefully treat areas of clustered cells, especially where cells overlap or touch each other. To make it easier for DL models to distinguish one cell from another, the overlapped cells edges were not marked for avoid feeding the DL models with ambiguous information and, to better delineate the cell bodies, the overlapping pixel was assigned to the cell that appeared to be on top in the 3-D structure. After the manual annotation was finished, the quality control was performed by an expert histologist with years of experience analyzing neuron cells who reviewed all images and corrected any issues in the segmentation process. A sample image of ground truth annotations can be seen in Fig. 3b) and e).

3. Methodology

In this section we start by describing the treatment given to the dataset and the image preprocessing step to help DL models to reach high performance. Next, we explain how we did dataset splitting. Finally, we talk about the proposed DL model and the applied modifications to enhance its learning capabilities.

3.1. Data preparation

Unlike other works (Chowdhury et al., 2020; Jiang et al., 2021) where cell counting is achieved by training CNN models with bounding boxes that wraps around cell bodies, in this work, we use semantic segmentation to teach the model what constitutes a cell and where it is located.

Semantic segmentation using histological images in image processing and DL projects are a naturally high difficult challenge. The histological process itself creates conditions where there is: a lack on a specific color for identifying cells, fuzziness on cell boundaries, variability of cell morphology, difference in tissue texture and presence of marks, scraps and tears in tissue. In addition, we also have to include the complexity added by the digitization process itself where lighting effects creates some images brighter than others, and the actual position of the camera can create out of focus images or artifacts whose size differs from other images. Furthermore, we deal with images where highly clumped cell areas exists and which hardens the identification task due to cells occlusion thus impacting on a reliable counting task. Fig. 2 shows some of these conditions.

For the reasons explained above, we conduct two strategies to increase performance predictability of DL models, named: Ground Truth Enhancement (GTE) process and Image Condition Enhancement (ICE) process.

3.1.1. Ground truth enhancement process

Softness in cell borders, cell occlusion and blurry images, create excessive noise to DL models resulting in an extremely low performance

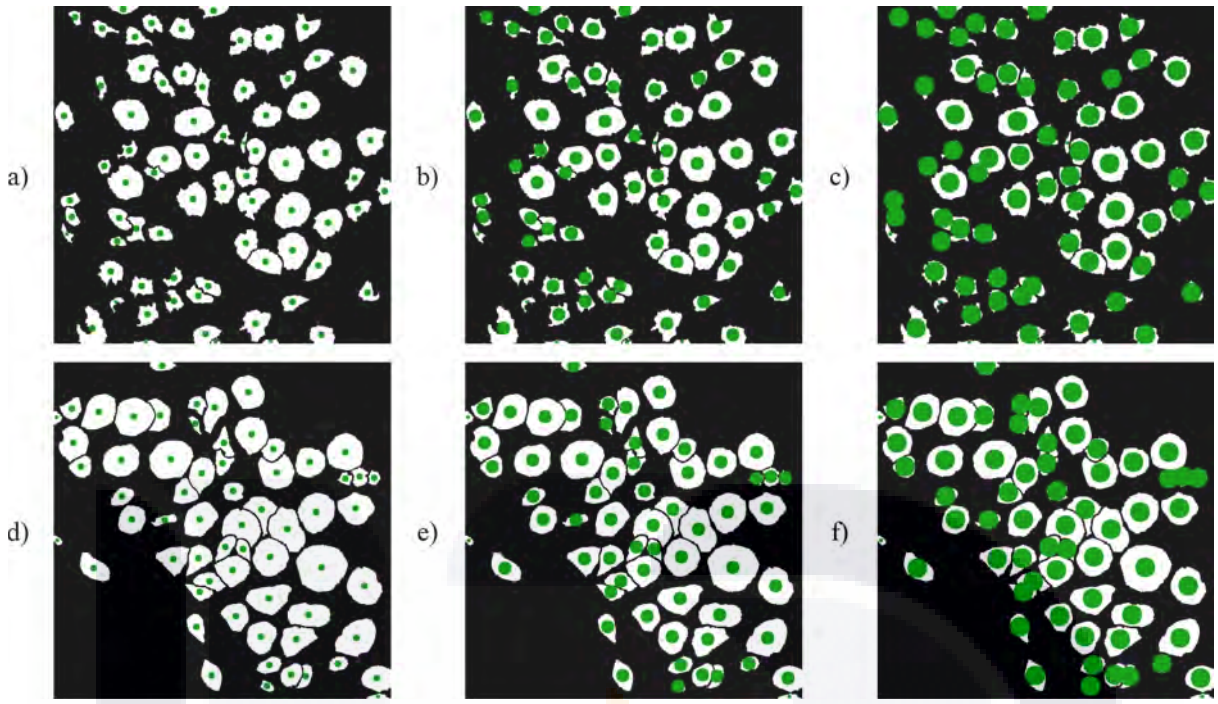

Fig. 4. Comparison of Ground Truth Enhancement process for different disk sizes using the same images of Fig. 3 b) and e). Green dots represent new ground truth, in a) and d) a disk size of 5 is used, in b) and e) a disk size of 10 and in c) and f) a disk size of 15. (For interpretation of the references to color in this figure legend, the reader is referred to the web version of this article.)

because of inaccurate cell boundaries prediction. For this reason, GTE is achieved by systematically replacing the ground truth annotation, obtained in Section 2, by a disk of smaller size, in this way, ground truth is purged from any ambiguities. GTE is performed in the following way:

For every cell body in a ground truth image, we obtain its contours, its centroid and its area. Then, if area $> A$, we set disk diameter to 5, otherwise we let diameter to 3. Finally, in the new GTE image we draw a circle of calculated diameter at the position of the centroid. In our experiments A is set to 190 pixels.

We have selected these values for the following reasons: 1) The size and shapes of cells are not uniform. Despite most of the cells are fairly round and 'big', larger than 190 pixels, there are still cells with an irregular shape and whose sizes are small either because of occlusion or because of its own nature. 2) The existence of fuzzy cell boundaries. Fuzzy cell boundaries can be the result of multiple factors such as having highly clump areas where the lighting conditions used in the microscope may make some cell borders lighter, giving the impression of two cells being visually merged into one; H-E dyes several types of cells creating different textures where the border for one cell can be similar to the body of another cell; and having sections of the images that are out of focus and make cells blurry. 3) The values mentioned here provided good results in our experiments. The rationale of using small disks sizes is to feed the DL models with the most centric part of the cell. In this way, we avoid feeding it with fuzzy regions that can be ambiguous to DL models and cause poor predictions results, that is, a DL model not being capable of separating two different cells and merging it into one, where

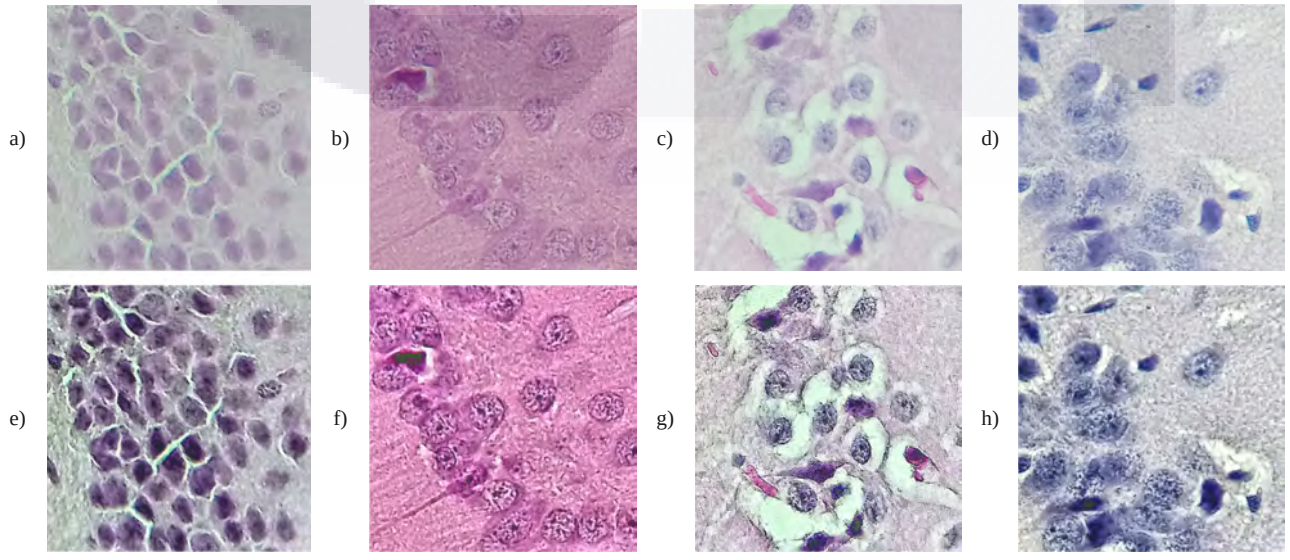

Fig. 5. Image Condition Enhancement process with different cell densities, colors, textures, and lighting conditions. Original images a-d). ICE images e-h).

Table 1
Dataset distribution.

	Training 70%	Validation 20%	Testing 10%	TOTAL
Highly dense images	116	33	17	165
Surroundings images	246	70	35	351
TOTAL	361	103	52	516

for a counting goal, this gives poor results. Thus, when cells have small bodies, less than 190, we used a disk size of 3 to prevent creating a disk that overlaps with another cell; and a disk size of 5 for the rest. In our experiments, we tested with disks sizes of 5, 10 and 15.

An example of the outcome of GTE process is shown in both Fig. 3 and Fig. 4. Fig. 4 shows a comparison of how different disk sizes keeps meaningful information and ignores fuzzy regions.

3.1.2. Image condition enhancement process

In some works (Inglis et al., 2008; Iqbal et al., 2019; Ritch et al., 2020; Soltanian-Zadeh et al., 2019; Vizcaíno, Sánchez-Cruz, Sossa, & Quintanar, 2021) image preprocessing is done by normalizing images to deal with image conditions. However, we decided to do it in a different manner. Before feeding the original image to the DL model, we do an image preprocessing step not only to address lighting conditions, but to deal with out focused images too. First, we convert the image from Red Green Blue (RGB) format to Hue Saturation Value (HSV) format to conduct a histogram equalization with Contrast-Limited Adaptive Histogram Equalization (CLAHE) (Reza, 2004) technique using a clip value of 1 and a grid size of 8 × 8 on the Value channel. Second, we do an automatic brightness adjustment process. Third, we sharpen the image. Some of these preprocessing techniques are used as well for enhancing predicting results in medical images (Kumar et al., 2020).

Automatic brightness adjustment is done by using contrast optimization with histogram clipping in the following way. First, we convert image from RGB to gray scale and calculate its histogram. Then, we calculate the cumulative distribution from the histogram. Next, we obtain the minimum and the maximum amount values to clip given a percentage parameter. Finally, we clip image by re-scaling according to the minimum and maximum values. In our experiments the clip percentage is set to 1%.

The final step, image sharpening, is implemented by doing a 2D convolution with a 3 × 3 sharpen kernel. In our experiment the sharpen kernel, k, is given by:

$$k = \begin{bmatrix} -1 & -1 & -1 \\ -1 & 9 & -1 \\ -1 & -1 & -1 \end{bmatrix}$$

An example of the outcome of ICE process is shown in Fig. 5.

3.2. Dataset construction

As mentioned in Section 2 we have 165 images of the highly dense hippocampus region DG, CA1 and CA3 and 351 images from its nearby area making a total of 516 images. To prevent images with high cell population from being unevenly distributed, we first randomly divided these 165 images into 70%, 20%, and 10% for the training, validation and testing set, respectively, and then we carried out the same procedure for the remaining 351 images. The final number of images in each set is show in Table 1.

3.3. DL model proposal

Our DL model, Cell-UNet, is based in U-Net architecture originally developed by Ronneberger et al. (2015) which has become a reference for image processing in several biomedical areas (Schlemper et al., 2019; Shuvo, Ahommed, Reza, & Hashem, 2021; Zhou, Siddiquee, Tajbakhsh, & Liang, 2020). But given the ample amount of details of very small size that are present in histological images, we modified it so that the model can be capable to 'see' them and 'learn' them. The new architecture is displayed Fig. 6.

In the encoder blocks we adjusted the 3×3 convolutions to have a padding of 1, we kept ReLU as the activation function and we replaced the max pooling operation by an adaptive max pooling operation. These changes were mainly applied to accommodate for the image size used in this work. After every encoder block, we added a sub-pixel convolution operation (Shi et al., 2016) with an upscale factor of 2 to keep and

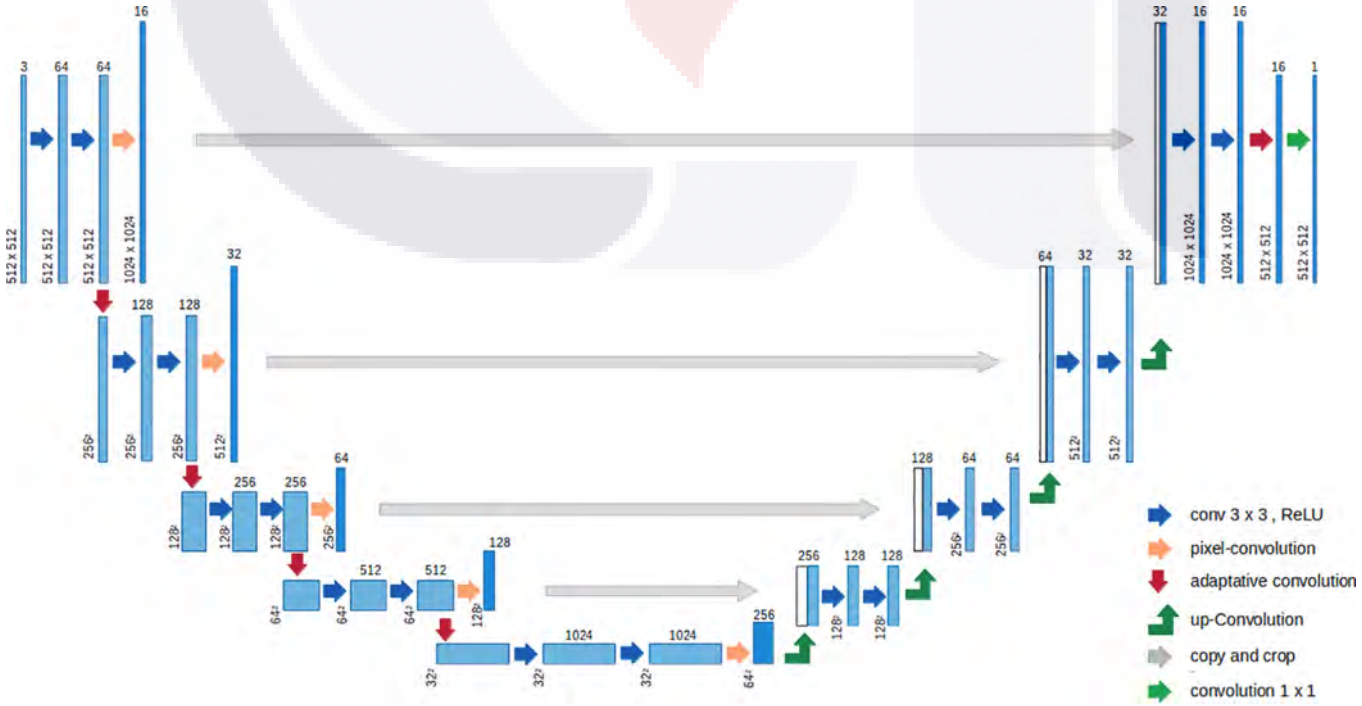

Fig. 6. Proposed Cell-UNet network architecture.

enhance the details of the channels. By doing this, we feed decoder blocks with a better pixel characterization. In a vanilla U-Net implementation, decoder blocks are fed with just the output of the encoder blocks. Finally, before the last layer of the network, another adaptive max pooling operation was added to reduce image size to match the input image size so visual inspection of the predicted cell can be easily achieved. The new model was implemented in PyTorch.

Another effect of adding adaptive max pooling and sub-pixel convolutions, besides reducing the size of decoder blocks for a factor of 4, is that the overall model size decreased, from ~31 million parameters of a baseline U-Net implementation to ~19.6 million parameters in ours. Nonetheless, its learning capabilities increased due to the better pixel characterization provided by the sub-pixel convolution operations.

4. Experiments and results

In this section we talk about how experiments were carried out. Next, we present the alternate state of the art DL models that we used to compare our model. Then, we talk about how they were trained and specify the metrics that we used to measure the performance of the model. We also discuss the approach we took to go from image segmentation paradigm to object identification paradigm. Finally, we show the results of our work and provide a comparative study using two different datasets to evaluate the generalization capabilities of the proposed methodology.

4.1. Experimental scenarios

To confirm that GTE and ICE processes contribute to models to gain better predicting performance, we formed four scenarios: 1) Unprocessed, 2) ICE, 3) GTE and 4) GTE + ICE.

In Unprocessed scenario, DL models were trained with original ground truth images obtained in Section 2 and no image preprocessing was done. In ICE scenario, nothing but image preprocessing was done to images to train DL models. Meanwhile, in GTE scenario, just ground truth enhancement process was performed. Therefore, in GTE + ICE scenario we conducted GTE and ICE processes for training DL models.

4.2. Comparison models and training information

To evaluate Cell-UNet performance against other models, we selected DL model U-Net (Ronneberger et al., 2015), U-Net++ (Zhou et al., 2020) and Attention U-Net (Schlemper et al., 2019) because they perform semantic segmentation in biomedical images and achieve state of the art results in their datasets. U-Net is a convolutional network architecture for fast and precise segmentation of images, its architecture consists of a contracting path to capture context and a symmetric expanding path that enables precise localization, these paths are commonly known as encoder-decoder blocks. U-Net++, which is based in U-Net, is essentially a deeply supervised encoder-decoder network where the encoder and decoder sub-networks are connected through a series of nested, dense skip pathways with the intention of that the redesigned skip pathways reduce the semantic gap between the feature maps of the encoder and decoder sub-networks. Attention U-Net is another DL model architecture based in U-Net that proposes the usage of attention gates in a standard CNN model with the intention to reduce false-positive predictions for small objects that show large shape variability, filters the features propagated through the skip connections and suppresses feature responses in irrelevant background regions.

All these models were trained using Training dataset. Regardless of the experimental scenario, image augmentation was employed to increase Training dataset with random operations such as vertical flip, horizontal flip, image transpose, image rotation (maximum rotation of ±270°), image scaling (scale limit of ±2%), image shifting (shift limit of ±1%), brightness adjustment (limit of ±12%), contrast adjustment (limit of ±12%), hue-saturation-value adjustment (limit of ±20 for all channels) and a resize operation (size of 512 × 512 and linear interpolation) to prevent feeding the models with an incorrect image size. To artificially increase the size of Training dataset, we set the number of steps per epoch to *train dataset size* × *n*. In our experiments, *n*, was set to 8. This decision was based in the number of random operations in the image augmentation process, in the range values that can be applied to them, verifying when models stopped learning and avoiding any overfitting situation.

Because pixel information belonging to cells is highly skewed in most images of the dataset, focal Tversky loss function (Abraham & Khan, 2019), which is a generalization from a dice loss function, was chosen for its capability to address imbalanced datasets in medical image segmentation tasks. In our experiments the α and β parameters were set to 0.75.

We used Adam optimizer with a learning rate of $1.5^{-4}/\sqrt{(5)}$ and a weight_decay of 2^{-5}. The best performing model, for each of the discussed DL models, were picked and judged under the Validation dataset.

All models were trained using a GTX 1080 Ti GPU and given the computational restrictions a training batch size of 2, 3, 4 and 4 was used for UNet++, Attention U-Net, U-Net and Cell-UNet, respectively. The operating system is Ubuntu 20.04 with an AMD Ryzen 9 3900X CPU and 32 GB in RAM.

Table 2
Model performance in unprocessed scenario. Bold numbers show the best metric/model.

Metric \ Model	U-Net	Attention U-Net	UNet++	Cell-UNet
Accuracy	0.6332	0.6032	0.6479	**0.6680**
Precision	0.8454	0.8153	**0.8920**	0.8636
Recall	0.7162	0.6987	0.7031	**0.7467**
F_1 score	0.7754	0.7525	0.7863	**0.8009**

4.3. Evaluation metrics

Since the output of the DL models is an image, to go from a semantic segmentation prediction to an object (cell) identification paradigm that facilitates a counting strategy, the following process is done: 1) With the ground truth image, we extracted the bounding boxes for each manually segmented cell, 2) With the predicted image, we performed a connected component analysis and obtained all the blobs, which is easy to see that they correspond to cell predictions, 3) We matched the predicted cells against the collected bounding boxes by checking if the centroid of cell fell inside of a bounding box that was not matched already; when this was the case, this cell was counted as a True Positive (TP), otherwise it was counted as a False Positive (FP), and 4) All unmatched bounding boxes were counted as False Negatives (FN).

With the above discrimination criteria in mind and making use of the Testing dataset, we compared the models against each other and measured their performance under different metrics such as Accuracy, Precision, Recall and F_1 score. These metrics are defined by:

$$Accuracy = \frac{TP + TN}{TP + TN + FP + FN},$$

$$Precision = \frac{TP}{TP + FP},$$

Table 3
Model performance in ICE scenario.

Metric \ Model	U-Net	Attention U-Net	UNet++	Cell-UNet
Accuracy	0.6277	0.6361	0.6222	**0.6506**
Precision	0.8143	0.8356	**0.8688**	0.8281
Recall	0.7325	0.7271	0.6867	**0.7522**
F_1 score	0.7713	0.7776	0.7671	**0.7883**

Table 4
Model performance in GTE scenario.

Metric \ Model	U-Net	Attention U-Net	UNet++	Cell-UNet
Accuracy	0.8116	0.8068	0.7802	**0.8094**
Precision	0.9235	**0.9376**	0.9248	0.9243
Recall	0.8701	0.8526	0.8330	**0.8668**
F_1 score	0.8960	0.8931	0.8765	**0.8946**

Table 5
Model performance in GTE + ICE scenario.

Metric \ Model	U-Net	Attention U-Net	UNet++	Cell-UNet
Accuracy	0.8090	0.8136	0.8062	**0.8160**
Precision	0.9059	0.9083	**0.9407**	0.9170
Recall	0.8832	**0.8865**	0.8493	0.8810
F_1 score	0.8944	0.8972	0.8927	**0.8987**

$$Recall = \frac{TP}{TP + FN},$$

$$F_1 score = 2 \times \left(\frac{Precision \times Recall}{Precision + Recall}\right).$$

4.4. Results

We computed these metrics for all different experimental scenarios stated before. The results for Unprocessed, ICE, GTE and GTE + ICE scenarios are shown in Table 2, Table 3, Table 4 and Table 5, respectively.

In Fig. 7, we show how models output segmentation prediction for an image with a highly dense cell population and fuzzy boundaries, under Unprocessed and GTE + ICE scenarios. In Fig. 8 we provide a comparative result between proposed scenarios and the effects of using different disk sizes and in Fig. 9, we have an image of a region of interest, its correspondent Ground Truth image and the segmentation prediction produced by our model under Unprocessed scenario suggesting that poor performance might not be associated to the number of cells but to cell boundary conditions. Finally, the mapping process that takes an image segmentation result to an object identification result, is shown in Fig. 10, where we present all scenarios and DL models we covered in this work.

Apart from models predictions and performance metrics, in Table 6, we provide model sizes in terms of number of parameters and their average training time.

Training time was measured from the start of epoch one until epoch ten, considering the preprocessing steps as part of the training process.

4.5. Results in other datasets

Here, we present the results of using the methodology described before, applied to two public domain image databases to evaluate its generalization capability.

The first dataset (Naylor, Laé, Reyal, & Walter, 2019) contains nuclei segmentation for breast cancer patients and it is constituted of 50 H-E stained images of a size of 512 × 512 scanned at 40x. The heterogeneity of the image data, include low and high cellularity areas regions which can be stromal areas or adipose tissue, but also of invasive breast carcinoma cells, respectively. Cell annotations include normal epithelial and myoepithelial breast cells, fibroblasts, endothelial cells, carcinomatous cells, macrophages, adipocytes and inflammatory cells. Information regarding ground truth acquisition, number of patients and the image provider institute is available on (Naylor et al., 2019). Fig. 11 presents the results obtained with our proposal and Fig. 12 shows prediction results on two randomly selected test images.

The second dataset (Kumar et al., 2017) comprises 37 H-E images scanned at 40×, each of size 1000 × 1000 of hand-annotated nuclear boundaries, and additional 18 H-E tissues images that were used for testing. The dataset is constituted of 7 different organs namely, liver, colon, kidney, stomach, bladder, prostate, and breast, that contains benign and diseased tissue samples. The ground truth acquisition technique, patients, and hospital information where the samples were obtained are available on (Kumar et al., 2017; Kumar et al., 2020). This dataset provides the ground truth annotation in xml format, where it is common to find the boundary of a nuclei overlapping or touching other

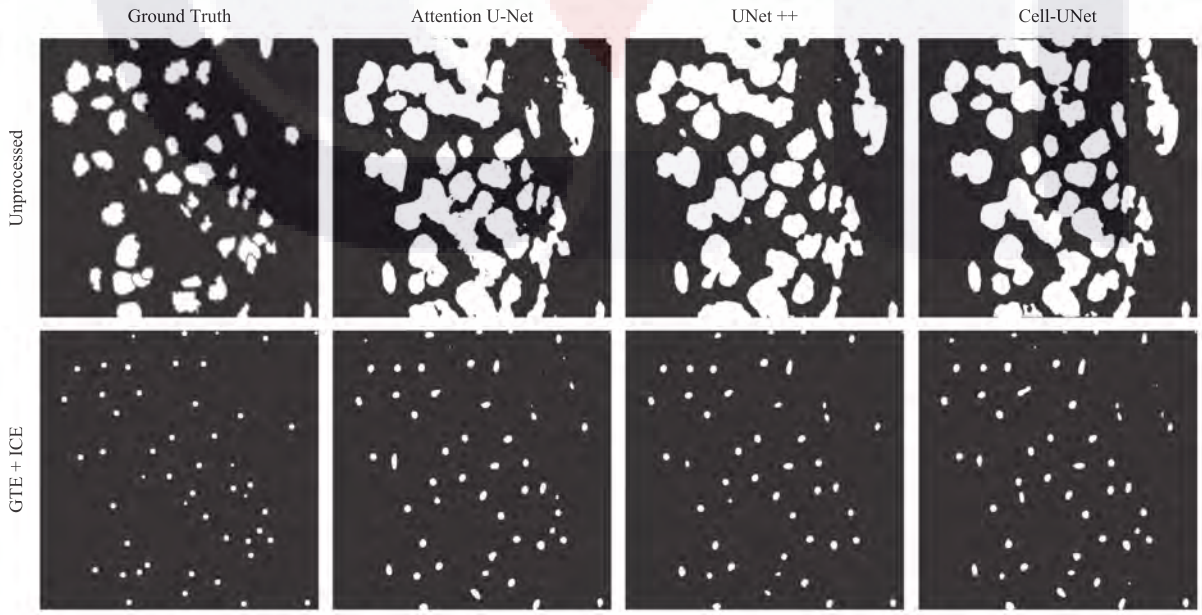

Fig. 7. Image from a DG region showing predictions per model under two scenarios. Rows correspond to different experimental scenarios. The first column corresponds to the ground truth and the rest of the columns correspond to DL models predictions.

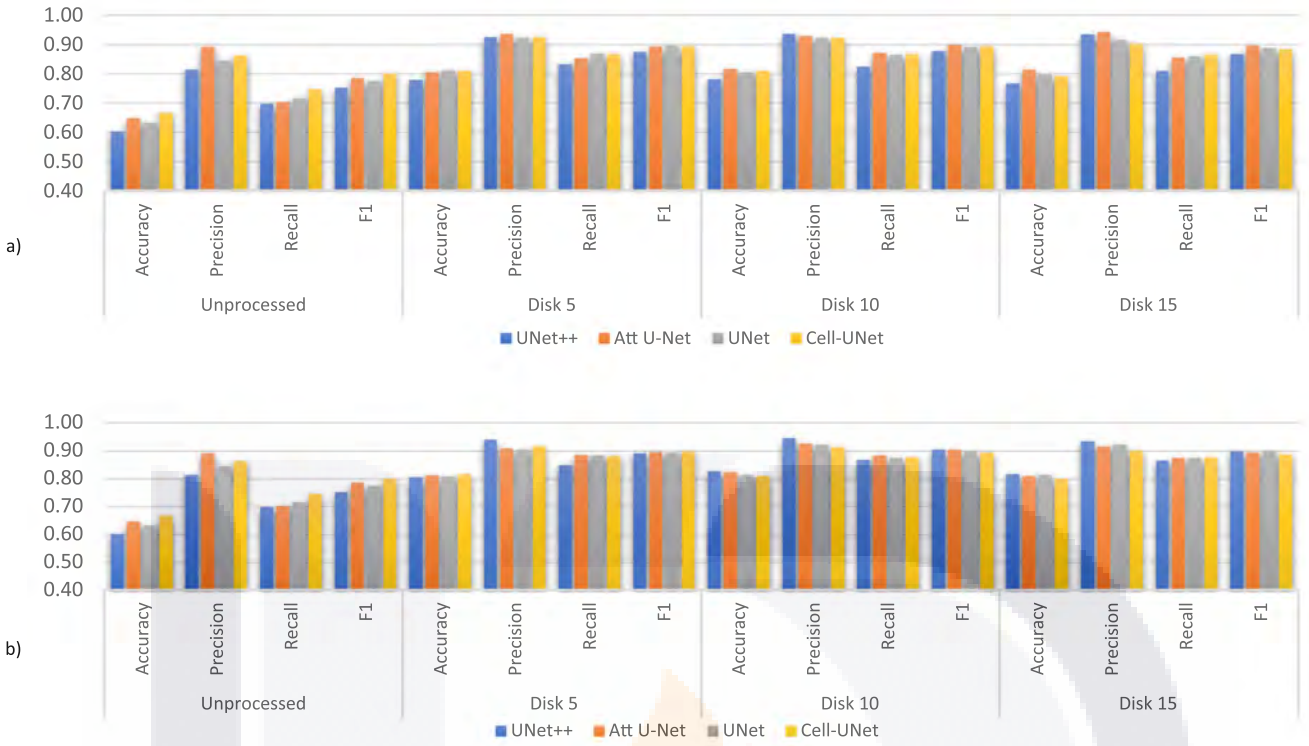

Fig. 8. Effects of tunning parameters in metrics performance when GTE is performed. a) Scenarios: Unprocessed vs GTE using disk sizes of 5, 10 and 15. b) Scenarios: Unprocessed vs GTE + ICE using disk sizes of 5, 10 and 15.

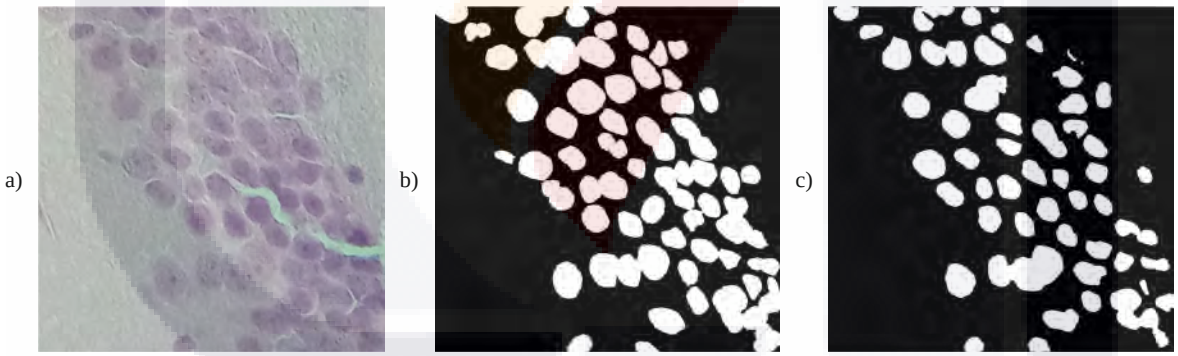

Fig. 9. a) Image from a CA1 region. b) Ground Truth Image. c) Cell-Net segmentation prediction.

nuclei, thus, causing those two different nuclei to be treated as one object and creating a problem to evaluate the counting goal intended in this work. For this reason, it was not possible to create a ground truth image where all cells are clearly separated and only GTE + ICE scenario was evaluated calculating the bounding boxes, in a similar way as described in section 4.2, of the annotated boundaries contained in the xml file. Figs. 13 and 14 show the results obtained by DL models with this dataset and the prediction results of two sample images obtained by Cell-UNet.

5. Discussion

As it can be seen from Table 2 and Table 3, in Unprocessed and ICE scenario, respectively, our proposed model outperformed all models in Accuracy, Recall and F_1 score, yet UNet++ obtained a better Precision value. However, when observing the metrics obtained in ICE only scenario against Unprocessed scenario, we can see a mix of better and worse metrics than in Unprocessed scenario, suggesting that ICE processing alone does not contribute to a consistent performance gain as a consequence of having very fuzzy cell boundaries.

For GTE scenario, Table 4, our proposed model outperformed again all models in Accuracy, Recall and F_1 score but in Precision metric, Attention U-Net achieved the highest value. Furthermore, all models show a mean performance increase of 12.2% in all metrics. This information is presented in Table 7. This suggests that GTE does bring models to a higher performance predictability, and confirming that when reducing noisy cell boundaries, models can distinguish cells in a more concordant way.

In GTE + ICE scenario, Table 5, all metrics have their highest values when compared to all previous scenarios. In this regard, UNet++ obtained the highest value for Precision metric (0.9407) and Attention U-Net for Recall (0.8865). Our model accomplished the highest values in Accuracy (0.8160) and F_1 score (0.8987). Moreover, when comparing the performance of the models in this scenario against the performance

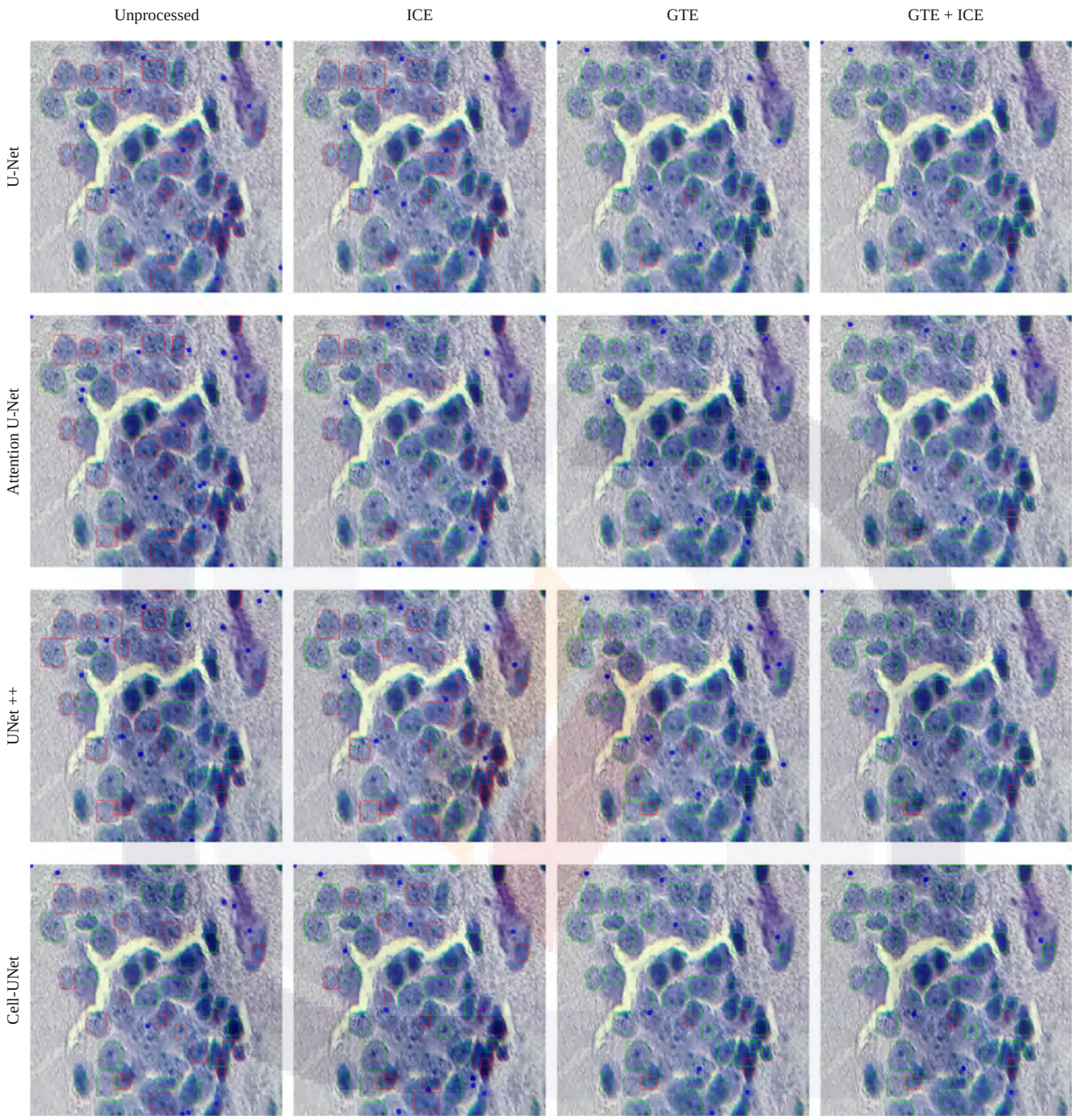

Fig. 10. Image from a DG region (its ground truth image is displayed in Fig. 7) showing predictions per model and scenario. Columns correspond to experimental scenarios. Rows correspond to DL models predictions. Green boxes indicate cells that were correctly identified (TP). Red boxes signal cells that were not found by the DL models (FN). Blue dots stand for incorrectly predicted cells (FP).

Table 6
Model size and training time.

Metric \ Model	U-Net	Attention U-Net	UNet++	Cell-UNet
Number of parameters (millions)	31	34.8	36.6	**19.6**
Avg. training time (hours)	1:18	1:53	3:55	**1:02**

obtained by the models in Unprocessed scenario, we can see that all models experienced a mean performance increase of 12.82% in all metrics. This information can be seen in Table 8. This indicates that when reducing noisy cell boundaries and enhancing the image condition, the model performance increases in a consistent and significant way.

Likewise, in Figs. 8 and 10, we can observe that all DL models increase their predicting capabilities when noise reduction is conducted by the effect of removing the fuzziness in cell boundaries and enhancing image condition which means that it is not associated to a particular DL model only. This situation explains the concordant performance increase across all models, and which is shown in the values expressed in Tables 2–5. Also, Fig. 8 shows that best results can be obtained when using a disk size of 5 or 10, and the difference between their results

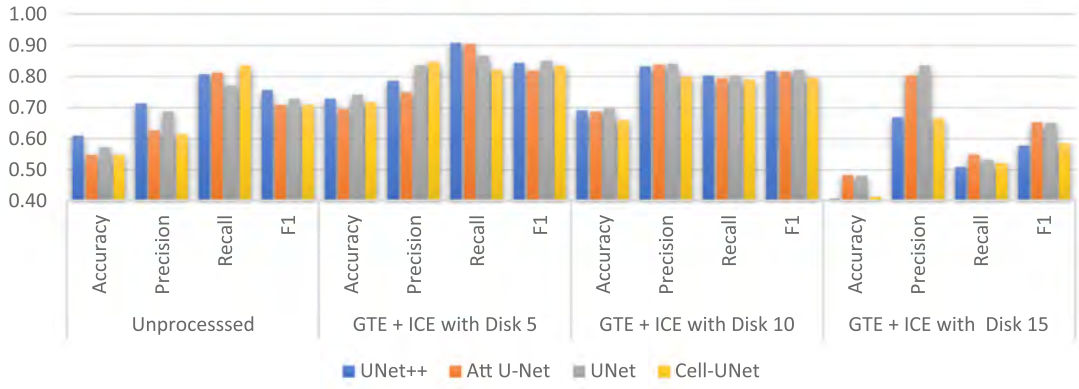

Fig. 11. Results and effects of tunning parameters in metrics performance when Unprocessed images and GTE + ICE is performed. For Nuclei segmentation based on breast cancer H-E images in a 40x magnification and using and disk sizes of 5, 10 and 15.

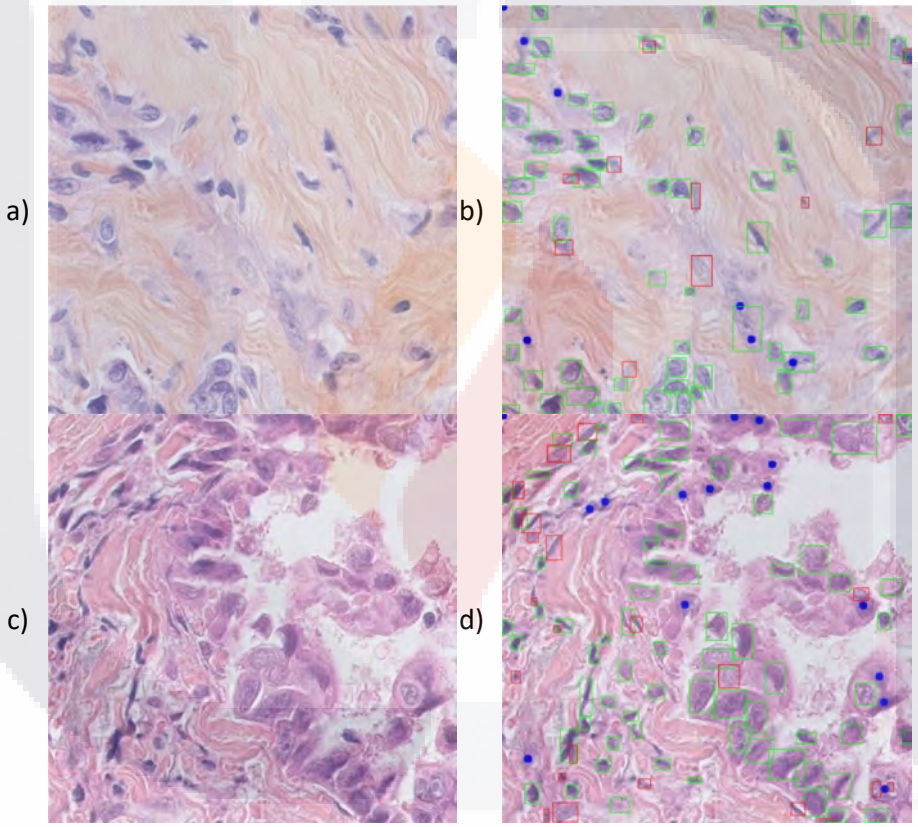

Fig. 12. Prediction results with Naylor et al (2019) dataset using GTE + ICE scenario and a disk size of 5. a) and c) original images. b) and d) Cell-UNet predictions. Green boxes indicate cells that were correctly identified (TP). Red boxes signal cells that were not found by the DL model (FN). Blue dots stand for incorrectly predicted cells (FP). (For interpretation of the references to color in this figure legend, the reader is referred to the web version of this article.)

might be associated to size of the cells contained in the images.

When analyzing the results of our work applied to other datasets, we can see from Fig. 11 and Fig. 13 that its generalizing capabilities stand across different type of images, achieving 0.7170, 0.8486, 0.8222, 0.8352 in Accuracy, Precision, Recall and F_1, respectively, in Naylor et al (2019) dataset and with Kumar et al (2017). We obtained 0.7846, 0.8784, 0.8802, and 0.8793 for Accuracy, Precision, Recall and F_1, respectively, despite the different sizes and nature of images. Unfortunately, a direct comparison with their works cannot be established since they use metrics for image segmentation and not cell counting.

Having verified that GTE + ICE scenario contributes to a higher performance predictability, we can examine the results obtained here and say that for a given experiment, if it were preferable to correctly find most of the cells in an image, that is, to have a few amount FN, at the expense of having a higher amount of incorrectly predicted cells, meaning, having a higher amount FP, then, the model with the highest Recall metric should be picked, in this case Attention U-Net. Likewise, if it were preferable to have fewer incorrectly predicted cells, having a fewer amount FP, at the expense of not finding all the cells in an image, having a higher amount FN, then, the model with the highest Precision metric should be selected, in this case UNet++. Nonetheless, when it is needed an equilibrium between correctly finding most of the cells in an image, having as few FN as possible, and having the fewest possible amount of incorrectly predicted cells, having as few FP as possible, the

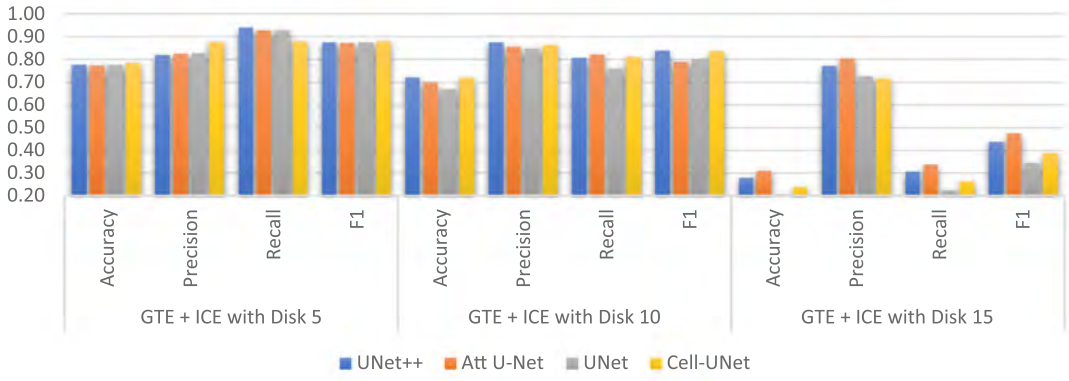

Fig. 13. Results and effects of tunning parameters in metrics performance when GTE + ICE is performed on different H-E images with a 40x magnification and using disk sizes of 5, 10 and 15.

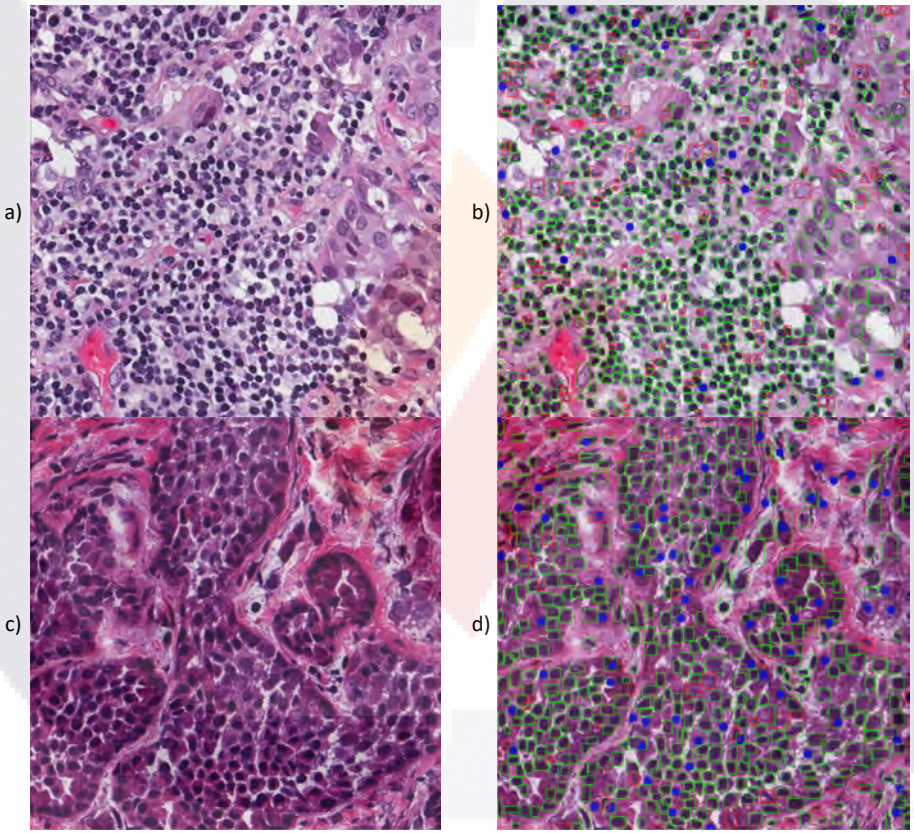

Fig. 14. Prediction results with Kumar et. al (2017) dataset using GTE + ICE scenario and a disk size of 5. a) and c) original images. b) and d) Cell-UNet predictions. Green boxes indicate cells that were correctly identified (TP). Red boxes signal cells that were not found (FN). Blue dots stand for incorrectly predicted cells (FP). (For interpretation of the references to color in this figure legend, the reader is referred to the web version of this article.)

Table 7
Performance gain – Unprocessed vs GTE scenario.

Metric \ Model	U-Net	Attention U-Net	UNet++	Cell-UNet
Accuracy	17.84%	20.36%	13.23%	14.14%
Precision	7.81%	12.23%	3.28%	6.07%
Recall	15.39%	15.39%	12.99%	12.01%
F_1 score	12.06%	14.06%	9.02%	9.37%
Avg. Increase	13.28%	15.51%	9.63%	10.40%
Mean Increase		12.2%		

Table 8
Performance gain – Unprocessed vs GTE + ICE scenario.

Metric \ Model	U-Net	Attention U-Net	UNet++	Cell-UNet
Accuracy	17.58%	21.04%	15.83%	14.80%
Precision	6.05%	9.30%	4.87%	5.34%
Recall	16.70%	18.78%	14.62%	13.43%
F_1 score	11.90%	14.47%	10.64%	9.78%
Avg. increase	13.06%	15.90%	11.49%	10.84%
Mean increase	12.82%			

best alternative to choose is our proposed model, since F1 score metric is the harmonic mean of Precision and Recall, which weights a balance between FP and FN.

Not only our proposed model performs in a remarkable way due to the better pixel characterization, but we can also see from Table 6 that it produced a more efficient model size since it is ~1.58 times smaller than U-Net and ~1.77 and ~1.86 times smaller than Attention U-Net and UNet++, respectively, making it specially suitable for hardware/resource constrained devices. Another side effect of reducing the model size can be seen in the positive impact given in the training time, as it takes ~3 h less when compared to its counterpart UNet++ or ~1 h less compared to Attention U-Net.

The histological analysis is very extensive, not only because of the involved techniques in creating the samples but also because of the staining used to mark the intended cell bodies which results in a vast variability of color in cell staining and in tissue texture, therefore a fair comparison between different techniques and antibodies would not be fair. However, we list the results obtained by different authors when performing cell counting task with the intention to create an awareness of the good results obtained in the context of this work. Iqbal et al. (2019) achieved a mean average-precision score of 0.75 and a mean precision of 0.87 in highly dense cell population of fluorescently-tagged images. Štajduhar et al. (2019) correctly distinguished 95.41% of neurons in NeuN-stained images of adult human prefrontal cortex images. Soltanian-Zadeh et al. (2019) reached scores of 0.86, 0.88, 0.87 for recall, precision and F1 metrics, respectively, in two-photon calcium images and Inglis et al. (2008) correctly identified 86 ± 5% neurons with 15 ± 8% error (mean ± standard deviation) in Nissl-stained images.

6. Conclusions

We proved that DL model performance can be leveraged by doing a Ground Truth Enhancement process and that the proposed architecture, despite its smaller size, is capable of achieving state of the art results in the highly dense sections CA1, CA3, and DG of hippocampus rat images, because of added layer which contains a better pixel characterization information.

We also proved that the present work yields remarkable and consistent counting results in H-E stained images with respect to its ground of truth reference, among different groups of rats. Thus, making its use feasible and reliable even in those images originated from rats that received a treatment after an ischemic procedure was applied to them.

With the foregoing, this work can help to reliably facilitate and automate the counting process when the cell concentration is either high or low, even in those images that do not have the most optimal conditions for their usage.

When compared with other DL models Cell-UNet achieves its best performance when using a disk size of 5, however, when using larger disk sizes, other models could have better results given the higher number of parameters that other models have. Additionally, to make use of the ground truth enhancement process, currently, a full manual segmentation on cells is needed. Nevertheless, as per the experiments presented in this work, a good research direction can be considered with the purpose of alleviating the time-consuming task for manually annotating images by just creating the manual ground truth annotation on cells with a small disk size and verify if good predicting results are still observed.

Likewise, one direction for future research could be on the generation of a DL model where the pixel characterization layer could be added to the DL models presented here or a YOLO based model. Also, handling a different image size can be an interesting experiment to evaluate when using an upscale image size which, in turn, could help DL models to better learn blurry regions. Another aspect that could be considered for future work is in the creation of a process that can automatically extract all the images contained in a big sample image and automate the counting process for the whole batch.

7. Funding statement

This work is funded in part by Universidad Autónoma de Aguascalientes under grant PII22-5.

CRediT authorship contribution statement

Alfonso Vizcaíno: Conceptualization, Software, Investigation, Writing – original draft, Methodology. **Hermilo Sánchez-Cruz:** Conceptualization, Writing – review & editing, Project administration, Supervision, Funding acquisition. **Humberto Sossa:** Conceptualization, Validation, Writing – review & editing, Methodology, Funding acquisition. **J. Luis Quintanar:** Conceptualization, Resources, Data curation, Methodology, Validation.

Declaration of Competing Interest

The authors declare that they have no known competing financial interests or personal relationships that could have appeared to influence the work reported in this paper.

Data availability

Data will be made available on request.

Acknowledgments

Hermilo Sánchez-Cruz thanks Universidad Autónoma de Aguascalientes support, under grant PII22-5. Humberto Sossa thanks the Instituto Politécnico Nacional under grants SIP 20210788 and SIP 20220226, and CONACYT under grant FORDECYT-PRONACES: CF-CD24-20200211185113358-6005. Alfonso Vizcaíno thanks CONACYT for the scholarship granted to pursue his doctoral studies. We also recognize Karina Alejandra Pedroza García for her scientific discussions.

References

Abraham, N., & Khan, N. M. (2019). A novel focal Tversky loss function with improved attention U-Net for lesion segmentation. *2019 IEEE 16th International Symposium on Biomedical Imaging (ISBI 2019)*, 683–687. https://doi.org/10.1109/ISBI.2019.8759329.

Ali, F., El-Sappagh, S., Islam, S. M. R., Kwak, D., Ali, A., Imran, M., & Kwak, K.-S. (2020). A smart healthcare monitoring system for heart disease prediction based on ensemble deep learning and feature fusion. *Information Fusion, 63*, 208–222. https://doi.org/10.1016/j.inffus.2020.06.008.

Attili, S. M., Silva, M. F. M., Nguyen, T., & Ascoli, G. A. (2019). Cell numbers, distribution, shape, and regional variation throughout the murine hippocampal formation from the adult brain Allen Reference Atlas. *Brain Structure and Function, 224*(8), 2883–2897. https://doi.org/10.1007/s00429-019-01940-7

Chai, Y., Liu, H., & Xu, J. (2018). Glaucoma diagnosis based on both hidden features and domain knowledge through deep learning models. *Knowledge-Based Systems, 161*, 147–156. https://doi.org/10.1016/j.knosys.2018.07.043.

Chen, H., Dou, Q., Yu, L., Qin, J., & Heng, P.-A. (2018). VoxResNet: Deep voxelwise residual networks for brain segmentation from 3D MR images. *NeuroImage, 170*, 446–455. https://doi.org/10.1016/j.neuroimage.2017.04.041.

Chowdhury, A. B., Roberson, J., Hukkoo, A., Bodapati, S., & Cappelleri, D. J. (2020). Automated complete blood cell count and malaria pathogen detection using convolution neural network. *IEEE Robotics and Automation Letters, 5*(2), 1047–1054. https://doi.org/10.1109/LRA.2020.2967290

Cireşan, D. C., Giusti, A., Gambardella, L. M., & Schmidhuber, J. (2013). Mitosis detection in breast cancer histology images with deep neural networks. In K. Mori, I. Sakuma, Y. Sato, C. Barillot, & N. Navab (Eds.), *Medical image computing and computer-assisted intervention – MICCAI 2013* (pp. 411–418). Berlin, Heidelberg: Springer, Berlin Heidelberg.

Dorph-Petersen, K.-A., Nyengaard, J. R., & Gundersen, H. J. G. (2001). Tissue shrinkage and unbiased stereological estimation of particle number and size*. *Journal of Microscopy, 204*(3), 232–246. https://doi.org/10.1046/j.1365-2818.2001.00958.x.

Duregon, E., Molinaro, L., Volante, M., Ventura, L., Righi, L., Bolla, S., … Papotti, M. G. (2014). Comparative diagnostic and prognostic performances of the hematoxylin-eosin and phospho-histone H3 mitotic count and Ki-67 index in adrenocortical

carcinoma. *Modern Pathology, 27*(9), 1246–1254. https://doi.org/10.1038/modpathol.2013.230

García, M. D. R. M., & Quintanar, J. L. (2020). Acute cerebral ischemia-reperfusion model by endovascular occlusion of the middle cerebral artery in the rat-technical improvements. *Biomedical Journal of Scientific & Technical Research, 32*(2), 24907–24911.

Gibson, E., Giganti, F., Hu, Y., Bonmati, E., Bandula, S., Gurusamy, K., … Barratt, D. C. (2018). Automatic multi-organ segmentation on abdominal CT with dense V-networks. *IEEE Transactions on Medical Imaging, 37*(8), 1822–1834. https://doi.org/10.1109/TMI.2018.2806309

Giguère, N., Burke Nanni, S., & Trudeau, L.-E. (2018). On cell loss and selective vulnerability of neuronal populations in parkinson's disease. *Frontiers in Neurology, 9*, 455. https://doi.org/10.3389/fneur.2018.00455

Hagos, Y. B., Narayanan, P. L., Akarca, A. U., Marafioti, T., & Yuan, Y. (2019). ConCORDe-Net: Cell count regularized convolutional neural network for cell detection in multiplex immunohistochemistry images. In D. Shen, T. Liu, T. M. Peters, L. H. Staib, C. Essert, S. Zhou, … A. Khan (Eds.), *Medical image computing and computer assisted intervention – MICCAI 2019* (pp. 667–675). Cham: Springer International Publishing.

Hamed, G., Marey, M. A. E. R., Amin, S. E. S., & Tolba, M. F. (2020). Deep Learning in Breast Cancer Detection and Classification. *Advances in Intelligent Systems and Computing, 1153 AISC*, 322–333. Springer. https://doi.org/10.1007/978-3-030-44289-7_30.

Inglis, A., Cruz, L., Roe, D. L., Stanley, H. E., Rosene, D. L., & Urbanc, B. (2008). Automated identification of neurons and their locations. *Journal of Microscopy, 230*(3), 339–352. https://doi.org/10.1111/j.1365-2818.2008.01992.x.

Iqbal, A., Sheikh, A., & Karayannis, T. (2019). DeNeRD: High-throughput detection of neurons for brain-wide analysis with deep learning. *Scientific Reports, 9*(1), 13828. https://doi.org/10.1038/s41598-019-50137-9

Jiang, Z., Liu, X., Yan, Z., Gu, W., & Jiang, J. (2021). Improved detection performance in blood cell count by an attention-guided deep learning method. *OSA Continuum, 4*(2), 323–333. https://doi.org/10.1364/OSAC.413787

Ke, H., Liu, D., Li, T., Chu, X., Xin, D., Han, M., … Wang, Z. (2020). Hydrogen-rich saline regulates microglial phagocytosis and restores behavioral deficits following hypoxia-ischemia injury in neonatal mice via the Akt pathway. *Drug Design, Development and Therapy, 14*, 3827.

Komur, M., Okuyaz, C., Celik, Y., Resitoglu, B., Polat, A., Balci, S., … Beydagi, H. (2014). Neuroprotective effect of levetiracetam on hypoxic ischemic brain injury in neonatal rats. *Child's Nervous System, 30*(6), 1001–1009. https://doi.org/10.1007/s00381-014-2375-x

Kumar, N., Verma, R., Sharma, S., Bhargava, S., Vahadane, A., & Sethi, A. (2017). A dataset and a technique for generalized nuclear segmentation for computational pathology. *IEEE Transactions on Medical Imaging, 36*(7), 1550–1560. https://doi.org/10.1109/TMI.2017.2677499

Kumar, N., Verma, R., Anand, D., Zhou, Y., Onder, O. F., Tsougenis, E., … Sethi, A. (2020). A multi-organ nucleus segmentation challenge. *IEEE Transactions on Medical Imaging, 39*(5), 1380–1391. https://doi.org/10.1109/TMI.2019.2947628

Kwon, J., Kim, K.-H., Jeon, K.-H., Kim, H. M., Kim, M. J., Lim, S.-M., … Oh, B.-H. (2019). Development and validation of deep-learning algorithm for electrocardiography-based heart failure identification.. Retrieved from *Korean Circulation Journal, 49*(7), 629–639.

Li, W., Fotinos, A., Wu, Q., Chen, Y., Zhu, Y., Baranov, S., … Wang, X. (2015). N-acetyl-l-tryptophan delays disease onset and extends survival in an amyotrophic lateral sclerosis transgenic mouse model. *Neurobiology of Disease, 80*, 93–103. https://doi.org/10.1016/j.nbd.2015.05.002.

Li, Y., Mahjoubfar, A., Chen, C. L., Niazi, K. R., Pei, L., & Jalali, B. (2019). Deep cytometry: Deep learning with real-time inference in cell sorting and flow cytometry. *Scientific Reports, 9*(1), 11088. https://doi.org/10.1038/s41598-019-47193-6

Mattson, M. P. (2000). Apoptosis in neurodegenerative disorders. *Nature Reviews Molecular Cell Biology, 1*(2), 120–130. https://doi.org/10.1038/35040009

Naylor, P., Laé, M., Reyal, F., & Walter, T. (2019). Segmentation of nuclei in histopathology images by deep regression of the distance map. *IEEE Transactions on Medical Imaging, 38*(2), 448–459. https://doi.org/10.1109/TMI.2018.2865709

Nuovo, G. J., Magro, C., Shaffer, T., Awad, H., Suster, D., Mikhail, S., … Tili, E. (2021). Endothelial cell damage is the central part of COVID-19 and a mouse model induced by injection of the S1 subunit of the spike protein. *Annals of Diagnostic Pathology, 51*, Article 151682. https://doi.org/10.1016/j.anndiagpath.2020.151682.

Ochi, S., Abe, M., Li, C., Mori, Y., Ishimaru, T., Yoshino, Y., … Ueno, S. (2014). The nicotinic cholinergic system is affected in rats with delayed carbon monoxide encephalopathy. *Neuroscience Letters, 569*, 33–37. https://doi.org/10.1016/j.neulet.2014.03.054.

Potes, C., Parvaneh, S., Rahman, A., & Conroy, B. (2016). Ensemble of feature-based and deep learning-based classifiers for detection of abnormal heart sounds. *Computing in Cardiology Conference (CinC), 2016*, 621–624.

Procaccini, C., Santopaolo, M., Faicchia, D., Colamatteo, A., Formisano, L., de Candia, P., … Matarese, G. (2016). Role of metabolism in neurodegenerative disorders. *Metabolism, 65*(9), 1376–1390. https://doi.org/10.1016/j.metabol.2016.05.018.

Radovsky, A., Katz, L., Ebmeyer, U., & Safar, P. (1997). Ischemic neurons in rat brains after 6, 8, or 10 minutes of transient hypoxic ischemia. *Toxicologic Pathology, 25*(5), 500–505. https://doi.org/10.1177/019262339702500512

Ravì, D., Wong, C., Deligianni, F., Berthelot, M., Andreu-Perez, J., Lo, B., & Yang, G.-Z. (2017). Deep learning for health informatics. *IEEE Journal of Biomedical and Health Informatics, 21*(1), 4–21. https://doi.org/10.1109/JBHI.2016.2636665

Redmon, J., Divvala, S., Girshick, R., & Farhadi, A. (2016). You only look once: Unified, real-time object detection. *IEEE Conference on Computer Vision and Pattern Recognition (CVPR), 2016*, 779–788. https://doi.org/10.1109/CVPR.2016.91

Ren, S., He, K., Girshick, R., & Sun, J. (2017). Faster R-CNN: Towards real-time object detection with region proposal networks. *IEEE Transactions on Pattern Analysis and Machine Intelligence, 39*(6), 1137–1149. https://doi.org/10.1109/TPAMI.2016.2577031

Reza, A. M. (2004). Realization of the contrast limited adaptive histogram equalization (CLAHE) for real-time image enhancement. *Journal of VLSI Signal Processing Systems for Signal, Image and Video Technology, 38*(1), 35–44. https://doi.org/10.1023/B:VLSI.0000028532.53893.82

Ritch, M. D., Hannon, B. G., Read, A. T., Feola, A. J., Cull, G. A., Reynaud, J., … Ethier, C. R. (2020). AxoNet: A deep learning-based tool to count retinal ganglion cell axons. *Scientific Reports, 10*(1), 8034. https://doi.org/10.1038/s41598-020-64898-1

Ronneberger, O., Fischer, P., & Brox, T. (2015). U-Net: Convolutional networks for biomedical image segmentation. In N. Navab, J. Hornegger, W. M. Wells, & A. F. Frangi (Eds.), *Medical Image Computing and Computer-Assisted Intervention – MICCAI 2015* (pp. 234–241). Cham: Springer International Publishing.

Roy Sarkar, S., & Banerjee, S. (2019). Gut microbiota in neurodegenerative disorders. *Journal of Neuroimmunology, 328*, 98–104. https://doi.org/10.1016/j.jneuroim.2019.01.004

Schlemper, J., Oktay, O., Schaap, M., Heinrich, M., Kainz, B., Glocker, B., & Rueckert, D. (2019). Attention gated networks: Learning to leverage salient regions in medical images. *Medical Image Analysis, 53*, 197–207. https://doi.org/10.1016/j.media.2019.01.012.

Schuhmann, M. K., Gunreben, I., Kleinschnitz, C., & Kraft, P. (2016). Immunohistochemical analysis of cerebral thrombi retrieved by mechanical thrombectomy from patients with acute ischemic stroke. *International Journal of Molecular Sciences, 17*(3). https://doi.org/10.3390/ijms17030298

Serte, S., & Serener, A. (2019). A generalized deep learning model for glaucoma detection. In *2019 3rd International Symposium on Multidisciplinary Studies and Innovative Technologies (ISMSIT)* (pp. 1–5). https://doi.org/10.1109/ISMSIT.2019.8932753

Serte, S., & Demirel, H. (2021). Deep learning for diagnosis of COVID-19 using 3D CT scans. *Computers in Biology and Medicine, 132*, Article 104306. https://doi.org/10.1016/j.compbiomed.2021.104306.

Shen, L., Margolies, L. R., Rothstein, J. H., Fluder, E., McBride, R., & Sieh, W. (2019). Deep learning to improve breast cancer detection on screening mammography. *Scientific Reports, 9*(1), 12495. https://doi.org/10.1038/s41598-019-48995-4

Shi, W., Caballero, J., Huszár, F., Totz, J., Aitken, A. P., Bishop, R., … Wang, Z. (2016). Real-time single image and video super-resolution using an efficient sub-pixel convolutional neural network. *IEEE Conference on Computer Vision and Pattern Recognition (CVPR), 2016*, 1874–1883. https://doi.org/10.1109/CVPR.2016.207

Shuvo, M. B., Ahommed, R., Reza, S., & Hashem, M. M. A. (2021). CNL-UNet: A novel lightweight deep learning architecture for multimodal biomedical image segmentation with false output suppression. *Biomedical Signal Processing and Control, 70*, Article 102959. https://doi.org/10.1016/j.bspc.2021.102959.

Soltanian-Zadeh, S., Sahingur, K., Blau, S., Gong, Y., & Farsiu, S. (2019). Fast and robust active neuron segmentation in two-photon calcium imaging using spatiotemporal deep learning. *Proceedings of the National Academy of Sciences, 116*(17), 8554. https://doi.org/10.1073/pnas.1812995116

Song, W. T., Lai, I.-C., & Su, Y.-Z. (2021). A statistical robust glaucoma detection framework combining retinex, CNN, and DOE using fundus images. *IEEE Access, 9*, 103772–103783. https://doi.org/10.1109/ACCESS.2021.3098032

Štajduhar, A., Džaja, D., Judaš, M., & Lončarič, S. (2019). Automatic detection of neurons in NeuN-stained histological images of human brain. *Physica A: Statistical Mechanics and Its Applications, 519*, 237–246. https://doi.org/10.1016/j.physa.2018.12.027.

Sugawara, T., Kawase, M., Lewén, A., Noshita, N., Gasche, Y., Fujimura, M., & Chan, P. H. (2000). Effect of hypotension severity on hippocampal CA1 neurons in a rat global ischemia model. *Brain Research, 877*(2), 281–287. https://doi.org/10.1016/S0006-8993(00)02684-6.

Uluç, K., Miranpuri, A., Kujoth, G. C., Aktüre, E., & Başkaya, M. K. (2011). Focal cerebral ischemia model by endovascular suture occlusion of the middle cerebral artery in the rat. *JoVE (Journal of Visualized Experiments), 48*, Article e1978. https://doi.org/10.3791/1978.

Vizcaíno, A., Sánchez-Cruz, H., Sossa, H., & Quintanar, J. L. (2021). Pixel-wise classification in hippocampus histological images. *Computational and Mathematical Methods in Medicine, 2021*, 6663977. https://doi.org/10.1155/2021/6663977

Wang, J., Jahn-Eimermacher, A., Brückner, M., Werner, C., Engelhard, K., & Thal, S. C. (2015). Comparison of different quantification methods to determine hippocampal damage after cerebral ischemia. *Journal of Neuroscience Methods, 240*, 67–76. https://doi.org/10.1016/j.jneumeth.2014.11.001.

Woeffler-Maucler, C., Beghin, A., Ressnikoff, D., Bezin, L., & Marinesco, S. (2014). Automated immunohistochemical method to quantify neuronal density in brain sections: Application to neuronal loss after status epilepticus. *Journal of Neuroscience Methods, 225*, 32–41. https://doi.org/10.1016/j.jneumeth.2014.01.009.

Xie, W., Noble, J. A., & Zisserman, A. (2018). Microscopy cell counting and detection with fully convolutional regression networks. *Computer Methods in Biomechanics and Biomedical Engineering: Imaging & Visualization, 6*(3), 283–292. https://doi.org/10.1080/21681163.2016.1149104

Xu, J., Xiang, L., Liu, Q., Gilmore, H., Wu, J., Tang, J., & Madabhushi, A. (2016). Stacked Sparse Autoencoder (SSAE) for nuclei detection on breast cancer histopathology images. *IEEE Transactions on Medical Imaging, 35*(1), 119–130. https://doi.org/10.1109/TMI.2015.2458702

Yang, J., Song, S., Li, J., & Liang, T. (2014). Neuroprotective effect of curcumin on hippocampal injury in 6-OHDA-induced Parkinson's disease rat. *Pathology - Research and Practice, 210*(6), 357–362. https://doi.org/10.1016/j.prp.2014.02.005.

Yang, Y., Mufson, E. J., & Herrup, K. (2003). Neuronal cell death is preceded by cell cycle events at all stages of Alzheimer's disease. *The Journal of Neuroscience, 23*(7), 2557. https://doi.org/10.1523/JNEUROSCI.23-07-02557.2003

Yata, K., Matchett, G. A., Tsubokawa, T., Tang, J., Kanamaru, K., & Zhang, J. H. (2007). Granulocyte-colony stimulating factor inhibits apoptotic neuron loss after neonatal hypoxia–ischemia in rats. *Brain Research, 1145*, 227–238. https://doi.org/10.1016/j.brainres.2007.01.144.

Yavuz, E., Güllüoglu, M. G., Akbas, N., Tuzlalı, S., Ilhan, R., Iplikçi, A., & Akhan, S. E. (2001). The values of intratumoral mast cell count and Ki-67 immunoreactivity index in differential diagnosis of uterine smooth muscle neoplasms. *Pathology International, 51*(12), 938–941. https://doi.org/10.1046/j.1440-1827.2001.01307.x.

Zarow, C., Lyness, S. A., Mortimer, J. A., & Chui, H. C. (2003). Neuronal loss is greater in the locus coeruleus than nucleus Basalis and Substantia Nigra in Alzheimer and Parkinson Diseases. *Archives of Neurology, 60*(3), 337–341. https://doi.org/10.1001/archneur.60.3.337

Zecca, L., Youdim, M. B. H., Riederer, P., Connor, J. R., & Crichton, R. R. (2004). Iron, brain ageing and neurodegenerative disorders. *Nature Reviews Neuroscience, 5*(11), 863–873. https://doi.org/10.1038/nrn1537

Zhou, Z., Siddiquee, M. M. R., Tajbakhsh, N., & Liang, J. (2020). UNet++: redesigning skip connections to exploit multiscale features in image segmentation. *IEEE Transactions on Medical Imaging, 39*(6), 1856–1867. https://doi.org/10.1109/TMI.2019.2959609

Zhu, Y., Fotinos, A., Mao, L. L. J., Atassi, N., Zhou, E. W., Ahmad, S., … Wang, X. (2015). Neuroprotective agents target molecular mechanisms of disease in ALS. *Drug Discovery Today, 20*(1), 65–75. https://doi.org/10.1016/j.drudis.2014.08.016.

Zhu, Y., Liu, F., Zou, X., & Torbey, M. (2015). Comparison of unbiased estimation of neuronal number in the rat hippocampus with different staining methods. *Journal of Neuroscience Methods, 254*, 73–79. https://doi.org/10.1016/j.jneumeth.2015.07.022.

5.3 Summary.

The information presented in this chapter exhibits the achievement of establishing a predicting model capable of identifying neurons but also dynamic enough to identify other types of cells. It also described image processing techniques that helped deep learning models enhance their predicting capabilities.

CHAPTER VI - AUTOMATICALLY COUNTING NEURONS.

6.1 Introduction.

In this chapter it is described a system that is designed and built to automate cell counting task based on the deep learning model conceived previously. With this, the third research objective is fully addressed. In addition, this section presents some images of the key functionalities built-in in the application.

6.2 System implementation.

For building a system that is capable of performing cell counting automatically and, for instance, help laboratory technicians evaluate the effectiveness of treatments, several factors were considered but the most important aspects to decide how the system was built are: programing language and technology used for the deep learning model, time available for system development, cost and available technological infrastructure, the familiarity of users with technology and computer systems in general, and human interface factors.

The deep learning model was built with PyTorch using python programming language. Despite having utility packages that permit PyTorch models to be exported and be used in a mobile application, just the model size is big enough, 200 megabytes, to discourage the creation of a mobile application. This factor, along with the foreseen user interaction gathered by previous application and the need of having a screen big enough to easily see the details of the images, makes this option unfeasible.

With the pervious factors in mind, the alternative of creating a desktop application was evaluated, however because of the diversity of operating systems used in the pharmacology department and the lack of time to setup a working environment on each individual computer this option was later discarded.

In this way, to avoid incurring expensive traditional client-server applications, it was identified that the system could be packaged in a Docker container. Given that Docker containers can run on operating systems used in pharmacology department and can have installed in them the programming language needed to run the deep learning model, it was conceivable these factors would permit, from a time constrain perspective, an easy environment setup and application development.

With these features in mind, it was decided to build a containerized client-server application, named Cell Counter, were the most straight forward way to use this model is in the direction of porting the code inside a backend server. Following this venue, the base image of container is created out of python-slim 3.7 version, the backend server application is built using Flask python library, where the backend application oversees the heavy-lifting task of image pre-processing, image analysis for cell identification and the return of cell location according to their pixel coordinates. The client application is built using HTML and JavaScript technology, it oversees the display of the image provided by the user, sends the image to the backend, receives the cell location, displays markers for each of them, and displays the total count of identified cells.

However, due to time constraints, the registration with INDAUTOR is still pending, hence no further technical diagrams are presented here.

6.3 System usage.

In this section it is briefly explained the steps for accessing the main functionality provided in Cell Counter application.

1. When the application is run with Docker, the application becomes available in a standard web browser as show in Figure VI-1

Figure VI-1. Cell Counter application. Source own creation

2. The user then drops the image to be analyzed, drags the red square to the target region of interest and clicks the gear icon to set the region for the cell identification process as shown in Figure VI-2.

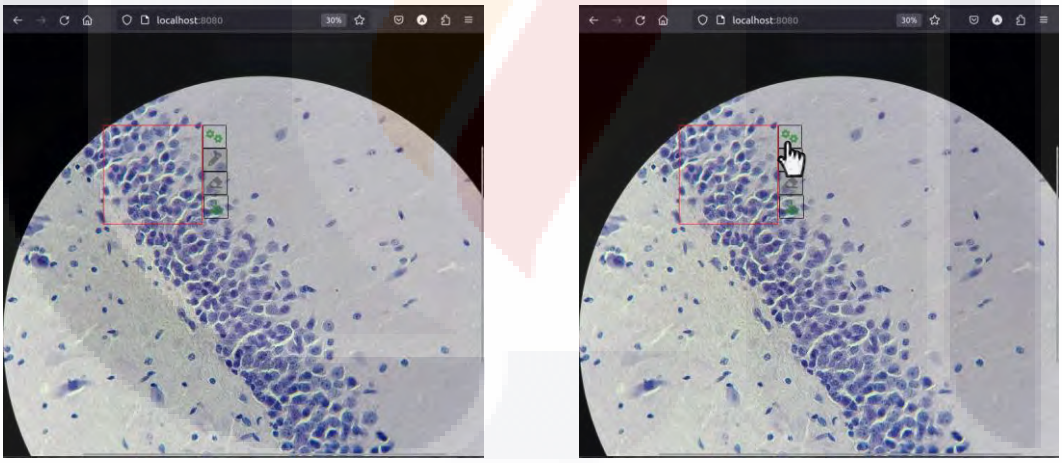

Figure VI-2. Selection of region of interest. Source own creation

3. When the user clicks on the pin-point icon, the system analyzes the image. The Figure VI-3 shows the result of the cell identification process where the user can adjust the results by removing wrongly detected cells with the usage of the eraser icon or adding any missing ones with the pencil icon.

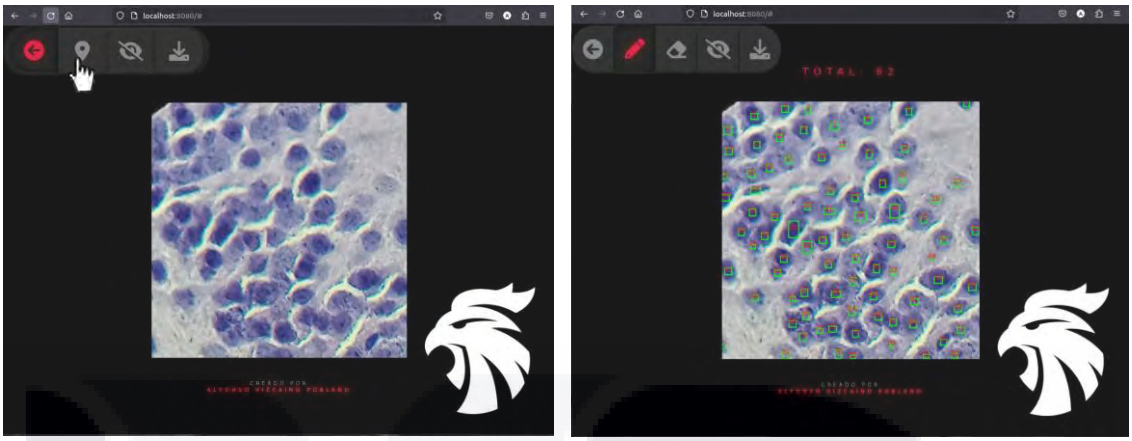

Figure VI-3. Cell identification and adjustment. Source own creation.

4. When the user click the back button, the system takes the user to previous window and lets the user select a new region of interest as shown in Figure VI-4.

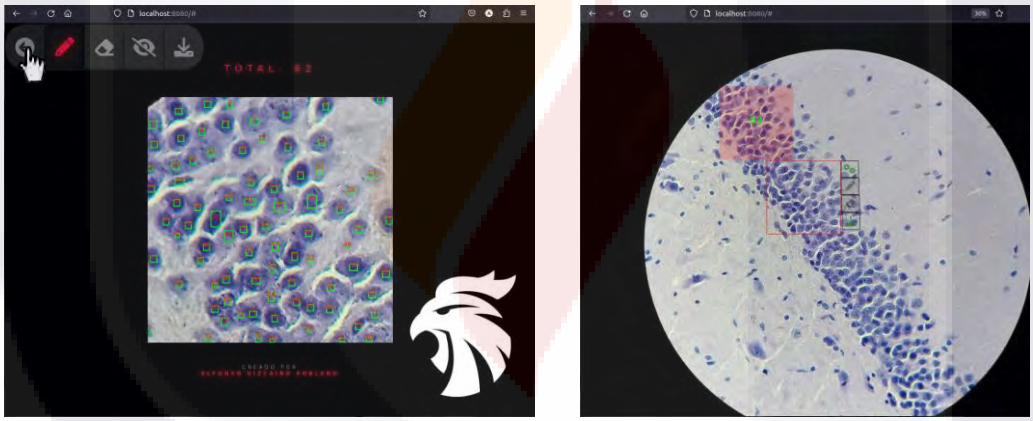

Figure VI-4. Selection of a new region of interest. Source own creation.

6.4 Summary.

This chapter described the implementation of the Cell Counter application, which helps laboratory technicians to automatically count neurons and with this, the third research objective is fully accomplished.

CHAPTER VII - 3D RECONSTRUCTION OF BRAIN AND ITS VIRTUAL REALITY PRESENTATION.

7.1 Introduction.

In this section the reader can know the details of how a series of histological images were used to perform a 3D reconstruction of the brain and how this brain representation was used in a virtual reality application. Therefore, effectively satisfying the fourth and fifth research objective.

7.2 Brain reconstruction.

3D reconstruction is known to be an ill-posed problem since no information of the true shape to be reconstructed is known a priory. Hence, having images alone does not provide any information about the true shape of the final structure, even with an image registration process (Pichat et al., 2018). Therefore, having no prior knowledge of the true shape can cause bad 3D reconstructions because of the “banana problem” or “z-shift”, which is defined as the undesired tendency to straighten curved structures by the optimization of individual images (Lobachev et al., 2021). Figure VII-1 illustrates the “banana problem”.

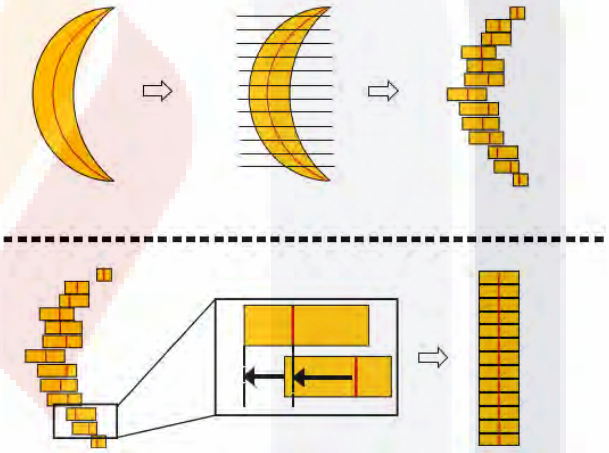

Figure VII-1. The "banana problem". In an attempt to maintain a better similarity to neighboring pixels, it produces large distortions of the real image and tends to create ellipsoids through pairwise alignment of adjacent slices. Image obtained from Lobachev et al., 2021.

3D reconstruction based on histological images, need not only to address this, but must also take care of the loss of continuity due to volume slicing, the peculiarities found in

the images produced by histological procedure itself, and the amount of images available since too few images will not produce a meaningful reconstruction.

Having this information, the initial target of the 3D reconstruction effort was focused on hippocampi only. The main problem faced when collecting images was that not enough serial images of the expected quality could be provided on time by the pharmacology department. Because of this inconvenience, several alternatives were evaluated.

First, state of the art articles that talk about the 3D reconstruction of the hippocampus were searched with the intention of asking the authors for the image dataset that was used, but to the best of the effort, too few articles were found. Nevertheless, the corresponding authors were contacted but it was not possible to get the datasets because of a different number of reasons such as confidentiality, license agreements or simply an answer was not received.

Then, it was decided to search for image dataset available online. Again, to the best of the effort, no feasible dataset was found for histological images of hippocampi. Because of the observed results, the effort was re-oriented towards brain image datasets. When searching for available brain image datasets, a small number of them could be located, but finding only mice brain MRI datasets and a Nissl-stained histological dataset of a single mouse. The problem faced with MRI datasets was not only the size of if, 97 GB per dataset, which translates into an enormous effort to get the ground truth from it but also the lack of an expert to properly establish which of the structures belong to the brain. Finally, when the Nissl-stained images were analyzed, it was determined that they could be used to recreate a 3D brain structure.

The Nissl-stained image dataset belongs to the Allen Brain Institute (Dong, 2008) and it was obtained using their Allen SDK package (Allen Institute for Brain Science & Allen Institute for Cell Science, 2021) with a download sample factor of 3. The dataset is constituted by 509 histological images of different sizes, ranging from 568x538 pixels to 1398x1140 pixels, where slices were approximately spaced at 26 μm.

To perform a 3D reconstruction of the brain, three main stages were conceived. The first stage involves an image pre-processing process to standardize them, the second stage encompasses a set of image processing steps that obtains the main shape representing the

brain, and the final stage puts together the brain shape and displays it in its 3D representation.

The pre-processing phase accounts for the “z-shift” problem too. Here, images are first sorted from anterior to posterior order, then file images are made the same size by making smaller image files have the size of the largest one but conserving their original image proportions by padding them with white color and then are manually relocated. Because histology process can cause the tissue to tear, fold or simply stretch or shrink, images that are too shrunken or stretched in shape and do not provide a smooth continuity of brain shape are removed, leaving only 443 images in the dataset. Finally, the ground truth for the brain is acquired. This process is illustrated in Figure VII-2.

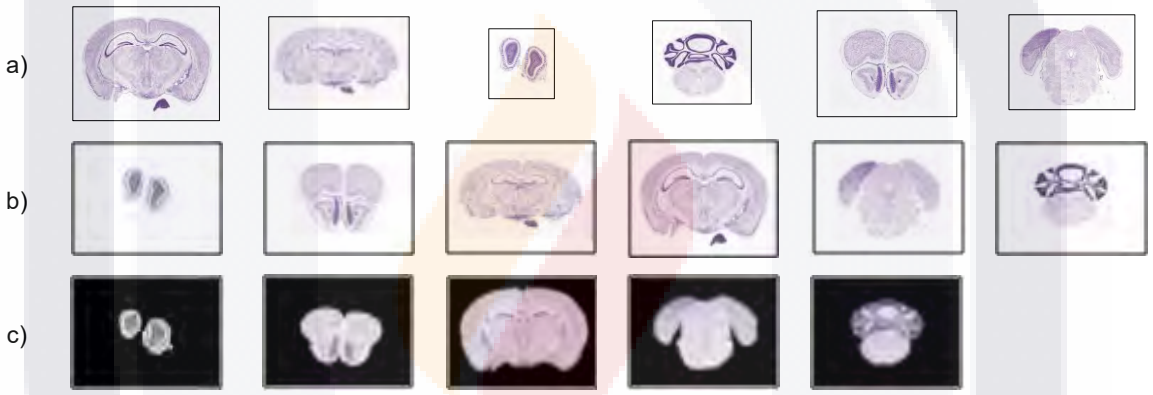

Figure VII-2. Preprocessing phase. a) original images obtained from Dong, 2008. b) sorted original images with their file size standardized and padded with white color. c) Removed bad quality images, ground truth source is presented by denoting non-brain structures with black color. Images from b) and c) were produced by this work. Black squares on the edge of images a) and b) were added for file size visualization purposes.

In the second stage of the brain reconstruction, the following steps are implemented to acquire its main shape. First, brain masks are gotten by binarizing the images attained in previous phase. To reduce the uneven edges caused by binarization, two opening morphological operators with an elliptical kernel size of 5x5 are applied and this is followed by a closing operator with the same kernel. Then, to further remove any noise expressed as isolated blobs, small structures equivalent to an area of 190 are ignored, that is, structures less than ~14x~14 pixels. Next, the brain contour is computed on all images, and for each image, every *n* pixel is extracted to constitute the representation of the brain slice, in this case with *n*=14. To visually assess what a nice representation of the brain looks like using

as little data as possible and without losing important details, this process is repeated but with a downscaled image of size 500x408 pixels and using an *n* of 1, 2, 4 and 14. The result of this process is illustrated in Figure VII-3. For this work a file size of 1398x1140 with an *n* = 14 is chosen. Finally, the extracted pixels are stored in a file in obj format where each pixel represents a vertex, and each image along with its extracted pixels constitute a face.

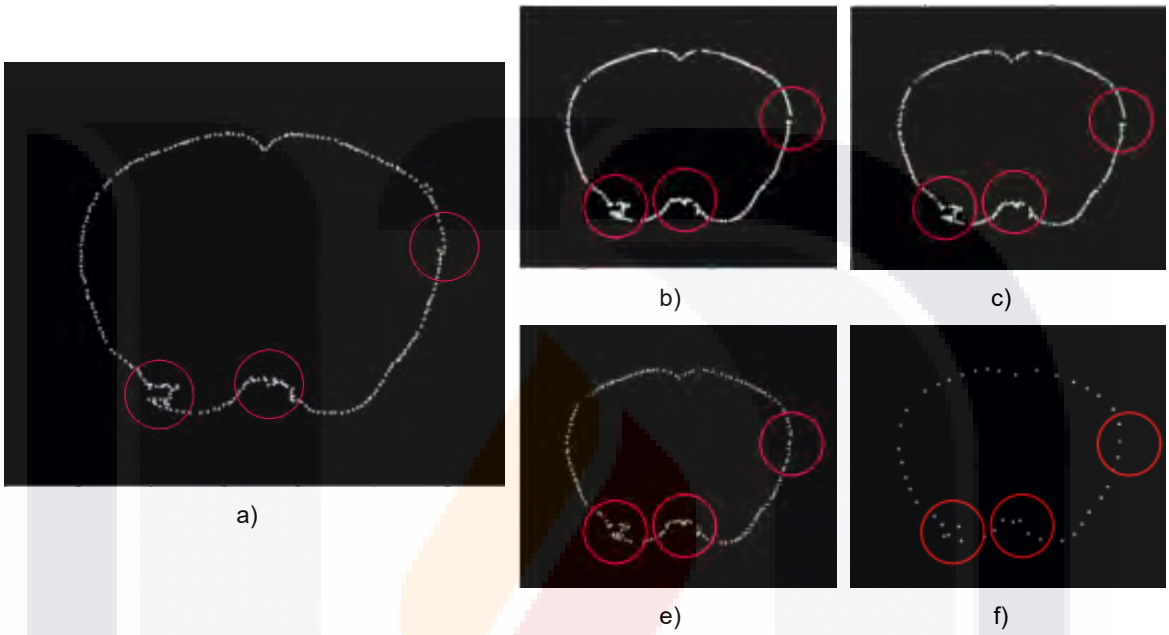

Figure VII-3. Contour extraction. Sampling results with an example image, red circles denote important image details observed with different n selection. a) Image size of 1398 x 1140 and n=14. b)-f) Image size 500 x 408 with n=1, 2, 4, 14 respectively. Images a)-f) produced by this work. Source own creation.

For the final stage, the obj file is processed and for each face in the file all its vertexes are joined sequentially with a straight line. To give the impression of a 3D perspective, faces further away from the user perspective are painted with darker colors while faces closer to user perspective are painted in lighter colors. Finally, the well-known rotation matrix formulas are computed to rotate vertexes and display the reconstructed brain shape in 3D visualization. Sample 3D reconstruction perspectives are presented in Figure VII-4.

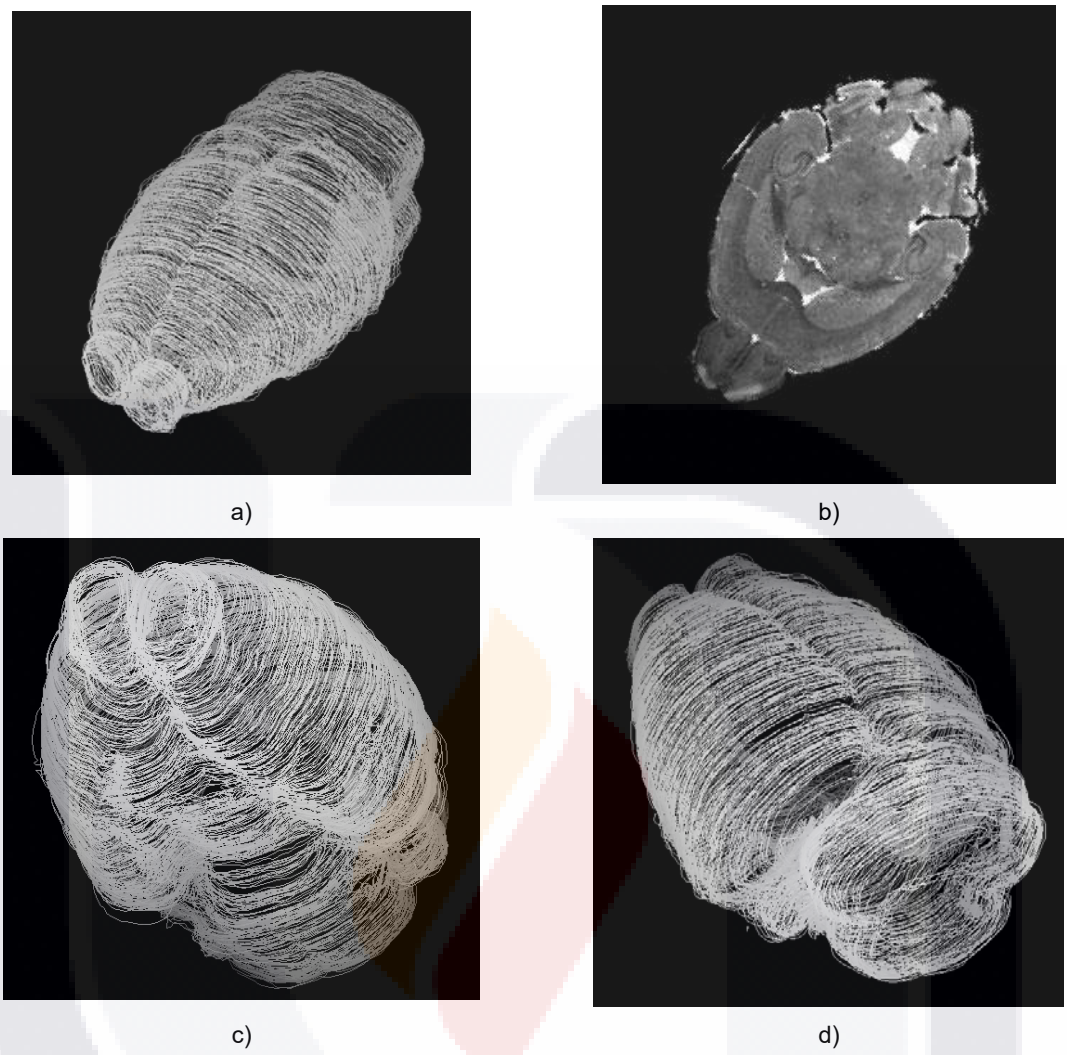

Figure VII-4. Brain reconstruction. A Sample 3D brain reconstruction using n=14. a) superior to inferior perspective. b) a slice of an MRI mouse brain presented here for comparative purposes with approximately the same orientation and obtained from Badea et al., 2007. c) inferior to superior perspective. d) posterior to anterior perspective. Source own creation.

7.3 VR application.

The main technical factor for building a VR application was the cost of VR headsets and programing language. Despite good quality headset available in the market, acquiring them would result in higher costs that expected, for this it was decided to buy a generic VR headset having the advantage that any future upgrade in the system would not incur it to be locked-up in costly proprietary hardware.

The selected VR headset has a field of view range of 90° - 120°, it has two 40mm diameter HD resin aspherical lens and as most common generic headset, an adjustable inter pupillary distance of 60-70mm, an adjustable focal distance of 37.5-46.5mm, a button to click the screen and it is capable of holding smartphones from 5.5” to 7.2” however, the VR headset does not contain any sensor itself. Having established the generic VR headset to be used, the next factor to be decided is the programming language. Given that the VR headset needs a mobile phone, two options are naturally offered, Android or iOS and with them the programming language. Since previous applications were developed with Android, it was decided to continue with this venue to expedite the development effort.

The Android application was built using an API target of 27 and due to time constrains it was not considered the usage of other third-party frameworks such as Unity for building the 3D scene. To provide an immersive experience the application interacts with the gyroscope sensor to detect head movements. Movement detection is then translated into interactive actions such as brain rotation or scene navigation. One consideration to have in mind is that to emulate depth illusion, VR applications need to display two images, one for each eye, to help create a 3D experience. For this, the screen is logically divided into two sections, one for each eye, and the same image is presented to each eye.

The VR application provides three main functions, a 3D Brain Explorer, a Tissue Navigator, and a Credits section. In the 3D Brain Explorer, the user can visualize the brain reconstruction through VR experience. In the Tissue Navigator, the user can see each of the images that were used to construct the brain and their approximate correspondent depth location. Finally, the Credits section provides information about the research institution.

7.4 System usage.

In this section it is briefly explained the steps for accessing the main functionality provided in VR application, but before interacting with the application through the VR headset, the user needs to adjust the focal and pupil distance to get a clear image. To achieve this, the application is started first and then the smartphone is placed in the mobile compartment of the headset. Once this is done, the user can wear the headset and adjust the focal and pupil distance to obtain a clear image. Finally, when the user is ready, the user can click the headset button to begin with the VR experience. Because of paper size constraint, in this

section only Figure VII-5 is presented with the two images needed to create the depth appearance.

Note: In this section, except otherwise noted, all brain reconstructed images were created in this work. All avatar user images were created in this work based on https://icon-library.com/icon/virtual-reality-icon-6.html.html>Virtual Reality Icon # 228757. All histological images shown here were processed in this work, but original images were obtained from Dong, 2008. All brain MRI images shown here were obtained from (Badea et al., 2007).

1. Figure VII-5 show the first scene which helps the user to adjust the headset settings to get a clear image.

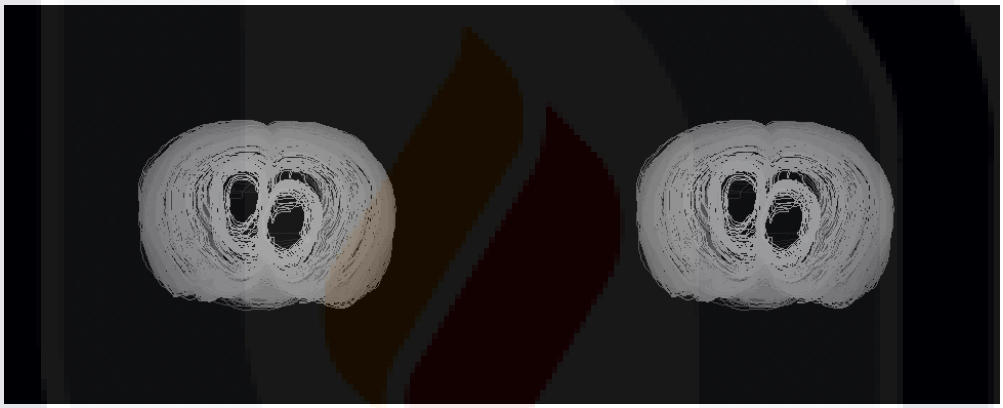

Figure VII-5. 3D reconstruction presented in VR. The 3D brain reconstructed with anterior to posterior perspective in a VR experience. Source

2. The main menu for VR application is shown in Figure VII-6. Here, head movement is translated into user movement through the menu scene which lets the user choose the desired menu option when clicking the headset button.

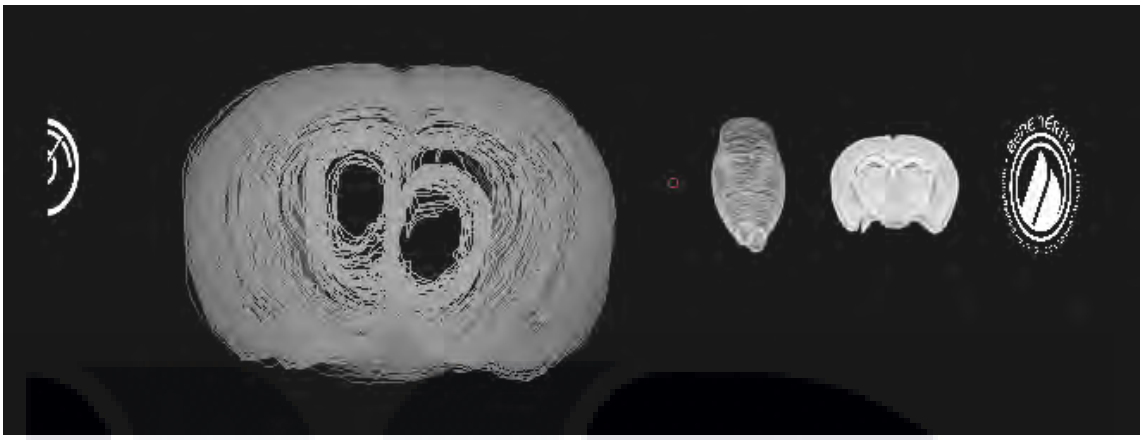

Figure VII-6. Main menu scene. The red circle acts as a pointer that helps the user locate herself in the scene and navigate it.

3. To go to the 3D Brain Explorer in VR application, the user needs position herself on the small 3D brain menu item and click the headset button as shown in Figure VII-7.

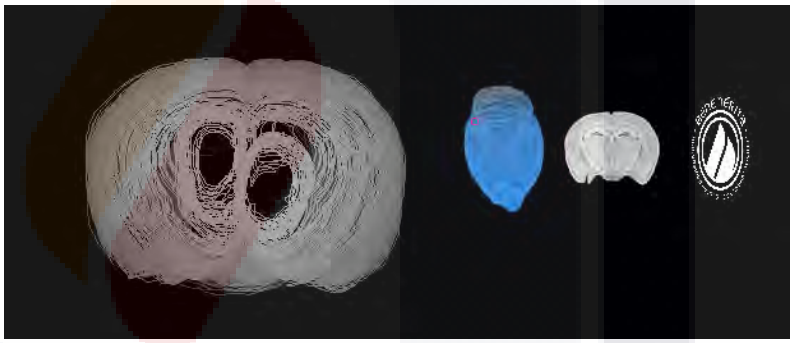

Figure VII-7. Selection of 3D Brain Explorer. The user turns right to move the red circle and positions it over the menu item. The menu item turns its color to blue to indicate that this has become enabled.

4. In the 3D Brain Explorer head movement is now interpreted as brain rotation movement. Figure VIII-8 displays several examples of the brain rotation caused by the head movement.

a)

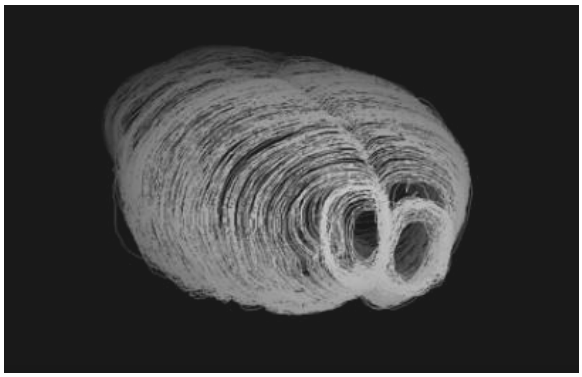

b)

Figure VII-8. VR Interaction with 3D Brain Explorer. a) Turning right. b) Turning up and left. To go back to the main menu, the user must click the headset button.

5. Being in the main menu, to go to the Tissue Navigator in VR application, the user needs position herself on the histology image and click the headset button as shown in Figure VII-9.

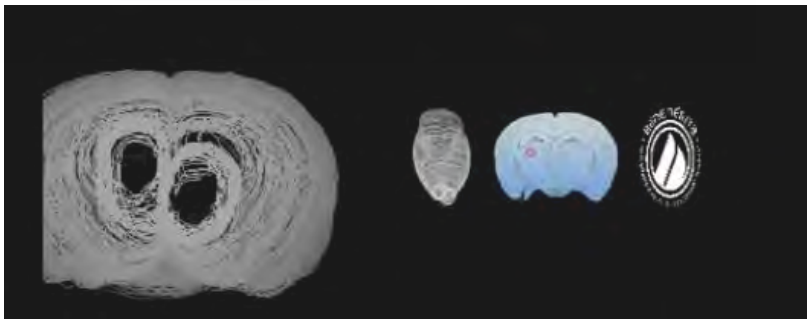

Figure VII-9. Selection of Tissue Navigator. The user turns right to move the red circle and positions it over the menu item. The menu item turns its color to blue to indicate that this has become enabled.

6. In the Tissue Navigator, head movement is used to position the cursor and navigate forward or backward through the set of images used in this research. Figure VII-10 displays several examples of this functionality.

a)

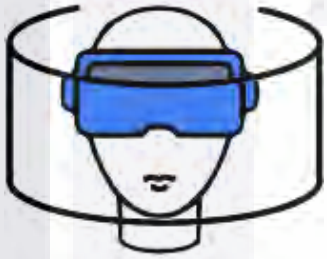

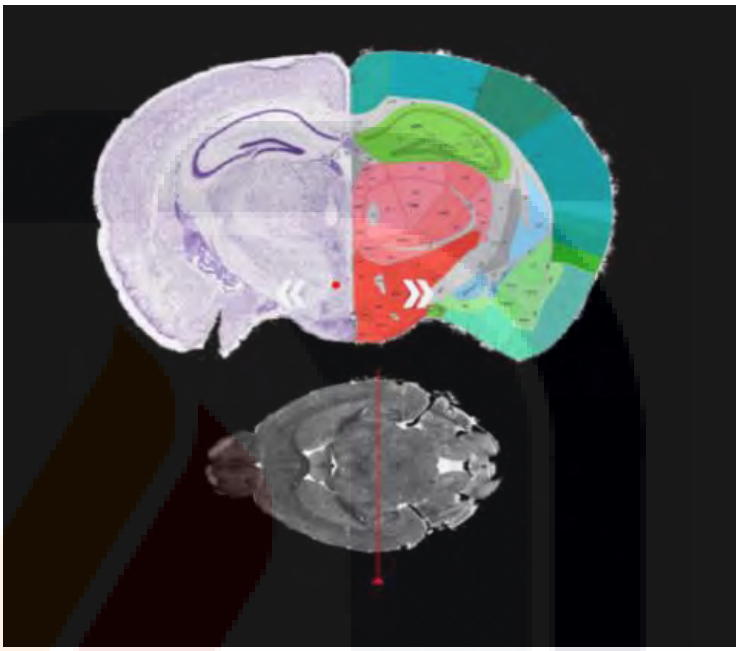

b)

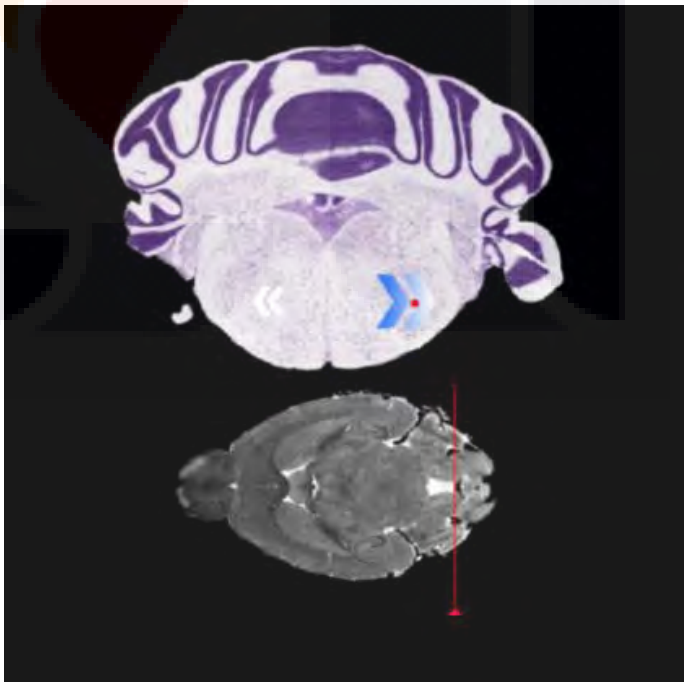

c)

Figure VII-10. VR Interaction with Tissue Navigator. The vertical red line indicates the approximate depth of the displayed image. a) Main screen. b) Turning right. c) Turning left. To go back to the main menu, the user must click the headset button.

7. Being in the main menu, to go to the Credits section, the user needs position herself on the university logo and click the headset button as shown in Figure VII-11.

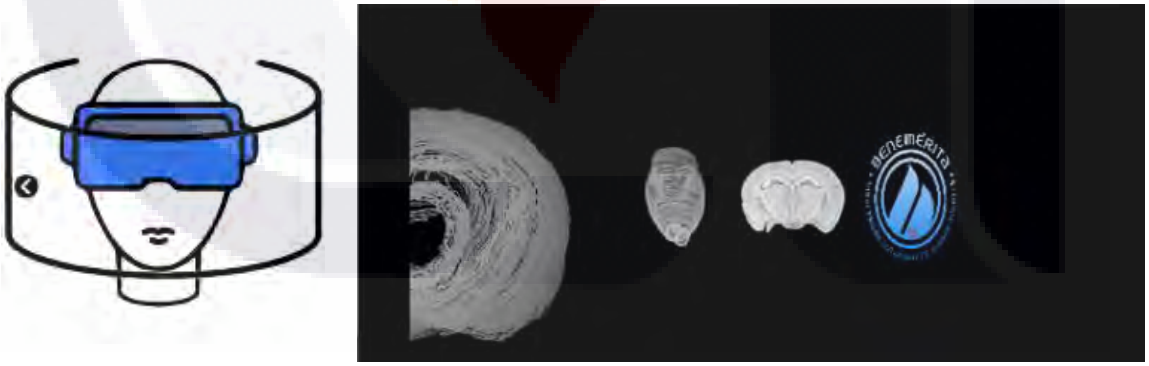

Figure VII-11. Selection of Credits section. The user turns right to move the red circle and positions it over the menu item. The menu item turns its color to blue to indicate that this has become enabled.

8. In the Credits section, head movement is used to move across the scene. Figure VII-12 shows the logo of the institution where this research was made and the student information.

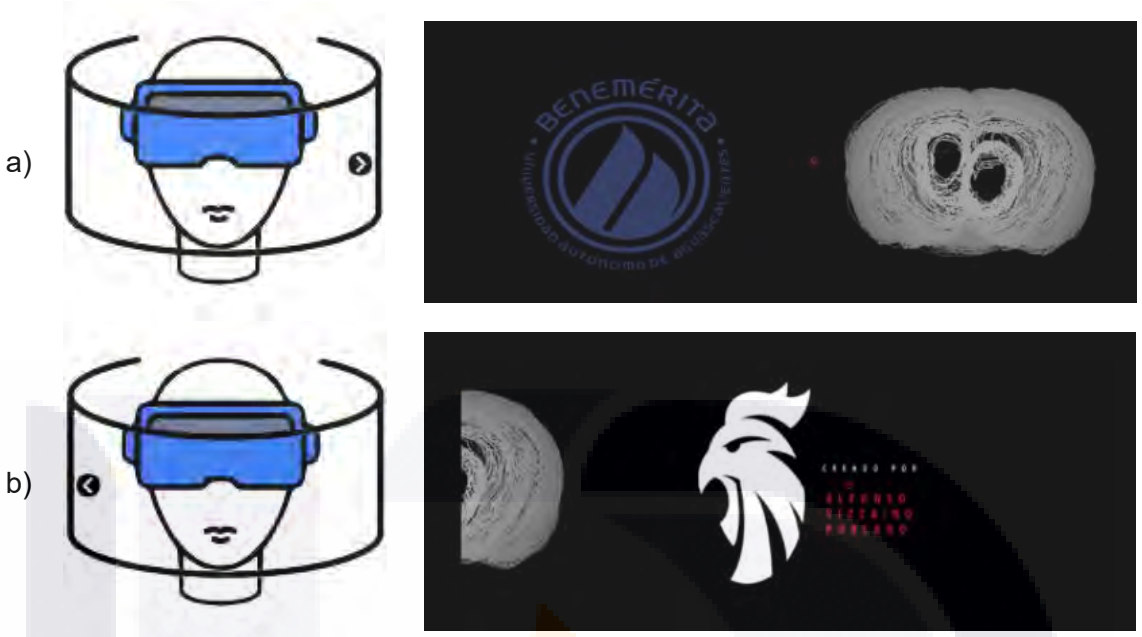

Figure VII-12. VR interaction with Credits section. a) User turns left to see the university logo. b) User turns right to see developer information.

7.5 Summary.

The fourth and the fifth research objective is effectively accomplished by the brain reconstruction and the implementation of the VR application shown here, thus successfully accomplishing all research objectives established in this work. A good direction for future improvement revolving brain reconstruction can be towards incorporating a mechanism to quantitatively measure the accuracy or smoothness of the brain representation. Likewise, the VR application can be enhanced by presenting the 3D brain reconstruction with a mesh and texture or even detecting what are the major brain structures being observed by the user and then show contextual information.

CHAPTER VIII - CONCLUSION.

In this work, several algorithms used in artificial intelligence have been implemented on the analysis of hippocampus histological images with the intention of helping make the work done by scientists more effective and efficient.

It has been shown that rat hippocampus can be detected in histological images using machine learning algorithms. Furthermore, it has been described how with the assistance of these algorithms, new applications can be built to simplify and expedite hippocampus area and volume measurement.

Similarly, it has been demonstrated that neuron identification can be accomplished even in the densest areas of rat hippocampus by employing convolutional neural networks, and with this, it has been presented an application that automates cell counting. This type of application can, for instance, effectively shorten the measurement effort of drug effectiveness in treatments against ischemic strokes.

Finally, an innovative and alternate proposal to analyze and study the brain has been suggested with the building of a virtual reality application that displays a brain in its 3D representation and allows an interactive visualization of its histological images. With this, medical students could benefit from a more dynamic way to visualize and interpret the information available in simple historical images.

Concretely, contributions to computer vision are:

- An image processing algorithm to produce pixel characterization that represents hippocampus.
- A multilayer perceptron model capable of discriminating hippocampus pixels.
- A convolutional neural network architecture skilled in identifying neuron cells.
- An image processing algorithm that builds a 3D brain representation out of histological images.

Contributions to computer science are:

- A procedure to bring a machine learning algorithm into an edge dispositive to create a functional application that facilitates hippocampus area measurement.

- A procedure to bring a convolutional neural network architecture into a containerized client-server application that automates cell counting.
- A procedure to bring a 3D image into a VR application.

8.1 Future work.

There is always room for enhancements and this work is not the exception. As artificial intelligence is evolving at unprecedented rate, the work presented here can be enhanced and leveraged to continually provide better tools to the scientific community which can result in having a positive impact on the health of people.

Measuring hippocampus area or volume is a key indicator for different studies but to achieve this, the hippocampus must be located first. In this topic, alternate artificial intelligence algorithms could be explored to achieve even higher accuracy scores and make the analysis process even easier.

Regarding cell detection and its count automation, this area can benefit from or creating a new deep learning model architecture or incorporating an online learning mechanism that makes the deep learning model more robust as the application is used thus constantly increasing its accuracy and effectiveness.

Correspondingly, in the brain reconstruction subject, future improvements can be focused on incorporating a mechanism to quantitatively measure the accuracy or smoothness of the brain representation. The VR application could improve its 3D brain presentation by displaying it with a mesh and texture but perhaps more importantly enhancing the VR application so that medical students could benefit from a more dynamic learning experience, for instance, displaying contextual information when observing specific brain structures.

REFERENCES

Allen Institute for Brain Science, & Allen Institute for Cell Science. (2021). *Allen Software Development Kit* (2.13.2) [Computer software]. Retrieved from https://allensdk.readthedocs.io/en/latest/

Badea, A., Ali-Sharief, A. A., & Johnson, G. A. (2007). Morphometric analysis of the C57BL/6J mouse brain. *NeuroImage*, *37*(3), 683–693. https://doi.org/https://doi.org/10.1016/j.neuroimage.2007.05.046

Dong, H. W. (2008). *The Allen reference atlas: A digital color brain atlas of the C57Bl/6J male mouse.* John Wiley & Sons Inc.

Lobachev, O., Funatomi, T., Pfaffenroth, A., Förster, R., Knudsen, L., Wrede, C., Guthe, M., Haberthür, D., Hlushchuk, R., Salaets, T., Toelen, J., Gaffling, S., Mühlfeld, C., & Grothausmann, R. (2021). Evaluating Registrations of Serial Sections With Distortions of the Ground Truths. *IEEE Access*, *9*, 152514–152535. https://doi.org/10.1109/ACCESS.2021.3124341

Pichat, J., Iglesias, J. E., Yousry, T., Ourselin, S., & Modat, M. (2018). A Survey of Methods for 3D Histology Reconstruction. *Medical Image Analysis*, *46*, 73–105. https://doi.org/https://doi.org/10.1016/j.media.2018.02.004